MECHANICAL CHARACTERIZATION OF SINGLE MICROBIAL CELLS USING MEMS

by

Bruno Barazani

Submitted in partial fulfilment of the requirements
for the degree of Doctor of Philosophy

at

Dalhousie University
Halifax, Nova Scotia
May 2017

© Copyright by Bruno Barazani, 2017

DEDICATION

I dedicate this thesis to my parents Elie and Sara for their incessant support of my studies and carrier

Table of Contents

List of Tables

List of Figures

Abstract

In this study, the mechanical properties of single yeast cells (baker's and brewer's strains) were measured by an on-chip PolyMUMPs MEMS squeezer in aqueous media. An electrothermal actuator with mechanical amplifiers was used to press single cells against a compliant reference spring. The actuator reached a total displacement of approximately 2.5 μm underwater. Deformations of the cell and the reference spring were measured with nanoscale resolution using optical Fourier Transform techniques. Finite Element Analysis was used to simulate the entire system (squeezer and cell).

Rupture force, stiffness, and hysteresis were measured for a total of 22 baker's yeast cells (*Saccharomyces cerevisiae*). An abrupt reduction in the cell stiffness and the appearance of cracks indicated the rupture force was reached. The average rupture force was 0.47 ± 0.10 μN. The average pre-rupture cell stiffness was 9.3 ± 3.1 N/m; the post-rupture stiffness dropped to 0.94 ± 0.57 N/m. Cells squeezed below the rupture force showed residual deformations below 100 nm while cells squeezed past rupture showed residual deformations between 470 and 960 nm.

Additionally, 31 baker's yeast cells had their stiffness measured during repetitive loading cycles (fatigue tests). Cell stiffness decreased as the cycle number increased. Cells tested up to 268 cycles reached a plateau of 23% of the initial stiffness (drop of 77%) after approximately 200 cycles. Cell viability showed a correlation with stiffness, the cells became less viable as the stiffness decreased.

Finally, 32 brewer's yeast cells had their stiffness and rupture force measured. The brewing cells were evenly divided into 6 groups sorted by 2 species (lager and ale) and 3 fermentation phases (start, middle, and end). Across all fermentation phases ale cells ruptured under an average force of 0.28 ± 0.05 μN, while lager cells ruptured at 0.47 ± 0.10 μN.

This study serves as a proof of concept of a MEMS device able to investigate the mechanics of individual microbial cells. The results presented here complement previous yeast cell mechanics assessments performed by nanoindentation and microplate compression techniques. Researchers and brewers may use this technology to better understand physical differences in their yeast populations.

List of Abbreviations and Symbols Used

~	Approximately
2D	2 Dimensional
3D	3 Dimensional
A	Area
AC	Alternating Current
AFM	Atomic Force Microscopy/Microscope
Amp	Amplifier
Avg	Average
b	Width of Polysilicon Beam
C	Heat Capacity
CAD	Computer-aided Design
CCD	Charge-coupled Device
Chev	Chevron
CMC	Canadian Microsystem Corporation
d	Displacement
DC	Direct Current
Def	Deformation
DEP	Dielectrophoresis
E	Young's Modulus
EA	Ale Cell at End of Fermentation
EL	Lager Cell at End of Fermentation
F	Force
FEA	Finite Element Analysis

FFT	Fast Fourier Transform
h	Height of Polysilicon Beam
I	Moment of Inertia
k	Stiffness, Thermal Conductivity
L	Length of Chevron Arm, Length of Back Spring Beam
MA	Ale Cell at Middle of Fermentation
Max	Maximum
MEMS	Micro-electro-mechanical Systems
Micro	10^{-6} m
Micron	10^{-6} m
ML	Lager Cell at Middle of Fermentation
Nano	10^{-9} m
P	Perimeter
Poly	Polysilicon
PolyMUMPs	Polysilicon Multi-User MEMS Process
R	Electrical Resistance
RBCs	Red Blood Cells
RMS	Root Mean Square
ROI	Region of Interest
SA	Ale Cell at Start of Fermentation
SEM	Scanning Electron Microscopy/Microscope
SL	Lager Cell at Start of Fermentation
T	Temperature
T_{ext}	External Temperature
V	Voltage

V_{RMS}	Root Mean Square Voltage
WBCs	White Blood Cells
XYZ	Three Dimensional Cartesian Coordinate System
α	Coefficient of Thermal Expansion
ΔT	Temperature Increase
Δx	Thermal expansion of Chevron Arm
Δy	Displacement of the Chevron Shuttle
Δz	Vertical Gap
θ	Angle of the Chevron Arm
ρ	Density

Acknowledgements

Firstly, I would like to express my gratitude to Dr. Ted Hubbard for his invaluable guidance throughout these years. His knowledge, dedication, and constant assistance were fundamental for this work.

I would like to thank Dr. Stephan Warnat and Dr. Marek Kujath for their support and precious advices; and Dr. Andrew Macintosh and Dr. Alan Fine for their cooperation and shared knowledge from their respective study fields, which made this interdisciplinary investigation possible. I also thank all the staff from the Mechanical Engineering Department and from Dalhousie University as a whole.

I acknowledge the Brazilian Federal Entity: National Council for Scientific and Technological Development (CNPq) for providing me financial support; and the Canadian Microsystem Corporation (CMC) for the microfabrication service and technical support with CAD and simulation tools.

Finally, I thank my parents Elie and Sara, my sister Adriana, and my lovely girlfriend Fernanda for all their love and support.

Chapter 1: Introduction

1.1 Scope of the Thesis

This study reports the mechanical characterization of individual yeast cells performed by a MEMS squeezer design working in aqueous media. The study comprises the design, finite element simulations, and characterization of the MEMS device; plus the experimental testing of 85 yeast cells divided into baker's and brewer's strains. Stiffness, rupture force, hysteresis, and fatigue of baker's yeast cells were measured and compared to existing results obtained from different experimental platforms. Measurements of stiffness and rupture force were used to characterize and compare two different species of brewer's yeast cells at different stages of fermentation.

1.2 Objectives of the Thesis

The thesis objectives are:

A. Implement an on-chip MEMS device able to precisely measure the mechanical properties of single yeast cells in aqueous media.

B. Analyze and compare mechanical properties of yeast cells of different species, and of yeast cells at different fermentation phases.

C. Compare cell measurements with assessments from other existing techniques.

D. Provide validated computational models of the MEMS squeezer design.

1.3 Cell Mechanobiology

Mechanobiology is the field of study derived from the intersection of engineering (mechanics) and biology. In particular, cell mechanobiology is the study of the relations between cell mechanics and its biological functions. It is known that mechanical loads experienced by a cell can influence cellular processes such as cell differentiation and migration [1]. Moreover, a cell's mechanical properties are often related to its biological state [1]. For example, the conversion of fibroblasts from sessile to motile states is associated with a dramatic reduction in cell stiffness [2]. Many studies have reported changes in cell Young's modulus and stiffness associated with diseases including diabetes [3] and cancer [4]. For example, increased stiffness of red blood cells (RBCs) in malaria [5] and sickle cell anemia compromises those cells' ability to squeeze through small capillaries contributing to the pathology of these diseases [6]. Leukemia-derived T-lymphocytes (cancerous white blood cells) have an elastic modulus only about half of normal T-lymphocytes [7]. Also, decreased stiffness of metastatic cancer cells [5] may contribute to their invasiveness [8]. Thus measurements of cell stiffness may provide a sensitive tool for early diagnosis of such diseases.

Another important mechanical characteristic of a cell is its membrane rupture force threshold. Cell lysis or membrane disruption may be carried out experimentally to allow the retrieval and analysis of intracellular molecules such as DNA and proteins [9] but it is also a mode of cell death in response to developmental or pathological processes where it is associated with changes in cell stiffness [10]. Finally, the abilities to recover from deformations (cell hysteresis) and to resist repeated mechanical loading (cell fatigue) are fundamental for the performance of a number of cells types such as blood, epithelial and bone cells.

1.4 MEMS Technology

1.4.1 Overview

Micro-electro-mechanical systems (MEMS) are micro fabricated devices that can sense and/or provide motions in the micro and sub-micro scale. Structural dimensions range from hundreds of nanometers to hundreds of micrometers. At this scale, forces that are proportional to area or length (e.g. electrostatic, van der Walls, adhesion, and surface tension forces) are dominant compared to forces that are proportional to volume (e.g. gravitational and inertial forces) [11]. In fact, adhesion forces may completely prevent a device's motion [12]. Miniaturized machines can be batch produced and can integrate multiple components in the same chip unit resulting in multifunctional devices fabricated for a much lower cost. Furthermore, MEMS are likely to exhibit faster response, increased sensitivity, lower power consumption, and improved accuracy and reliability compared to macro devices [11].

While macro scale machining uses physical processes such as drilling or milling, micro scale machining adopts physical-chemical procedures such as photolithography and etching. Such processes are similar to the ones used for microelectronics [13]; MEMS fabrication uses sacrificial layers that are released at the end of the process allowing relative motion between the device's structural layers and the substrate. During fabrication, material layers (usually polysilicon and oxides) are deposited and structured by multiple steps of deposition, photolithography and etching until the desired functionality is achieved. Final devices are separated and packaged in housings that allow interactions with electrical inputs/outputs, such as power supplies and meters.

1.4.2 MEMS for Measuring Cell Mechanics

Despite the existence of several traditional methods to measure cell mechanics, MEMS, or in this case BioMEMS, seem to be well suited for this task. MEMS have dimensions, motions, and force scales that match those of the cells [11], [14]. Galbraith [15] was one of the first to use a micro machined platform to gauge cell mechanics. The study assessed the traction forces of single fibroblasts attached to the free end of a micro cantilever. The micro scale system was able to measure deformations and forces on the micro and sub-micro scale by optically monitoring the cantilever deflections. Microfabricated structures can also be utilized in multiple arrays and combined with microfluidic platforms to test a large number of cells with low cost (per unit) and no need of big equipment or laboratorial installations. Youn [16] implemented a microfluidic device composed of a series of adjacent micro orifices (filters) through which the cells were aspirated. Because the length of the orifices increased from filter to filter, the cells needed to deform more to pass through. Cell deformability was measured based on their lysis rate (cell rupture) at each filter. The system was able to test more than 400 red blood cells per minute.

1.5 Individual Cell Manipulation

In the absence of a complex microfluidic system able to accurately move and place cells on a microchip, capillary micropipettes can be used to manipulate cells one by one. In this approach, a micropipette is attached to a micromanipulator (of at least 3 degrees of freedom) which moves the micropipette tip to a visually selected cell settled on the chip substrate. The cell is then aspirated by applying negative pressure to the micropipette and moved to the desired location where it is released by applying positive pressure [17]. Although the use of micropipettes for handling single cells requires operator extensive training and has a low cell throughput, the technique is considered accurate and reliable [17]. The inclusion of an automated/robotic cell positioning system could dramatically increase the device capability, but that is beyond the scope of this thesis.

1.6 Yeast

1.6.1 Microorganisms and Yeast Cells

Microorganisms or microbes are microscopic living organisms that are usually unicellular. The microbial cell is simple and small, usually in the 1-10 μm range [18]. The main components of the cells are DNA, ribosomes, cytoplasmic membrane, and for most a cell wall [18]. The microbes include, but are not limited to, bacteria, fundi, and algae. Fundamental life processes are extensively studied on microbial cells [18].

Yeasts are unicellular microorganisms that together with molds and mushrooms are classified as fungus. Yeast microorganisms are simple cells that are robust and easy to cultivate. Yeast cells are eukaryotic as they contain a delimited nucleus and other specialized organelles such as mitochondria [18]. These cellular structures are located within the cytoplasm which is surrounded by a thick (100 to 200 nm) cell wall [19]. The size and shape of yeast cells can vary widely across yeast species. *Saccharomyces cerevisiae*, one of the main yeast species used for baking and brewing, are typically ellipsoids with major diameters ranging from 5 to 10 μm and minor diameters in the 1-7 μm range. A culture of yeast cells goes through three main grow phases: lag, exponential, and stationary [19], [20]. Typically, it takes around 24 hours to reach the stationary phase [19].

1.6.2 Saccharomyces Cerevisiae

Saccharomyces cerevisiae is the yeast species most used in baking and brewing industries. Via fermentation *Saccharomyces cerevisiae* is substantially used to leaven the dough before baking (baker's yeast) and to produce alcoholic beverages such as beer (brewer's yeast), wine, cider, and whisky [19]. Fermentation is the conversion of sugar into CO_2 and ethyl alcohol by the yeast. Other applications of *Saccharomyces cerevisiae* include the production of biofuel (bioethanol) and other types of alcohols such as glycerol, sorbitol and so on [19]. In the biomedical fields, *Saccharomyces cerevisiae*

contributed to advances on oncology, toxicology and pharmacology as the species is used as a model for more developed eukaryotic cells [19].

1.6.3 Brewing Yeasts

The two main species of yeast used in the brewing industry are ale yeast (*Saccharomyces cerevisiae,* described above) and lager yeast (*Saccharomyces pastorianus*). In fact, approximately 90 % of the global production is currently brewed using lager yeast [21]. While there is a great variety within the numerous strains of ale and lager yeast, many studies have noted general differences between both species. The most recognizable of these differences include the historically observed top (ale) vs. bottom (lager) fermentation behaviour and the ability of lager yeast to grow and ferment at significantly colder temperatures than ale yeast [19], [22].

1.6.4 Stress on Yeast Cells

Industrial fermentations induce several forms of environmental stress upon yeast. From high osmolality/sugar content at the beginning of fermentation, to nutrient/oxygen limitation and high ethanol concentrations at the end of fermentation, yeast survives in environments that are too harsh for most microorganisms. One survival mechanism of yeast is physiological changes in organelles such as the cell walls and vacuole over the course of fermentation. For example, when yeast experience cold related environmental stress they undergo an increase in cell wall mannoproteins [23]. Another example is the reorganization of the actin cytoskeleton in response to high osmotic stress as described by [24]. In a study performed on lager yeast by [25], an increase in cell wall size (through mutation) led to an increase in environmental stress resistance during high gravity brewing. These examples indicate that the cell wall of yeast is a dynamic structure which may exhibit changes due to their environment. These changes are favorable to the survival of the yeast; however, not much is known on how such adaptations affect the mechanical characteristics of the cells, such as the strength and stiffness.

1.7 Contributions of the Thesis

Currently, there already exists a large body of work regarding MEMS for mechanical interrogation of individual cells. However, many of these devices are dedicated to the test of non-microbial cells, for example fibroblasts. Microbial cells are typically smaller (usually in the 1-10 μm range) compared to some other MEMS tested cells, which raises additional challenges with manipulation, testing, and measurement resolution. In particular, reported data for the mechanical properties of yeast cells comes predominantly from milli or nano-scale techniques. Since MEMS have been proved to be suitable for investigating cell mechanics, it would be helpful to have a MEMS design for the test of smaller single microbial cells such as yeast.

Furthermore, the mechanical characterization of yeast at the cellular level may be helpful for industrial yeast-related processes such as fermentation. Measured cells mechanical differences between ale and lager species and among different fermentation phases could be used to improve the process efficiency.

Finally, as yeast cells are considered eukaryotic models, accurate measurements provided by a MEMS platform could serve for a better understanding of the mechanics of higher eukaryotic cells such as animal and even human cells.

Chapter 2: MEMS

2.1 Characteristics and Applications

Micro-electromechanical systems or MEMS are microscopic devices able to provide or detect motions on the micro scale. MEMS can work as actuators (motors) such as micro tweezers or as sensing devices such as pressure or force sensors. Their miniaturized dimensions range from hundreds of nanometers to hundreds of micrometers. Miniaturization grants MEMS devices several performance advantages such as higher sensitivity and lower response time due to their lower thermal mass and high frequency response [13]. MEMS can be embedded with micro circuits which are able to provide them power, control and interface connections [13]. MEMS can be easily integrated with micro circuits as both can be fabricated in the same wafer (silicon-based platform) with micro scale lithography precision and improved signal quality due to the shorter connections [13].

MEMS are already present in our daily life. Printer ink-jet nozzles, automotive airbag sensors, and digital micromirror devices used for projectors are some of the most popular and well known applications of MEMS [26]. Automobiles and smart phones are equipped with several MEMS devices including inertial measurement units (accelerometers and gyroscopes), antennas and microphones. For example, automobiles use MEMS sensors for ABS (anti-lock braking system), airbag, yaw rate (for driving stability), air flow (for air conditioning), and so on [27]. In the medical field, MEMS can be used in implants, surgeries, and minimal invasive diagnostics devices due to their very small dimensions. Commercialized fluidic-MEMS (also called Lab on Chip) can be used to analyze biological material at the cellular level with minimal sample amounts which reduce the need for laboratory installations.

2.2 Fabrication

MEMS fabrication is derived from silicon-based microelectronics processes, which are characterized by the batch production of identical microchip units [27], [28]. Surface micromachining is a microfabrication technology that produces planar movable MEMS structures at the surface of a substrate; the structures typically exhibit a very low height/width ratio [27]. Another possible fabrication technology that was considered (but not used) was bulk micromachining, for example SOI processes. Bulk micro machined structures are taller and more robust than surface micromachining. In this work, surface micromachining was chosen for 2 reasons: 1) the height of the surface micro machined structures matches the dimensions of yeast cells (5 to 10 μm), producing an in-plane test platform. 2) As will be discussed later in Chapter 4, in order to measure the low stiffness of biological cells, testing structures should have similar low values of stiffness. Thin surface micro machined structures can be made with lower and adequate stiffnesses for cell testing.

During the surface micromachining process microscopically thin layers are deposited across the entire substrate. After deposition, photolithographic processes are used to pattern selected parts of the layer. The layer material located underneath the non-patterned areas is then removed by chemical etching. Many thin layers of different materials are deposited and patterned into a stack that may be several microns tall. Typically two broad types of layers are used: structural layers e.g. polysilicon and sacrificial layers e.g. oxides. At the end of fabrication the sacrificial layers can be chemically etched without etching the structural layers. The remaining layers can be wholly attached to the substrate or anchored only at one end allowing relative motion between the structural layers and the substrate. The cantilever is one of the simplest MEMS designs and its fabrication flow is shown in Figure 2.1. After fabrication electrical potential can be applied to the anchors to generate electrostatic or thermal energy (by the Joule effect), which is then converted to micro scale motion (MEMS actuators). Likewise, minor deformations of the movable layers could be detected by a voltage change (MEMS sensors).

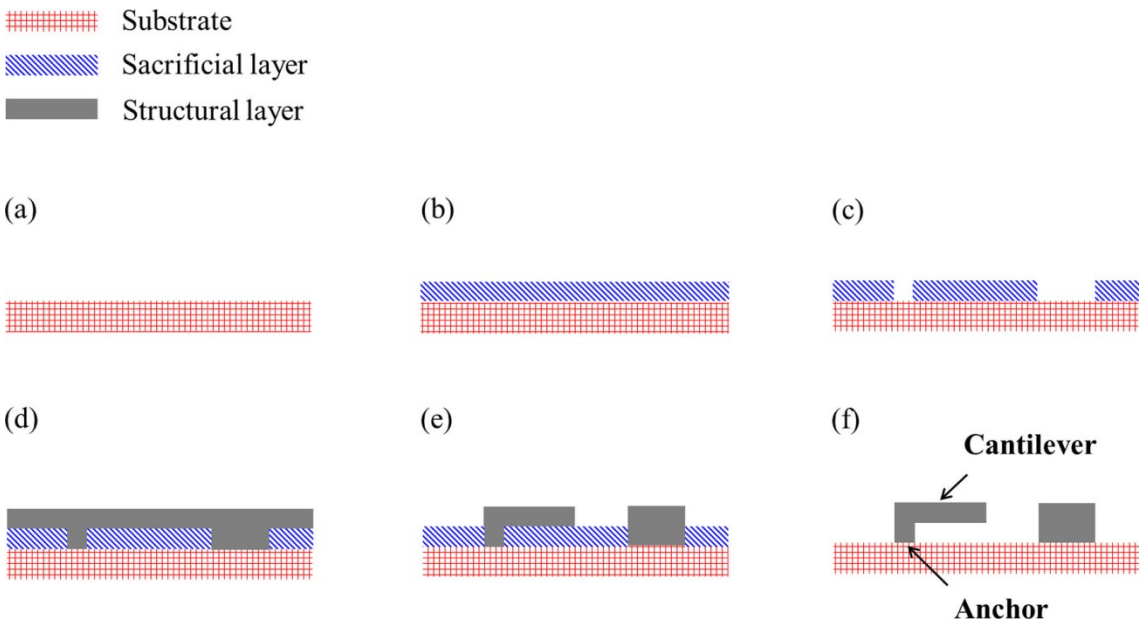

Figure 2.1: Illustration of a MEMS cantilever fabrication flow: (a) Initial planar substrate (b) Sacrificial layer deposition (c) Patterned sacrificial layer (d) Structural layer deposition (e) Patterned structural layer (d) Removal of sacrificial layer resulting in a cantilever free to move relative to the substrate by bending (in plane and out of plane) and a fixed structure wholly attached to the substrate.

2.3 PolyMUMPs

The particular surface micromachining fabrication technique used in this study is the Polysilicon Multi-User MEMS Process (PolyMUMPs) [29]. The process minimum feature (planar resolution) is ~2 µm and all PolyMUMPs layers with their respective thicknesses can be seen in Figure 2.2. PolyMUMPs uses three structural polysilicon layers and two sacrificial oxide layers. A fixed structural layer (Poly 0, 0.5 µm thick) is initially deposited and patterned on a silicon substrate. Next to be deposited and patterned is a sacrificial layer (Oxide 1, 2 µm thick), then the second structural layer (Poly 1, 2 µm thick). In regions without Oxide 1 the Poly 0 and Poly 1 layers are laminated/joined. Oxide 1 is removed at the end of the process allowing relative motion between Poly 1 and the substrate/Poly 0. Next, an optional second sacrificial oxide layer (Oxide 2, 0.75 µm thick), can be deposited. The third structural layer (Poly 2, 1.5 µm thick) is deposited over the Oxide 2, or (as done in this study) laminated directly on the top of Poly 1 resulting in a movable double thickness structure of 3.5 µm. A final metal layer can be

deposited for electrical connections. It is also possible to perform partial etches of the Oxide layers to produce dimples: shallow non-planar depressions in the layers that help prevent flat surfaces from sticking together.

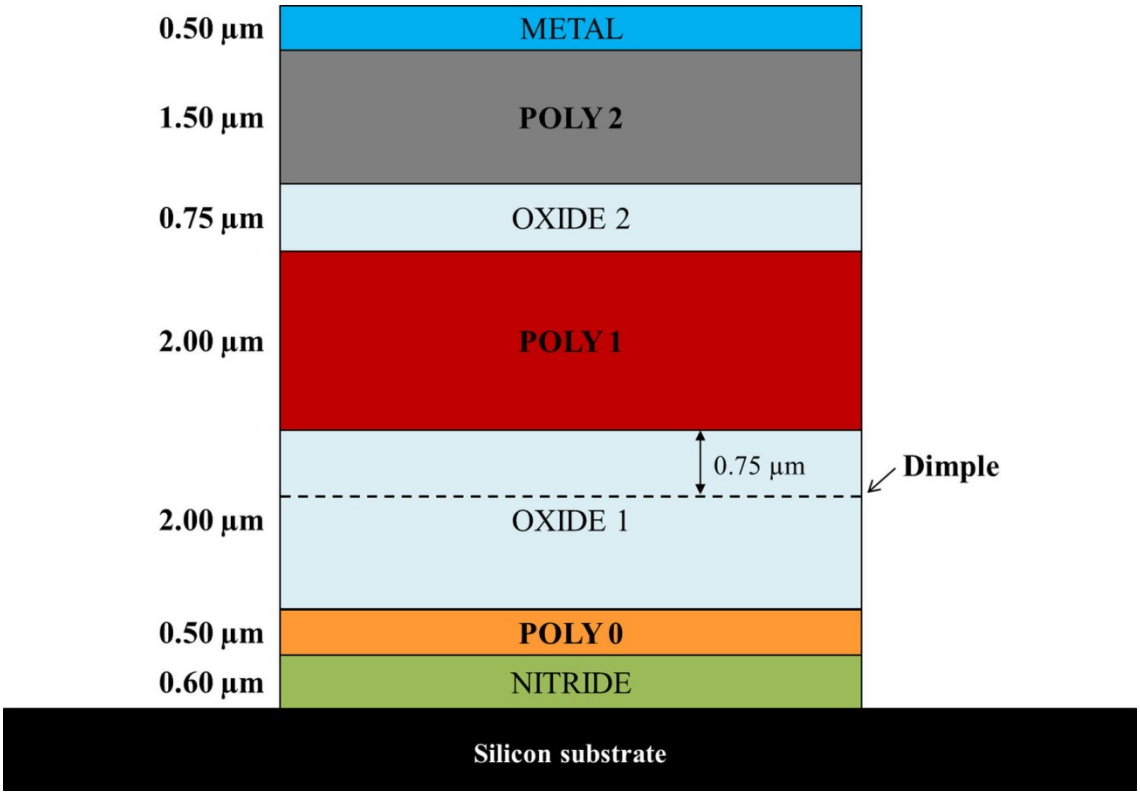

Figure 2.2: Stack of PolyMUMPs layers with their respective thicknesses. Dimples are optional shallow depressions in Poly 1 etched in Oxide 1.

2.4 MEMS in Aqueous Media

MEMS devices fabricated with standard microfabrication processes such as PolyMUMPs are usually designed to operate in air or vacuum. However, in order to interact with biological materials, which naturally belong to aqueous environments, the ability to work underwater is essential. Unfortunately, the operation of MEMS in wet environments is challenging and difficult to attain. The main difficulties are related to the following water characteristics: surface tension, electrical conductivity, and thermal conductivity [30]. The list below briefly summarizes each of these difficulties.

1) When immersed in water surface micro machined structures can trap air bubbles in between the substrate and the moving layers. When this occurs, the water surface tension creates large friction/stiction forces able to completely adhere the devices to the substrate and prevent actuator motion.

2) Water electrolysis is the splitting of water molecules into oxygen and hydrogen (gases) caused by an applied voltage in an aqueous media. This leads to the formation of a large amount of bubbles that may interfere or damage the microscopic system. Electrolysis starts in de-ionized water at approximately 1.2 V.

3) The thermal conductive of water is approximately 20x higher than the thermal conductivity of air. As a result thermal actuators, which depend on a temperature rise to move, undergo a drastic reduction of performance underwater (more on sections 2.5 and 2.6).

4) Finally, depending on the electrical conductivity of the media, the current can bypass the MEMS electrodes and flow through the media itself, reducing the device performance.

Reports of a number of BioMEMS devices confirm the difficulties described above. For example, Scuor [31] used the PolyMUMPs process to fabricate an electrostatic MEMS single cell stretcher. The device was tested in air and in aqueous media where problems with stiction and current bypass led to a maximum displacement of less than 1 μm. A PolyMUMPs, multidirectional cell stretcher was fabricated by Antoniolli [32] using multiple bimorph thermal actuators. The stretcher was characterized in air and vacuum; however, in water no displacement could be measured since electrolysis occurred at voltages above 1.5 V.

Specialized material coatings such as ALD (atomic layer deposition) could be used to avoid problems at the MEMS interface with the aqueous media, as done in [33]. The coating would thermally and electrically isolate the MEMS structures preventing current

bypass, electrolysis, and excessive heat exchange with the media. However such coatings are not part of the standard surface micromachining fabrication processes. Simpler redesigns of the micro devices and the use of high frequency AC electrical inputs can avoid electrolysis; and the design of mechanical amplifiers can be used to improve the actuator's performance. These last approaches were used in this study and will be described in more details in the following sections.

2.5 Electrothermal Actuators

MEMS electrothermal actuators [34]-[36] are devices capable of producing displacements on the micron or sub-micron scale when heated via Joule effect caused by electrical current passing through their structures. The output motion results from the material's (usually silicon or polysilicon) thermal expansion induced by the temperature rise. Electrothermal actuators can provide displacements on the order of micrometers in air and can be more robust than electrostatic actuators due to their high force capacity and stiffer suspensions [37]. They are commonly fabricated in a hot/cold arm configuration or in a 'V' shape (chevron) geometry; both configurations provide an output motion derived from the mechanical amplification of the material's thermal expansion. However, electrothermal actuator's behaviour is considerably influenced by the media in which they work. In particular, underwater their displacement is reduced by an order of magnitude compared to air [30]. This is mostly due to the higher thermal conductivity of water.

2.6 Chevron Electrothermal Actuator

A common thermal actuator design is based on a 'V' shape geometry also called chevron; Figure 2.3 shows a typical electrothermal chevron actuator design. In this configuration, electrical current is induced from anchor to anchor through the chevron arms which are connected to a central shuttle at a small angle θ. The Joule effect increases the arms temperature inducing their thermal expansion which is expressed by:

$$\Delta_x = L\alpha\Delta T \quad (1)$$

Where L is the arm length (from anchor to chevron shuttle), α is the material's thermal expansion coefficient, and ΔT the temperature gradient. The thermal expansion (Δx) is amplified and transmitted to the chevron shuttle which moves a larger amount (Δy) upwards (in plane), albeit with a reduction in the force. The multiple arms; however, provide a larger output force.

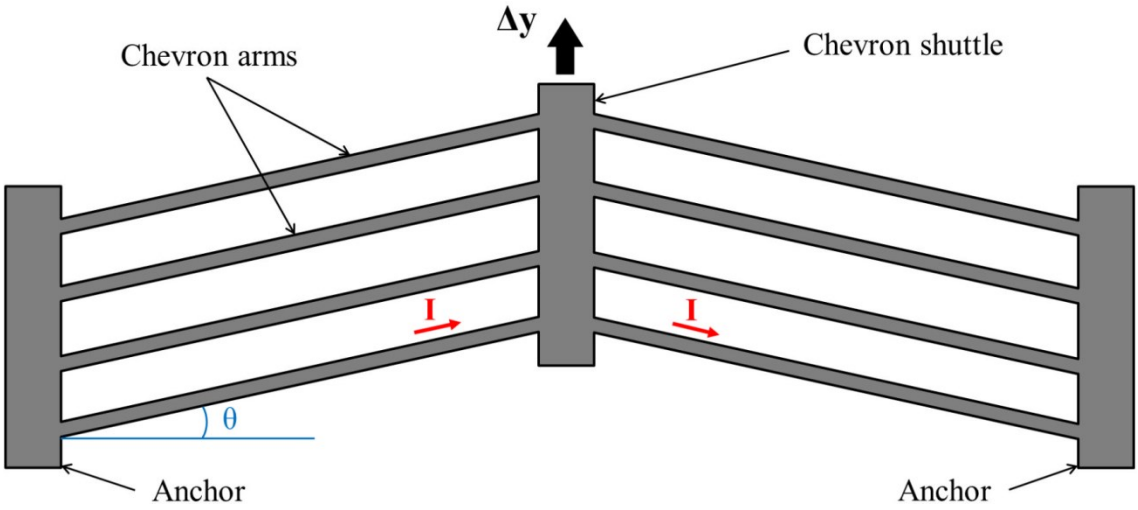

Figure 2.3: Typical PolyMUMPs electro-thermal chevron actuator with multiple arms.

According to a rigid-link kinematic model, the amplification factor is proportional to 1/θ, where θ is the angle of the arms in rads [37]. For example, the chevron actuator used in this study has an angle of 6 degrees (0.1 rad); hence, it amplifies the arms displacement by approximately 10x. Therefore, if Δx is the arm thermal expansion, then:

$$\frac{\Delta y}{\Delta x} \approx \frac{1}{\theta} \quad (2)$$

$$\Delta y \approx \frac{L\alpha\Delta T}{\theta} \quad (3)$$

Thus, from equation 3 the chevron output displacement Δy is inversely proportional to θ and direct proportional to L, both geometric parameters of the chevron design. Typically, chevron electrothermal actuators provide total displacements on the order of 1 μm in air when subjected to ~5V [37].

In order to simulate the temperature distribution over the length of the arms of a thermal actuator, it is necessary to consider the heat generation plus the heat flow in the structural material and the heat exchange between the material and the media surrounding it. From [38], the following differential equation calculates the temperature along each of the chevron arms, assumed to be made of polysilicon:

$$\frac{\partial T}{\partial t}(x) = \frac{k_{poly}}{C_{poly}\,\rho}\frac{\delta \partial^2 T}{\partial x^2} - \frac{k_{media} P/2}{C_{poly}\,\rho\, A\, \Delta z}(T - T_{ext}) + \frac{V^2/R}{C_{poly}\,\rho\, AL} \qquad (4)$$

where T is the arm temperature, T_{ext} is the external surrounding temperature of the media, A is the cross-sectional arm area, P is the cross-sectional arm perimeter, L is the arm length, V is the applied voltage in each arm, Δz is the vertical media gap between the structure and the substrate below (2 μm, PolyMUMPs), R is the electrical resistance of each arm, ρ is the material density (polysilicon), k_{media} is the thermal conductivity of the media surrounding the actuator, k_{poly} is the thermal conductivity of polysilicon and C_{poly} the heat capacity of polysilicon. The numerical integration of equation (4) results in the temperature profile over the chevron arm.

Again from [38], it is possible to estimate the steady state maximum temperature increase (ΔT_{approx}) along each arm by neglecting the term $\boldsymbol{\partial}^2 T/\boldsymbol{\partial} x^2$ from equation (4). This simplification assumes that the vertical temperature gradients ($\boldsymbol{\partial} T/\boldsymbol{\partial} z$) are greater than longitudinal temperature gradients ($\boldsymbol{\partial} T/\boldsymbol{\partial} x$). Thus, equation (4) reduces to:

$$\Delta T_{approx} \approx \frac{V^2}{R}\frac{\Delta z}{k_{media}\, P/2L} \qquad (5)$$

According to equations (1) and (5) the temperature increase and thus the thermal expansion are proportional to voltage squared. Using typical parameter values for a PolyMUMPs electrothermal actuator arm in equation (5): V = 3V, k_{air} = 0.05 W/(mK), R = 1.3 KΩ, Δz = 2 μm, P = 8 μm and L = 150 μm, ΔT_{approx} along this actuator arm in air is on the order of 400 °C. Likewise, considering k_{water} = 1 W/(mK), ΔT_{approx} along the arm in water is approximately 20x smaller, ~20 °C. Later we will see that actual temperatures are significantly smaller since ΔT_{approx} neglects a path of a heat loss and; therefore, is an overestimate of the actual temperatures. Nevertheless, both theory and measurements indicated a temperature increase in water ~20x smaller than in air.

Chapter 3: Cell Mechanics

3.1 Cellular Mechanobiology

Cellular mechanobiology can be divided into the study of how cells sense and respond to mechanical loadings and the study of cell's mechanical properties such as Young's Modulus and stiffness [1]. For example, Moraes [39] stated that loading conditions could change cell's protein expression. Furthermore, mechanical features of living cells appear to be closely related to their biological functionality. For example, sick cells might present changes in their stiffness or Young's Modulus. Below, a number of examples are provided.

Suresh [5] detected that red blood cells' (RBCs) stiffness increased ~10x during malaria parasite development inside the cell while Tsukada [3] found that diabetic RBCs had a lower deformability (cell's ability to change shape when under a deformation force) compared to healthy RBCs. According to these studies, both diseases result in an increase of the RBCs' stiffness. Eventually, stiffer RBCs could lead to an increase in blood's viscosity and, consequently, a higher shear stress on the vessels' walls leading to vascular and heart complications.

In addition to diabetes and malaria, cancer also seems to affect mechanical characteristics of cells. According to [8] metastatic cancerous cells can be 70% less stiff than benign cells. The study indicated that different types of cancer cells (lung, breast and pancreas) have similar Young's modulus (~0.5 kPa) while healthy cells showed higher stiffness (~ 2 kPa). Regarding leukemia (cancerous white blood cells or blood cancer), Rosenbluth [40] found that cancerous white blood cells (WBCs) are ~5x less stiff than healthy WBCs. Finally, Li [41] reported that malignant cancerous breast cells have lower stiffness than benign breast cells. According to the study, the Young's modulus of the cancerous cells was approximately 1.6x lower than that of the healthy cells. In summary, cancerous cells seem to be less stiff than healthy cells.

Some studies [7], [41], [42] have indicated that cell mechanics would be influenced by their cytoskeleton, a chain of protein fibers diffused into the cell cytoplasm. Li [41], for example, linked the lower stiffness of the cancerous cells to a reduction in the number of the cell's filaments (protein fibers), resulting in a weaker cytoskeleton

3.2 Example: Blood Cells Mechanical Properties

This section briefly compares the mechanics of red and white blood cells. Blood is a complex body tissue with essential biological functions composed of different kinds of cells of distinct mechanical characteristics [43]. There are 3 types of cells in blood: red blood cells (RBCs or erythrocytes), white blood cells (WBCs or leukocytes), and platelets (thrombocytes) [44].

Erythrocytes (RBCs) are fundamental for the gaseous exchange between blood and the other body tissues. Human RBCs are biconcave discoids having diameters ranging from 6 to 8 μm [43] that are able to deform considerably without rupturing since they can pass through tiny capillary vessels with diameters on the order of 3 μm [45]. Thus, RBCs should exhibit lower stiffness compared to other cells; they need to have high strength and yet be very flexible [44]. RBCs are less stiff then WBCs and present a Young's modulus a few orders of magnitude smaller than the Young's modulus of yeast cells [46], [47].

Leukocytes (WBCs) defend the body against foreign organisms/materials; they have diameters typically ranging from 9 to 15 μm and are spherical when they are in their passive state [48]. Atomic force microscopy (AFM) based studies indicated that WBCs have Young's modulus on the order of 1 kPa [7] while RBCs have Young's modulus on the order of 0.1 kPa [47].

3.3 Measuring Cell Mechanical Properties

3.3.1 Non-MEMS Platforms

There are several well established techniques for measuring single cell mechanics such as micropipette aspiration, optical tweezers, optical stretchers, magnetic twisting, atomic force microscope, microplate compression and so on [49]-[51]. All of these techniques perform an off-plane interaction between the cell and the actuation [49]. Micropipette aspiration is the most common and measures global properties of the cell (higher contact area), while AFM provides cell wall local measurements with resolution on the order of nanometers. The next paragraphs provide a short description of the four relevant non-MEMS techniques used to mechanically interrogate single cells.

Micropipette aspiration [52] consists of deforming single cells by aspiring them into a micropipette controlled by a micromanipulator. The applied pressure and the corresponding measured cell deformation are used to estimate the cell's elastic properties utilizing a mechanical model. Micropipette aspiration offers a large range of pressures and forces (from 10 pN to 10 μN) compared to other techniques; however, evaporation, drift at zero pressure, low cell throughput and the need for extensive operator training are disadvantages. Figure 3.1 (a) shows a schematic of the micropipette aspiration technique.

Schmid-Schonbein [48] performed measurements of a WBC deformation at 3 different points when subjected to stress via micropipette aspiration. The cell was treated as a homogeneous visco-elastic sphere with no membrane. The close agreement of the results for the three different measurement points on the cell suggested that the measured Young's Modulus could be considered the same in the whole cell.

Optical tweezers (see simplified schematic on Figure 3.1(b)) are able to deform single cells producing forces up to a few hundreds of piconewtons. Focused laser beams produce radiation pressure which leads to forces on dielectric beads attached to both sides of the cell. These forces are sufficient to deform the cell [51]. Despite the high force

accuracy, the method is limited to low forces and may damage the cell due to laser heating.

Atomic force microscopy (AFM) is another technique used to test the mechanics of individual cells [47]. The AFM cantilever probe (driven by a piezo) approaches the cell surface while its deflection is measured via a laser beam that reflects off its back (Figure 3.1 (c)). The moment the probe tip start indenting the cell, the cantilever deflects more or less according to the cell's Young's Modulus which can be calculated afterwards using Hertzian models. The AFM method can measure nanomechanical properties of single cells due to its nano-scale resolution; however, it cannot provide bulk or global cell properties and can only provide small displacements and forces [49], [51].

Finally, microplate compression (Figure 3.1 (d)) consists of squeezing single cells between two flat parallel plates, one movable (e.g. a 50 μm wide probe) and the other fixed (e.g. a glass slide) [53]. The movable plate is equipped with a transducer that measures the force while the cell is compressed up to its rupture (burst). Cell mechanical properties such as stiffness, Young's Modulus and rupture force can be calculated from the force vs displacement curve. Although this method provides large cell deformations and forces, the resolution and accuracy (especially from the downwards motion of the probe) is low. The motion accuracy in [53] was ± 0.2 μm (200 nm).

Despite the existence of many different platforms for measuring single cell mechanics, they typically provide divergent results when analyzing the same type of cell. This may be due to the distinct loading distribution and different mechanical models adopted by each technique. For example, the AFM indentation of erythrocytes utilizing the Hertz model indicated a cell Young's Modulus on the order of 0.1 kPa [47]. However, the optical stretching (similar to optical tweezers with no need of beads) of erythrocytes utilizing finite element analysis and membrane theory models measured a Young's Modulus on the order of 1 kPa [54], [55].

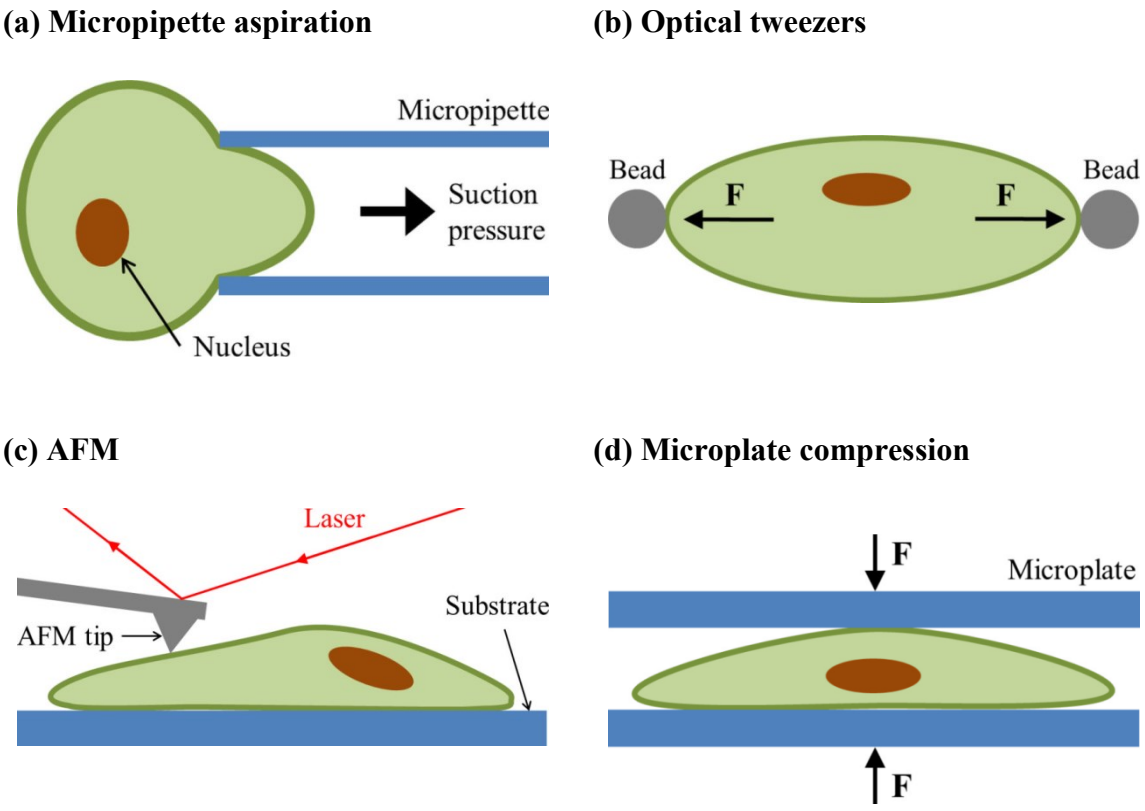

Figure 3.1: Non-MEMS techniques to measure single cell mechanics (F: force).

3.3.2 MEMS Platforms

MEMS have been investigated as promising complementary tools for measuring the mechanical properties of single living cells [14], [49], [56]-[58]. Both MEMS and cells have typical dimensions on the micro-scale; further, MEMS can provide forces and displacements with nanometric resolution in a range that matches with biological systems [14], [57]. MEMS present high flexibility due to their large force range and well-defined load and contact area conditions compared to non-MEMS methods [49]. Moreover, MEMS can provide an in-plane single cell test system, mid to high displacements range, and all the advantages derived from microfabrication such as batch production, quick response, and chip integration [49]. MEMS can also directly stimulate (push or pull) the cell with no need of functionalizing beads (e.g. magnetic or optical beads) [56].

MEMS cell testers typically use optical measurements of beam deflections to estimate forces i.e. image analysis techniques output the deformation of compliant beams (of known elastic constant) allowing force calculations [49]. Alternatively, capacitive load sensors could be used for the same purpose. MEMS cells tester are usually designed in three different configurations [51]: A) pullers [31], [59]-[61] B) probes [62]-[65], and C) pillars [66]-[69]. A) Pullers consist of two bases or platforms that move apart from each other stretching the cell that is adhered to their top surface (Figure 3.2 (a)); compliant beams attached to the bases (one or both) act as load sensors. B) Probes are driven indenters able to poke the cell as they deflect compliant beams used to estimate the forces (Figure 3.2 (b)). C) Pillars consist of an array of closed spaced vertical beam pillars that the cell lies over (Figure 3.2 (c)); the cell can be electrically stimulated to contract while lateral and vertical forces can be estimated from the pillar deflections. Examples of these three configurations are provided in the next sub-section.

Another category of micro-devices used to investigate mechanical properties of individual cells are microfluidic platforms. In these devices cells go through tiny channels (cross-sectional dimensions on the micro-scale) where they, one by one, can have their elastic properties evaluated. Microfluidic cell testing devices can induce cell deformation via: aspiration, converging streamlines, and/or dielectric forces [51]. Cells are deformed by aspiration (Figure 3.2 (d)) when going through constricted channel geometries such as vertical gaps, wedges or funnel shapes. Mathematical models from micropipette aspiration can be used to analyze the cell mechanical properties when it deforms at the constriction [70]. When the cell is able to go through the channel constriction, the cell transit time or the entrance time could be used for the measurements [71]. Opposing fluidic stream lines that converge over the cell while it passes through the microchannel is another approach to promote cell deformation [72]. This mode prevents the cell from the contact with the channel's wall. Finally, cell deformation can be induced by forces originated in particles (cells in this case) suspended in a non-uniform electric fields (dielectrophoresis or DEP); however, the force calculation is imprecise since it depends on cell electrical properties which are hard to measure with accuracy [73].

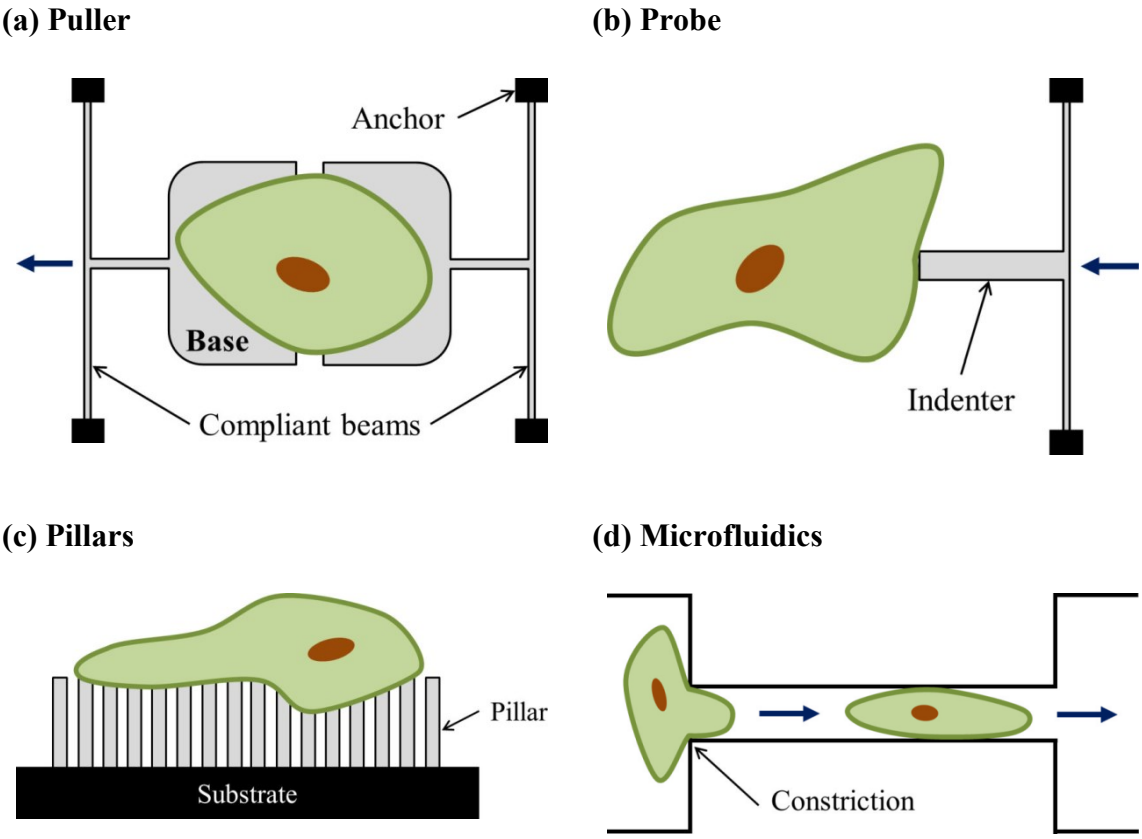

Figure 3.2: Design concepts of micro devices used to measure single cell mechanics: (a) puller, (b) probe, (c) pillars, and (d) microfluidics. Adapted from [51].

3.3.3 Examples of Mechanical Testing of Single Cells Using MEMS

A number of cell types have their mechanical properties investigated by MEMS devices of different designs and working principles; below several examples are provided.

Serrell [59] used a micro fabricated cell stretcher mechanically driven by an off-chip micro manipulator to test a single cell. The authors reported the linear force response of a hamster fibroblast (~50 µm size) up to 1.3 µN. Yang [62]-[64] used an off-chip piezo actuator to indent multiple monkey fibroblasts (~35 µm size). The cells showed a linear force response up to 0.4 µN when the fibroblasts started deforming plastically and showed hysteretic response during unloading. Zhang [74] used an on-chip electrothermal chevron actuator to compress one NIH3T3 fibroblast (~16 µm size) in cell medium by 25% of the cell initial size. Canine kidney cells were stretched by an on-chip electrostatic

MEMS device in biological media [60]. The cells (~20-40 μm size) showed stiffness on the order of 0.1 N/m. Subsequent work [61] included measurements of hysteresis and viscoelasticity of epithelial cells. Cardiac myocytes (~20 μm size) placed over a micro fabricated pillar array responded to external stimulus producing forces in the range of 10-200 nN [68], [69]. A monolithic MEMS microgripper consisting of an electrothermal actuator and electrostatic sensors was used to squeeze porcine aortic valve interstitial cells (PAVICs) [75]. The cells were grasped in a cell culture medium without immersing the actuator or the force sensors. A 15 μm PAVIC cell was deformed by 15% by a gripping force of 100 nN. The authors reported cell rupture using the gripper. Mouse zona pellucida oocytes and embryos (~50 to 60 μm size) were mechanically characterized by a MEMS two-axis cellular force sensor [65]. A micropipette attached to the electrostatic sensor was used to indent the cells up to their rupture while normal and tangential forces were measured. Embryos showed an elastic modulus 2.3x, and a puncturing force 1.7x that of oocytes.

3.4 Mechanics of Yeast Cells

Mechanical characterization of single yeast cells has been significantly explored in studies based on microplate compression and AFM technique. The microplate applied global forces and could be used as a cell rupturer, which gauged yeast cell's elastic properties and rupture force. The AFM was able to measure cell's local elastic properties and penetration force.

Using the microplate compression, Mashmoushy [53] was able to rupture single baker's yeast cells by squeezing them between a glass slide and an optic fiber probe (puncher) of 50 μm of diameter. An average cell rupture force of approximately 100 μN was measured. Later, similar apparatus were used to measure yeast cells (*Saccharomyces Cerevisiae*) rupture forces between 50 and 250 μN, and a rupture deformation of more than 50% of the cell initial size [76]-[80]. Additionally, Smith [80] calculated an average cell Young's modulus and surface modulus (stiffness) of approximately 110 MPa and 12 N/m respectively using a linear-elastic model for the cell wall. Smith [80] also detected a

slight increase in the stiffness of cells entering at the stationary phase supposedly due to an increase of the cell wall. According to Arfsten [76], the cells showed reversible deformation if compressed below their rupture force.

Some studies have used the AFM to nanoindent single yeast cells. Treating the cells (*Saccharomyces Cerevisiae)* as springs in series with the AFM cantilever probe, Arfsten [81] measured an average local cell stiffness of 0.32 N/m while Pelling [82] measured a stiffness of approximately 0.05 N/m. Ahmad [83] used a cantilever driven by a robotic nanomanipulator to indent hydrated single yeast cell. Using the Hertz model to fit the experimental data, the study calculated a cell Young's modulus of ~3.3 MPa and a penetration force in the 0.09-0.23 μN range. The fact that elastic modulus and rupture forces were 2 to 3 orders of magnitude lower compared to the microplate measurements may be explained by the fact that microplates measured global cell properties instead of performing local examinations. Finally, Touhami [46] also utilized the AFM and the Hertz model to compare the Young's modulus at a random location at the cell surface (*Saccharomyces Cerevisiae,* brewer's strain) to the Young's modulus at the cell bud scar (region where cell division occurred). The bud scar showed a Young's modulus 10x higher than at the other regions of the cell, ~ 6 MPa compared to ~ 0.6 MPa.

Even though many AFM and microplate compression studies investigated the same yeast species (*Sacaromises Cerevisae*), differences between reported measurements was sometimes orders of magnitude. For example the 3 orders of magnitude between the measured rupture force (microplate compression) and the penetration force (AFM) was likely due to the much lower contact area of the AFM probe.

In the next section, a MEMS design able to test the mechanical properties of yeast cells is introduced. Later sections compare the measured results to the other prior techniques, microplate compression and AFM.

Chapter 4: MEMS Squeezer Design

4.1 Design specifications

The MEMS platform was designed with the following design specifications:

1. Type of test:

   Compression testing rather than stretching or indentation was specified. Yeast cells are in general not adherent; stretching them would require a cell fixing mechanism or the use of functionalizing techniques to attach the cell to the substrate/MEMS. In addition, the small size of yeast cells (5 to 10 μm) could lead to an insufficient cell/MEMS adherent area. As for indentation, given the resolution limits of standard micromachining processes, MEMS would produce too coarse of a tip (micro vs. nano-scale).

2. Displacements:

   One of the goals of the MEMS squeezer was to deform yeast cells by 10-15% of the initial cell size, i. e. ~0.5-1 μm. The cell deformation is smaller than the input displacement due to the fact that compression is done against a compliant beam, which also moves. Thus the desired input displacement is in the 2-3 μm range.

3. Forces:

   In order to achieve the cell deformation above, the necessary MEMS forces were roughly estimated based on reported values of stiffness in the 1-10 N/m range [84]. Thus, the required compression forces are on the order of micro Newtons.

4.2 Chevron Electrothermal Actuator

In this study, two identical PolyMUMPs chevron electrothermal actuators were used to drive the cell squeezer mechanism underwater. The designed chevron has 140 μm long polysilicon (Poly 1) beams with 2x2 μm of cross section suspended 2 μm above the

substrate. The beams are anchored at one end and meet at the central shuttle at an angle θ of 6 degrees. The chevron anchors are connected to electrodes which are used to input a voltage difference over the chevron beams. The design was done using the CAD tool L-Edit™ and can be seen in Figure 4.1. Figure 4.2 shows a microphotograph of the PolyMUMPs chevron actuator microfabricated by CMC Microsystems. The presence of dimple arrays (moving and reference) will be explained in sections 4.7 and 5.5.

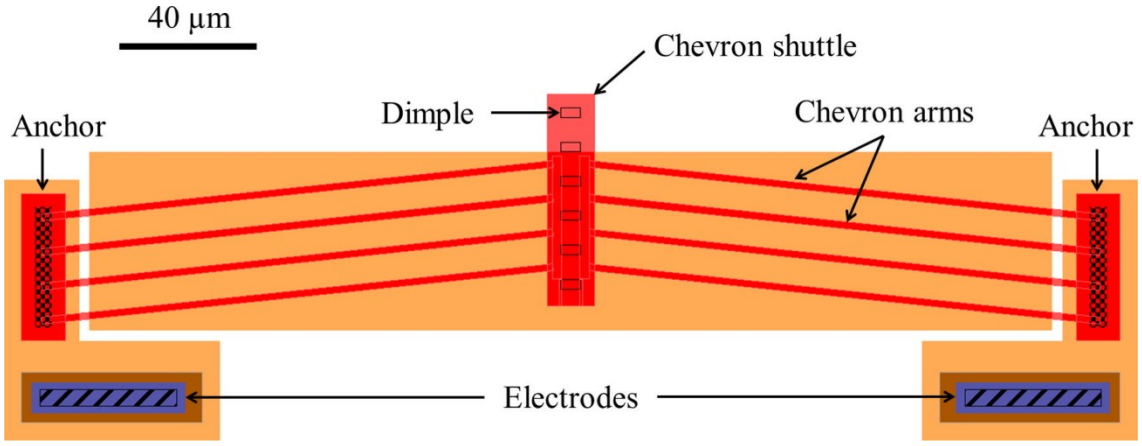

Figure 4.1: Design of the PolyMUMPs chevron thermal actuator.

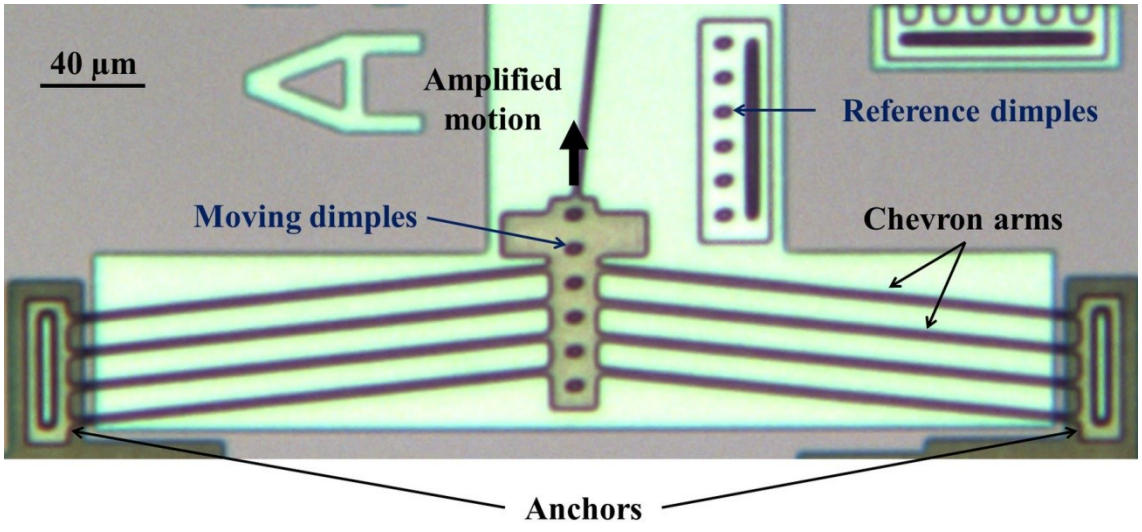

Figure 4.2: Microfabroicated PolyMUMPs chevron thermal actuator.

A current (few milliamps) passes through the beams from anchor to anchor causing Joule heating and thermal expansion of the beams. The small angle of the beams produces a

geometrical amplification of the thermal expansion (upwards motion on Figure 4.1 and Figure 4.2). As explained in section 2.6, the theoretical amplification factor is $1/\theta$ (~10x in this case since $\theta = 6$ degrees which is ~0.1 rad). In water even low DC voltages (~3 V) cause electrolysis that leads to bubble formation. This was avoided by using high frequency AC signals in which the RMS power acts as a DC input for frequencies higher than the system thermal cut-off frequency [30].

In a previous work [85] the temperature profiles of an unamplified chevron thermal actuator of similar design were simulated in air and water. In that study the simulated temperature rise at the chevron in air at 6 V_{DC} was approximately 300 °C. In water, at the same voltage (6 V_{RMS}), the simulated maximum temperature rise was significantly reduced to about 15 °C. The corresponding measured output motions were ~1 μm in air and below 0.10 μm in water. The study [85] also determined that the maximum applied voltage in water was limited to 12-13 V_{RMS} (due to bubble formation) resulting in a maximum displacement of ~0.35 μm.

4.3 MEMS Cell Testing Platform

Figure 4.3 shows the PolyMUMPs cell squeezer design with: A) 2 chevron electrothermal actuators, B) passive 'V" mechanical amplifier, C) jaw, and D) back spring. When activated the chevrons A) laterally push the mechanical amplifier B) extremities inwards producing an amplified transverse motion at the jaw C) The jaw motion (d_{jaw}) was used to compress single cells against the back spring that reacted by moving back (d_{spring}). Repeated patterns of dimples and 'optical combs' were used to measure the displacement of the moving parts via an FFT image analysis algorithm described in section 5.5. The circular loop at the back of the mechanical amplifier could be used (if needed) to mechanically push the jaw to eliminate stiction (see section 5.1). Figure 4.4 shows a microphotograph of the microfabricated cell testing platform. The following subsections describe in more details each part of the squeezer design, except the chevrons which were described in section 4.2.

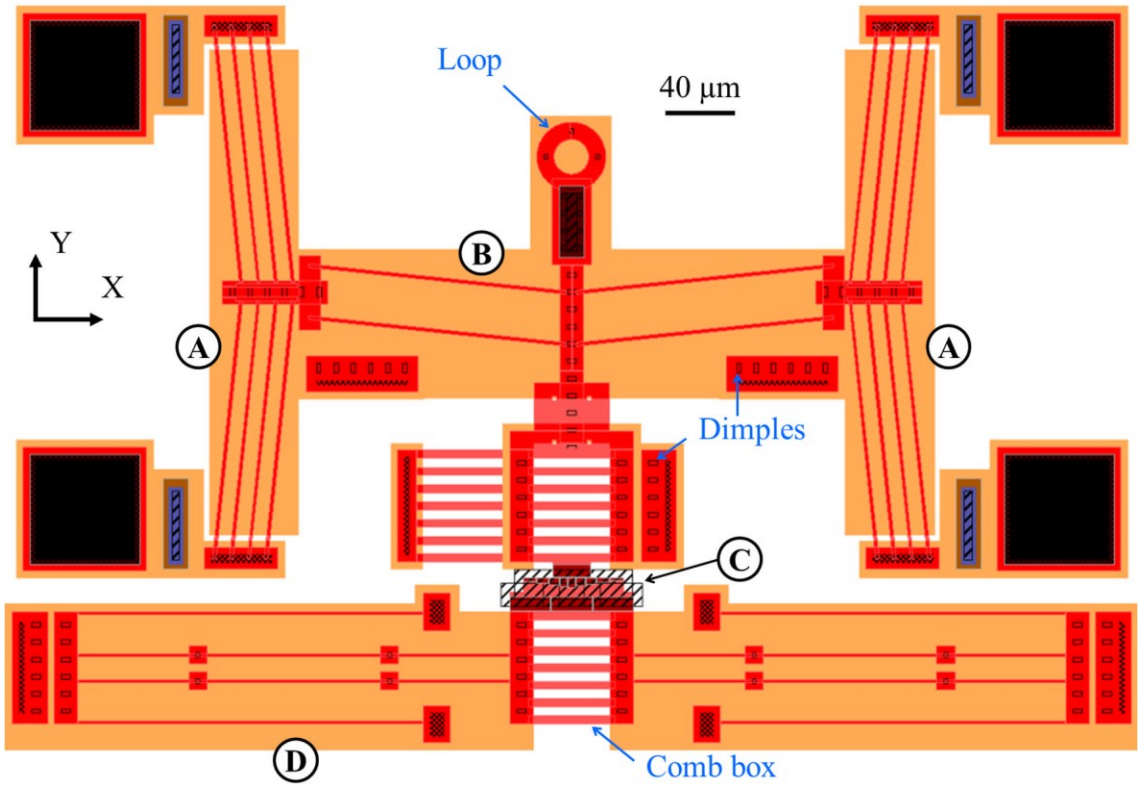

Figure 4.3: PolyMUMPS cell squeezer: A) chevron actuators, B) Passive double arm mechanical amplifier, C) jaw, and D) long back spring.

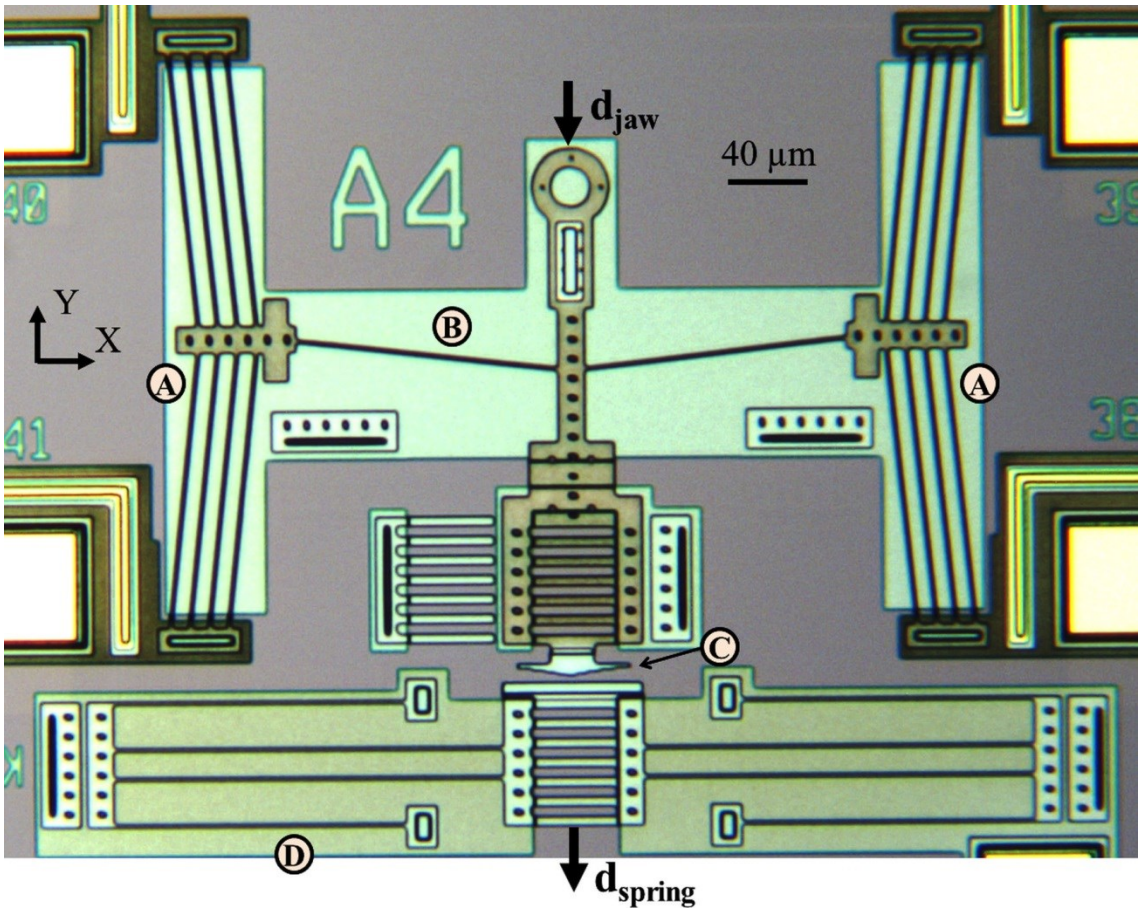

Figure 4.4: Microfabricated PolyMUMPs cell squeezer: A) chevron actuators, B) single arm mechanical amplifier, C) jaw, and D) stiffer short back spring.

4.4 Mechanical Amplifier

Because the maximum displacement of the chevron actuator underwater was 0.35 µm [85], a mechanical amplifier was implemented to increase this motion. It was designed as a 6 degree V-shaped bent beam amplifier with a theoretical kinematic amplification of ~10x. The ends of the amplifier were attached to the chevron shuttles while its central shaft was connected to the squeezer jaw. The motion of amplifier's central shaft or the jaw motion (d_{jaw}) is the final amplified motion used to squeeze individual cells. Figure 4.5 shows the two types of mechanical amplifiers tested at the squeezer. The single arm amplifier is less stiff than the double arm amplifier and therefore should provide a slightly larger final displacement, d_{jaw}.

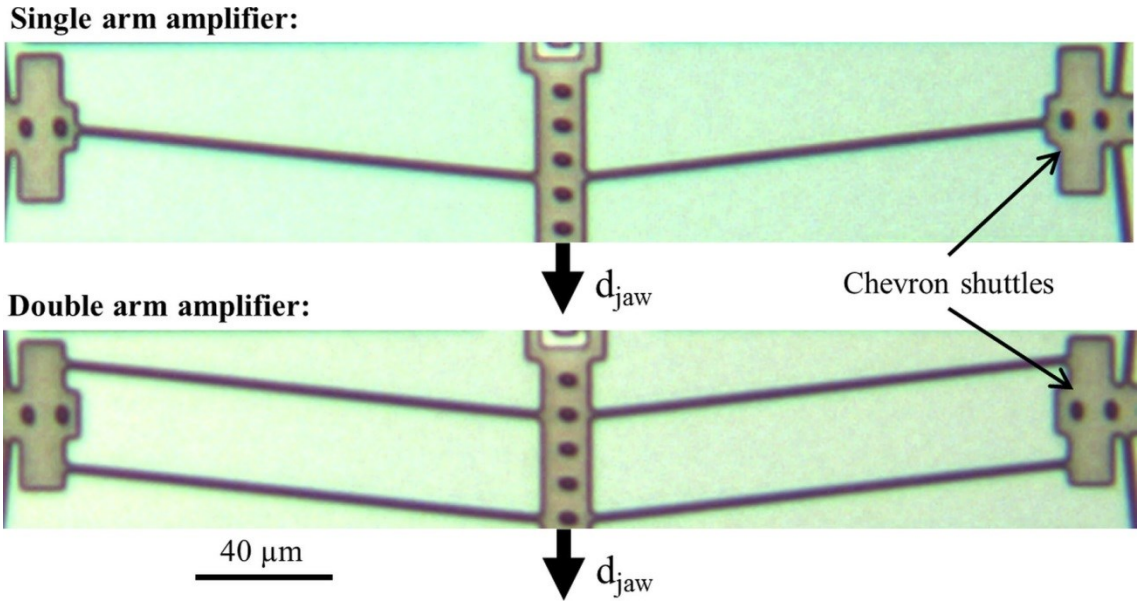

Figure 4.5: Microphotographs of the single and double arm amplifiers.

4.5 Squeezer Jaw

The jaw was manufactured using the PolyMUMPs double layer (Poly 1 plus Poly 2, 3.5 µm thick, 2 µm above substrate). The higher thickness at the jaw provided a higher contact area with the cell during compression. The MEMS part where the cell is compressed against is the back spring wall (see next section) which was also designed with the thicker layer. The jaw was modeled with multiple steps to provide squeezing gaps ranging from 4.5 to 8.5 µm. This configuration allowed the compression of cells with different sizes. Figure 4.6 shows the top view and the cross section of the jaw designed in L-Edit™. Note that in order to allow multiple jaw steps and simultaneously keep the jaw total width small and close to the centerline, the flat sections of each jaw step are relatively short. As a result, in some tests the cell would be in contact with the flat section and also with the side wall of the jaw step, leading to a not perfect parallel compression. This would result in an increase of the contact area, the effects of which are discussed in section 7.4. In order to create the double height structure, a laminated Poly 1 Poly 2 VIA layer was used; this layer indicates where Oxide 2 should be removed so as to Poly 2 be deposited directly over Poly 1. Note in Figure 4.6 that the over-etch of Poly

2 is sufficient to eliminate the single layer Poly 1 (light pink) located under the VIA layer, leaving the gap between the jaw and the back spring.

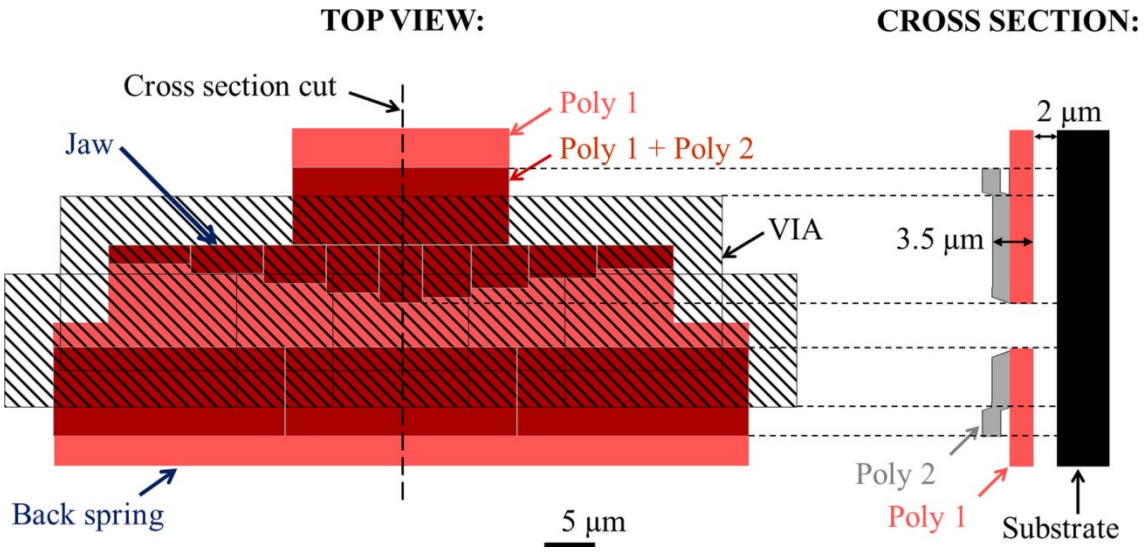

Figure 4.6: Design of the jaw with multiple steps (see TOP VIEW) and double height structure (see CROSS SECTION VIEW).

If we approximate the yeast cells as oblate spheroids with approximately circular cross sections, then cells with diameters ranging from 4.5 to 8.5 µm can be clamped at their mid-section at different locations on this particular jaw design. Figure 4.7 (a) shows a microphotograph of the jaw after fabrication (top view) and Figure 4.7 (b) shows an illustration of cells of different sizes placed at the jaw (side view). Figure 4.8 shows a scanning electron microscope image (SEM) taken at a 45° angle of the jaw and part of the back spring. Note the double height structures of 3.5 µm compared to the less thick parts made of a single Poly 1 layer.

Once a cell is placed at the test location, the jaw compresses it by pushing it against a back spring (or reference spring) of known elastic constant. Figure 4.9 (a) shows a microphotograph of a cell positioned at one of the jaw's gaps (top view) while Figure 4.9 (b) shows a side view sketch of the same cell.

(a) TOP VIEW: (b) SIDE VIEW (sketch):

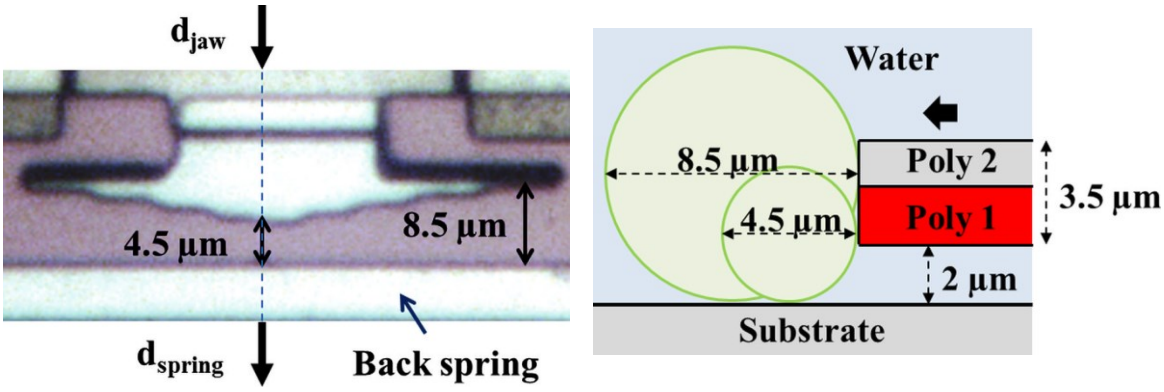

Figure 4.7: (a) Top view microphotograph of the multi-step jaw. (b) Side view illustration of cells of diameters ranging from 4.5 to 8.5 µm placed at the test location.

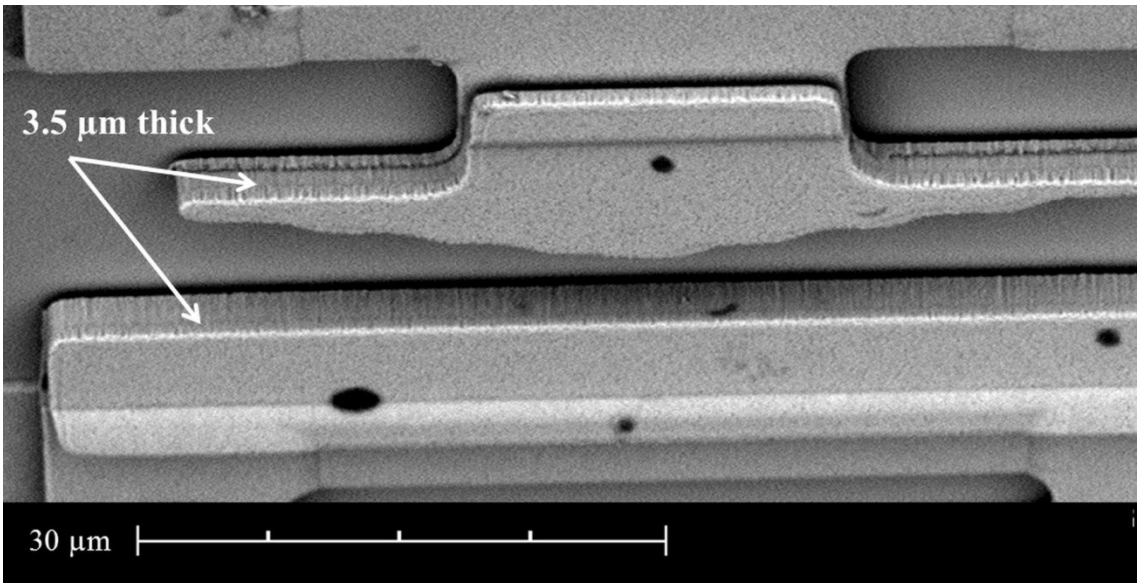

Figure 4.8: SEM image at 45° of jaw and back spring wall double height structures for cell squeezing.

(a) TOP VIEW:

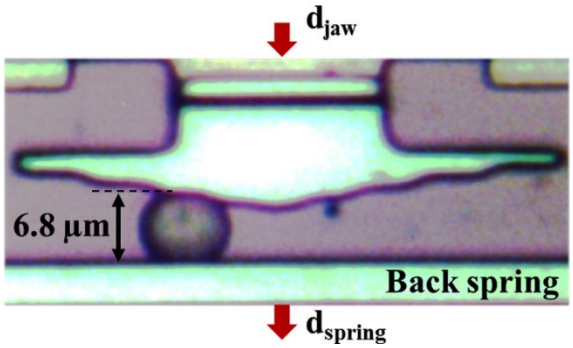

(b) SIDE VIEW (sketch):

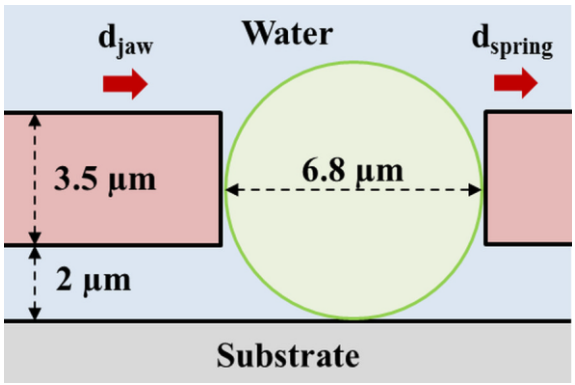

Figure 4.9: (a) Top view microphotograph of a cell located at one of the jaw's gap. (b) Side view sketch of the same cell.

Figure 4.10 shows more SEM images of the jaw (Poly 1 plus Poly 2, double height structure). Note the vertical striations (Figure 4.10 (b)) indicating sidewall roughness. Miller [86] reported peak surface roughness of PolyMUMPs of ~30-100 nm, but no sidewall roughness was given for PolyMUMPs. The presence of these sharp asperities on the jaw sidewalls may increase the local contact stress.

(a)

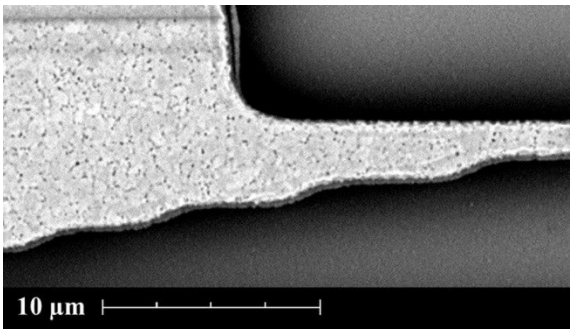

(b)

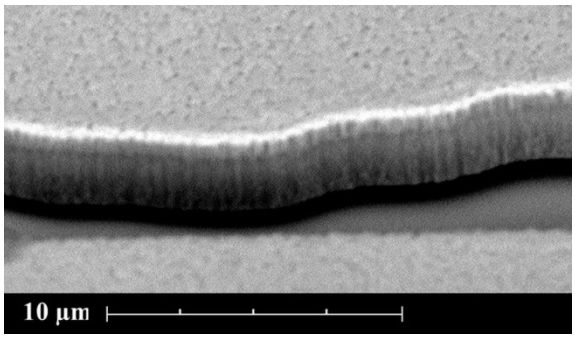

Figure 4.10: SEM images of the cell test location. (a) Top view: surface roughness of polysilicon. (b) 45° view: note vertical striations of the sidewalls.

4.6 Back Spring

The back spring or reference spring is a 2 stage folded accordion type suspension which has selective compliance to allow motion in only one direction. The back spring has four longer arms with length L_1 (stage 1) and other four shorter arms with length L_2 which have one of their ends anchored to the substrate (stage 2). Figure 4.11 shows a back spring designed to move only in the Y direction. Although not shown here the back jaw attached to the central section of the back spring was designed as a double height structure as can be seen in Figure 4.6 and in Figure 4.8.

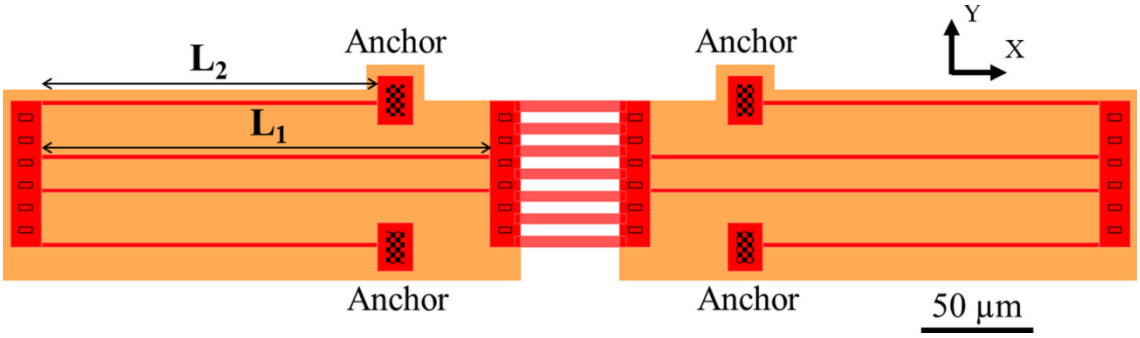

Figure 4.11: Design of the back spring done in L-edit.

The transversal (Y direction) stiffness of each stage of the back spring was calculated using the following relation considering a concentrated center load [87].

$$k_{stage} = 2\left[\frac{192EI}{(2L_n)^3}\right] \tag{6}$$

Where E is the Young's Modulus of polysilicon (160 GPa), n is the stage number (1 or 2), and I is the moment of inertia of the beam given by:

$$I = \frac{bh^3}{12} \tag{7}$$

As b = h = 2 μm (width and height of the beam) the moment of inertia I is 1.33 μm^4. Since the spring stages are in series the total transversal stiffness of the back spring is given by:

$$k_{spring} = \frac{k_{stage\,1} \cdot k_{stage\,2}}{k_{stage\,1} + k_{stage\,2}} \tag{8}$$

Back springs with two different combinations of L_1 and L_2 were designed. In the first design L_1 and L_2 were 200 and 150 μm respectively; in the second design L_1 and L_2 were 250 and 200 respectively. The stiffness of both back springs was calculated by substituting the results from equation 6 on equation 8. The calculated stiffness of the spring with shorter arms was 0.90 N/m while the stiffness of the spring with longer arms was 0.43 N/m. The springs' stiffness were also estimated with FEA simulations as shown in section 6.5. Figure 4.12 shows microphotographs of the two back springs used in this study.

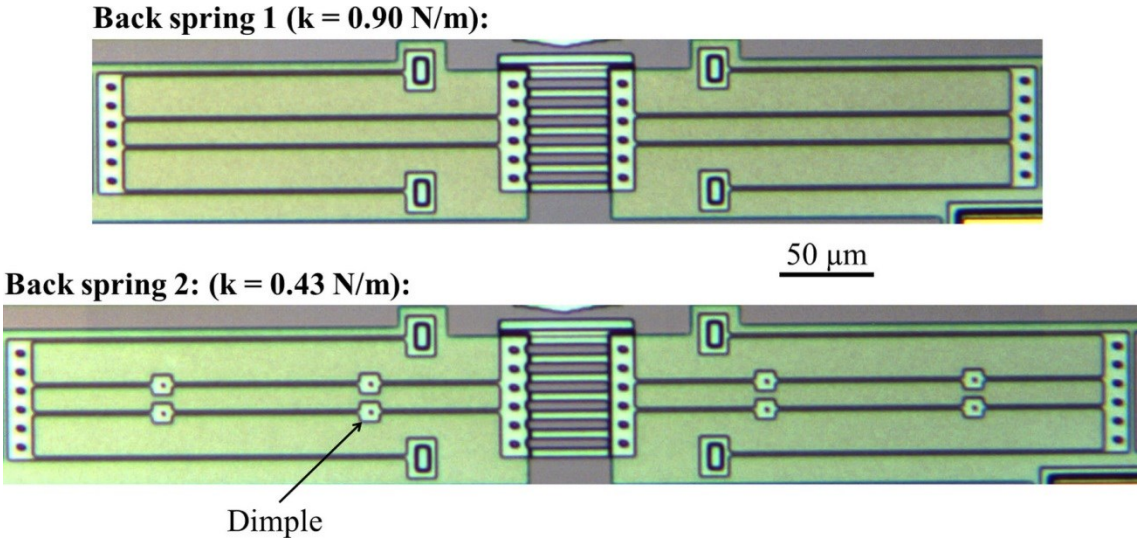

Figure 4.12: Microphotographs of the two back springs used in the cell testing.

4.7 Combs and Dimples

In order to measure the displacement of the input motions (chevron and jaw) and the output motion (back spring) equally spaced comb structures (comb boxes) and dimples were attached to: the chevron central shuttle (Figure 4.13 (a)), the central section just prior to the jaws (Figure 4.13 (b)), and the center of the back spring (Figure 4.13 (b)). Additional fixed reference comb and dimples were attached to the substrate adjacent to the jaws, so as to measure and subsequently remove any frame motion (Figure 4.13 (b)).

(a) (b)

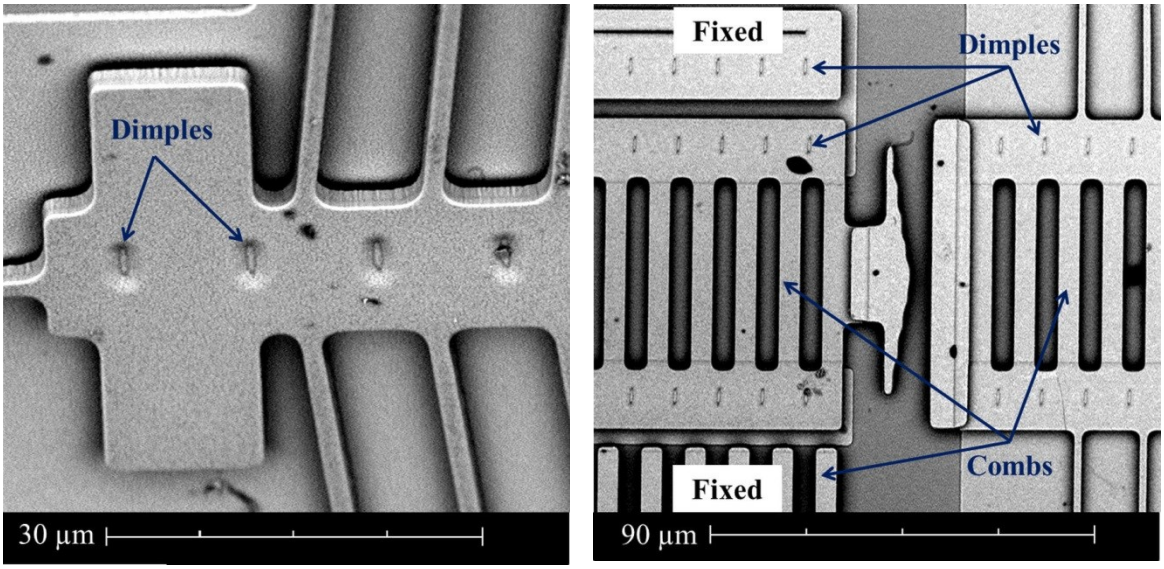

Figure 4.13: SEM images of: (a) 45° VIEW, dimples etched on the chevron shuttle; (b) TOP VIEW, comb structures and dimples: attached to jaw and back spring, and fixed to the substrate.

4.8 Lumped Model

A two stage spring model was used to calculate the cell stiffness. When two springs are in series the ratio of their elastic constants is a function of the ratio of their deformation. Therefore, one can calculate the stiffness of a spring in series with another spring of known stiffness by measuring their relative deformation. In this study the cell is the spring with unknown stiffness (k_{cell}) while the back spring is the spring with known

stiffness (k_{spring}). Figure 4.14 shows the lumped model of the system: the squeezer provides a force that pushes the cell in series with the back spring which is fixed to the substrate. The back spring deformation is d_{spring} while the cell deformation is the difference between the jaw motion (d_{jaw}) and the back spring motion, d_{jaw} - d_{spring}.

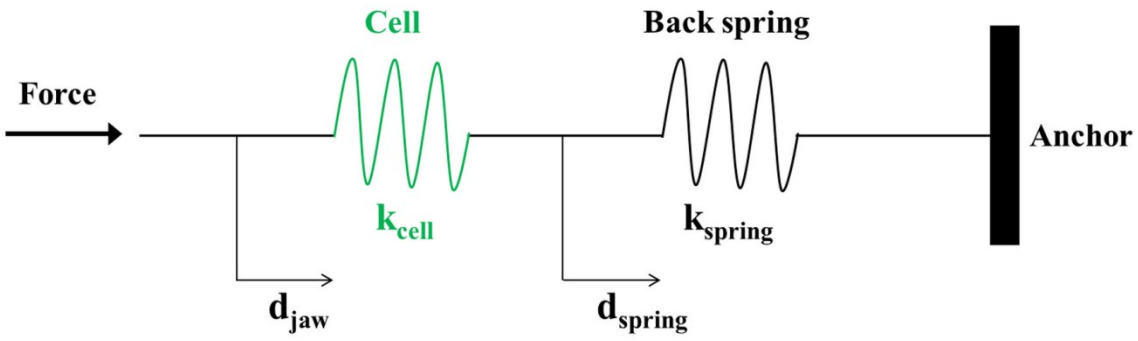

Figure 4.14: Lumped model of the cell testing mechanical system.

The force on a spring is its deformation multiplied by its elastic constant. Therefore, the force on the back spring and on the cell can be calculated by equations 9 and 10 respectively shown below.

$$F_{spring} = d_{spring} \cdot k_{spring} \tag{9}$$

$$F_{cell} = (d_{jaw} - d_{spring})\, k_{cell} \tag{10}$$

Since the cell and the back spring are in series the force over each of them is the same. Equating both forces we get:

$$k_{cell} = \left(\frac{d_{spring}}{d_{jaw} - d_{spring}}\right) k_{spring} \tag{11}$$

Hence, knowing the back spring elastic constant it is possible to calculate the cell stiffness by measuring the displacements of the jaw and of the back spring. This approach was validated in [84]. According to the study [84] if a ratio of springs' constants equals

unity ($k_{cell}/k_{spring} = 1$) it would lead to the minimum error in the measured cell stiffness, but accurate measurements can still be achieved if the k ratio is not too large. Therefore, the values for the back spring stiffness should be similar to the values of cell stiffness. This result is intuitive since if $k_{spring} << k_{cell}$ the cell deformation would be negligible (difficult to measure with accuracy) and if $k_{srping} >> k_{cell}$ the back spring deformation would be negligible.

Chapter 5: Experimental Set up

5.1 Chip Inspection and Manipulation

The MEMS design was microfabricated, diced and packaged by CMC Microsystems. 15 packaged dies (5x5 mm), as can be seen in Figure 5.1, were delivered. Firstly, the chip was visually inspected under a Wentworth™ Probe station microscope (Figure 5.2 (a)). A Point Grey™ colour CCD camera (1280 × 960 pixels) attached to the microscope transmitted the chip image on a screen located over the microscope (Figure 5.2 (b)). After checking for fabrication problems, MEMS structures were tested in air to verify if they worked properly. An electrical board (Figure 5.3(a)) was used to apply voltage to the chip mounted over the microscope stage (Figure 5.3(b)).

(a) (b)

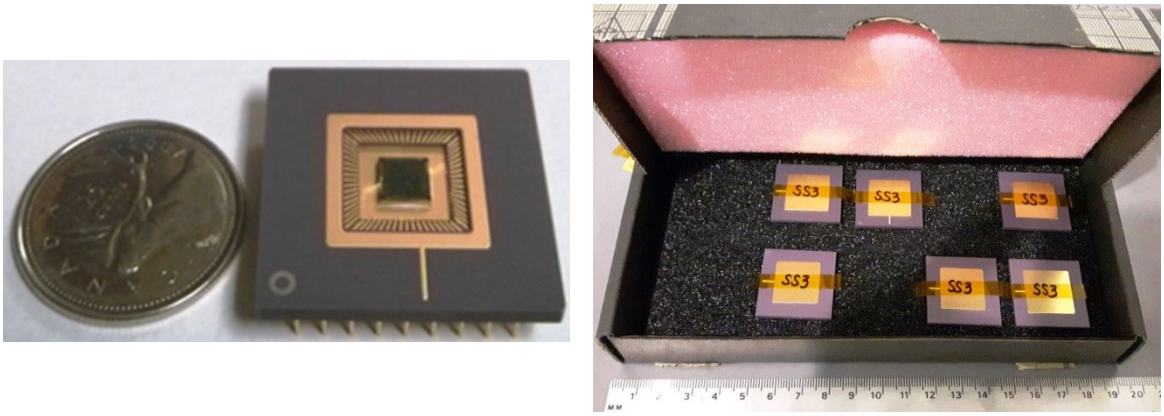

Figure 5.1: (a) Packaged die after microfabrication (b) Foam box with 15 chips.

(a) (b)

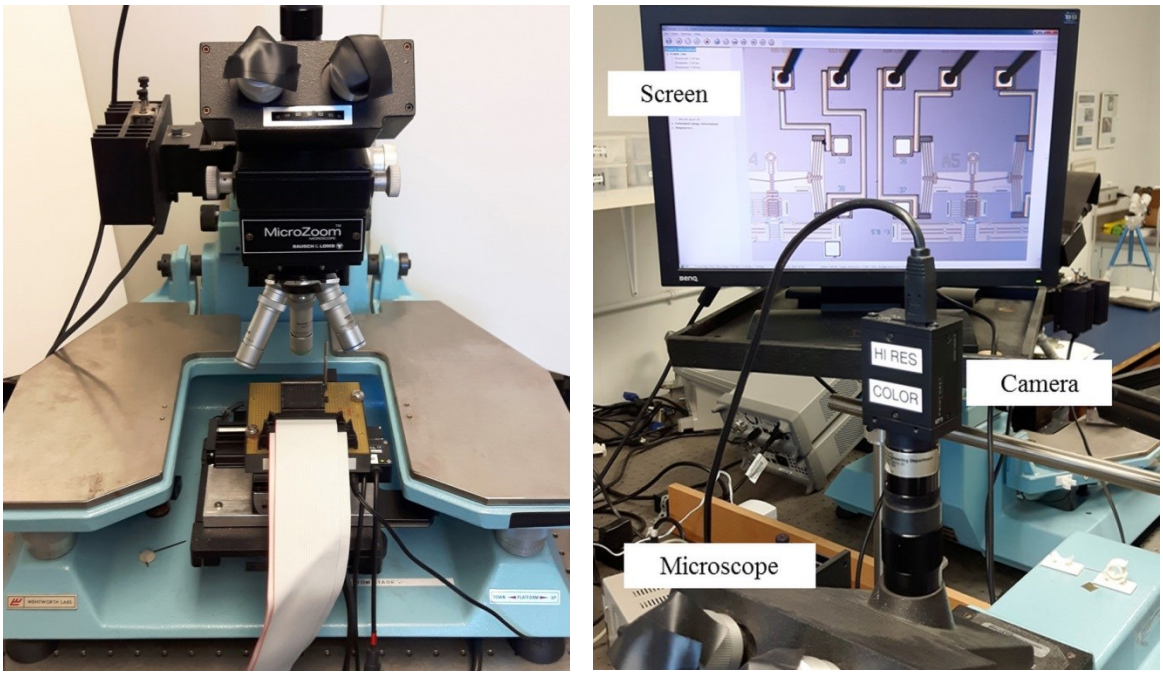

Figure 5.2: (a) Probe station microscope. (b) Colour CCD camera attached to the microscope and screen showing the magnified image.

(a) (b)

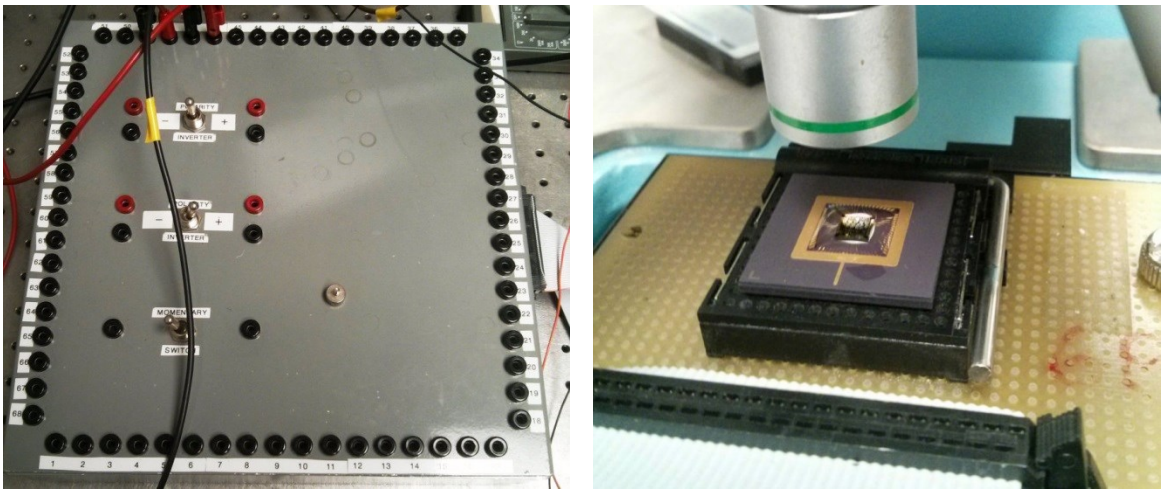

Figure 5.3: (a) Electrical board used to activate the chip (b) Chip mounted over the microscope stage.

In order to avoid stiction the chip was let stand in methanol for at least 24 hours. The chip's actuators were then tested underwater (tap water). If their motion were considered

adequate and repeatable the chip was considered good to work in aqueous media. However, sometimes the actuators did not move or their motions were too short and not repeatable indicating that stiction was still holding them. In this case, an acupuncture needle (J-type from Seirin) mounted over a Wentworth™ mechanical 3D manipulator was used to poke the MEMS structures (Figure 5.4) in order to help releasing air pockets stuck under the beams. Although this was a delicate and risk prone procedure, it was usually effective on eliminating stiction.

(a)

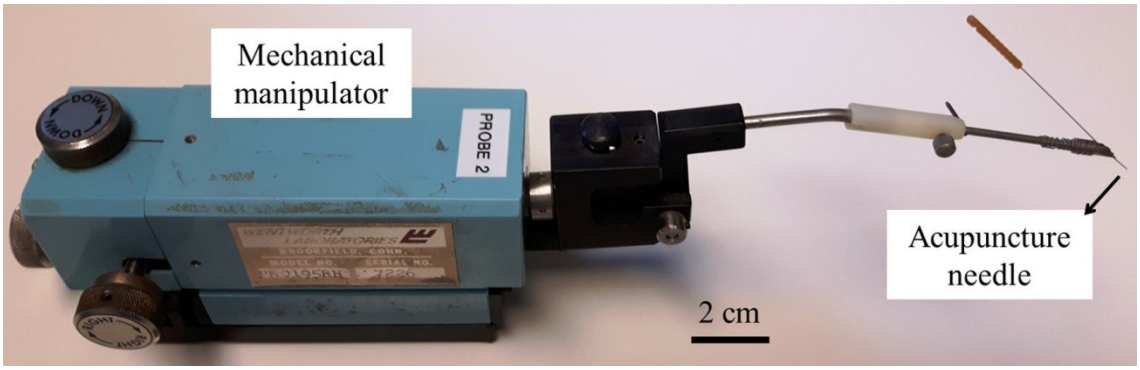

(b)

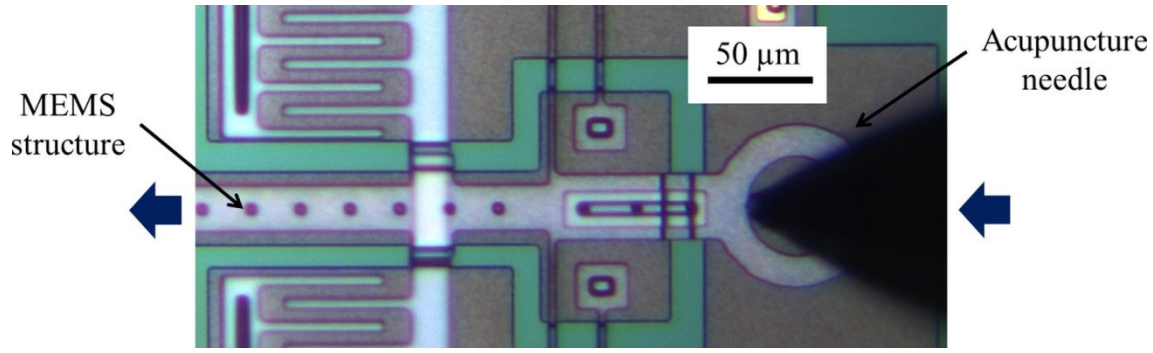

Figure 5.4: (a) Acupuncture needle attached to the 3D manipulator. (b) Using the acupuncture needle to push MEMS structures underwater so as to eliminate stiction.

Once the chip was considered free from stiction it could be used for experiments. Before every test, the chip was removed from methanol and rinsed with deionized water (DI water) to clear it from methanol. The chip's borders and electrical pins were then dried out using wipes (Kimwipes® Low-Lint). If a cell test was to be conducted, the die was let stand until it completely dried out so the cells could be placed on it (see section 5.3 for

more details). If the MEMS structures were to be tested, there was no need to wait until the die to dry (see section 8.1 for more details). After the test the chip was rinsed with methanol and returned to a container (Figure 5.5) where it was immersed in methanol until the next test.

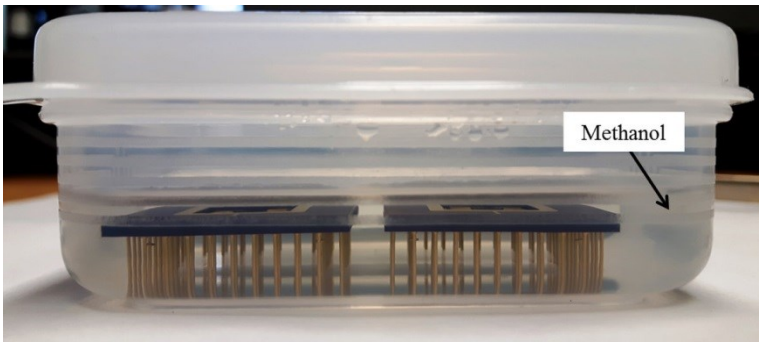

Figure 5.5: Chips stored in a container while immersed in methanol.

5.2 Cell Preparation

5.2.1. Baker's Yeast

Baker's yeast cells (*Saccharomyces cerevisiae*) were prepared by mixing yeast (Fleischmann's active dry yeast, Figure 5.6 (a)) and sugar in 15 ml of filtered water at 38°C as indicated on the product's package. Yeast, sugar and water were mixed at volumetric ratios of 11:5:60 respectively. The solution was left to stand for 24 hours. Then 0.12 ml of the cell culture was diluted in 20 ml of filtered tap water. A small drop (4 µl) of methylene blue 1% (from Fisher Science Education) was added to the diluted solution in order to allow visual differentiation of viable and non-viable cells under the microscope. Methylene blue is a common stain used for yeast; non-viable yeast cells become blue due to the intake of the substance (Figure 5.6 (b)).

(a) (b)

Figure 5.6: (a) Fleischmann's active dry yeast package (b) Viable and non-viable cells observed under the microscope.

5.2.2 Brewer's Yeast

The two industrial brewer's yeast strains chosen for this study are listed in Table 5.1. The industrial lager strain (SMA) is often used in research and in malt quality assays.

Table 5.1: Brewing yeast characteristics

Species	Strain	Genotype	Source
Ale (*S. cerevisiae)*	Nottingham ale	Industrial strain	Lallemand
Lager (*S. pastorianus)*	SMA	Industrial strain	Wyeast

The following yeast preparation was performed by Dr. Andrew J. MacIntosh, from the Process Engineering and Applied Science Department of Dalhousie University.

To attain yeast at various phases of fermentation, a miniature fermentation assay [88] was carried out with Canadian pale malt, which was used as a control malt for fermentations in [89]. The yeast was taken from agar slants and propagated for 24 h in volumetric flasks containing Yeast-Extract, Peptone, and Dextrose (YEPD) growth medium while shaken at 100 RPM at 30 °C [88]. Small fermentation tubes (containing 15 mL of wort each) were pitched (yeast was added to the wort) at a rate of 1.5×10^7 cells/mL and allowed to

ferment at 21 °C for 7 days. Figure 5.7 shows the reduction of sugar (extract) in the tube (%) as it was consumed by the yeast during fermentation. The ale strain was shown to ferment slightly faster than the lager. Samples were taken at approximately 0 h (start), 46 h (middle) and 94 h (end) and diluted to ~1×10^6 cells/mL prior to mechanical analysis. These specific sampling times were chosen in an attempt to capture characteristics of cells that were: propagating in the presence of oxygen (start), actively fermenting (middle), and entering the stationary phase (end).

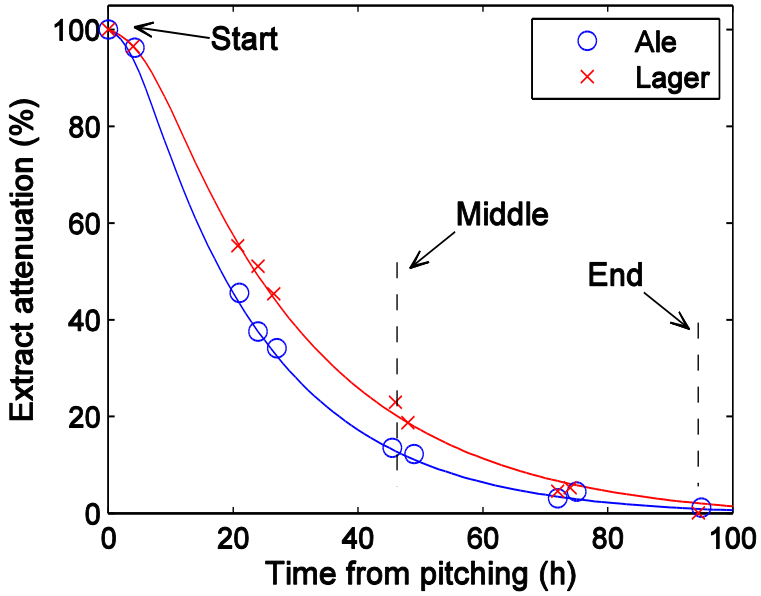

Figure 5.7: Sugar consumption over the assay fermentation conducted. Both fermentation curves were modeled using the logistic model described in ASBC Yeast-14. Data provided by Dr. Andrew J. MacIntosh.

5.3 Cell Placement

A small drop (~4 µl) of the diluted solution of baker's or brewer's cells was placed on the dried 5x5 mm MEMS chip die near the squeezer structures using hand pipetting (Figure 5.8 (a)). The drop was left to stand for 5 minutes so that the cells settled down on the chip surface. The entire chip area was then flooded (Figure 5.8 (b)) with a dilution solution (20 ml of filtered water plus 4 µl of methylene blue). The cells on the chip remained confined within a 300 to 500 µm radial distance.

(a) (b)

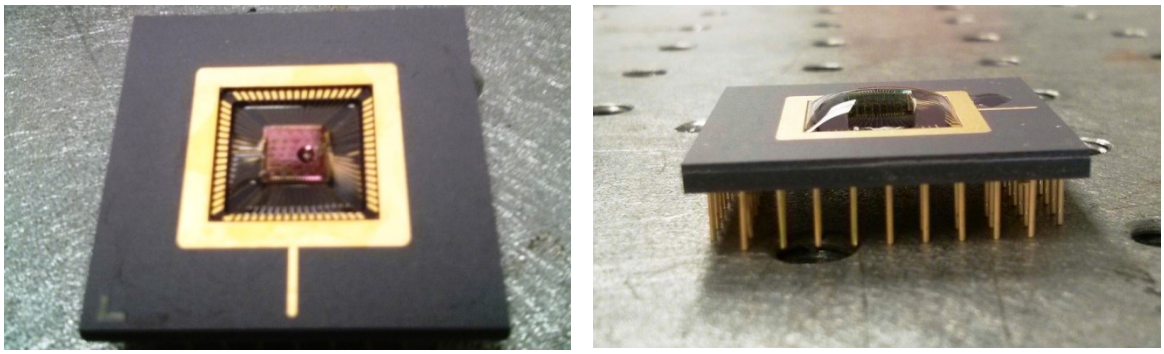

Figure 5.8: (a) Small drop of cell solution placed at the chip die. (b) Chip flooded with the dilution solution.

The cells were individually moved to the test location (between the jaw and back spring) utilizing micropipettes and a 3D micromanipulator driver. Micropipettes (FivePhoton™, inner tip diameter: 3 µm, outer tip diameter: 5 µm) were attached to a Hamilton™ pipette holder which was mounted on a Zaber™ XYZ micro-positioning system controlled by a joystick (Figure 5.9).

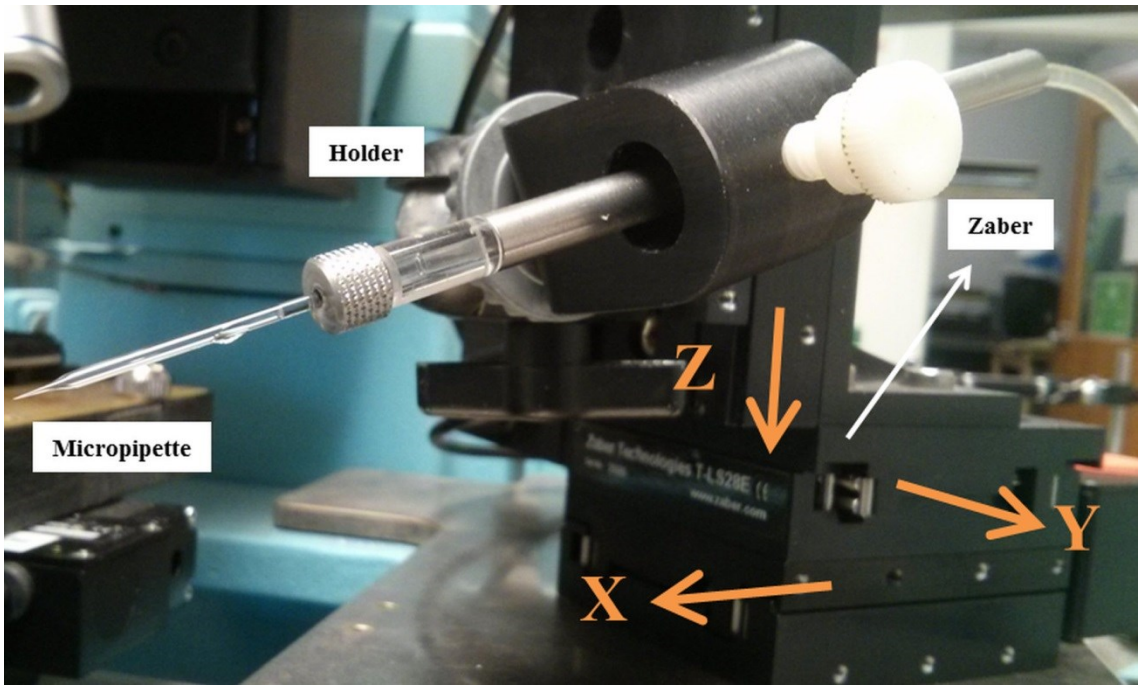

Figure 5.9: Micropipette fixed to the holder which is attached to the Zaber manipulator.

Once inserted underwater (Figure 5.10 (a)), the micropipette was driven to the selected viable cell and the cell was aspirated onto the pipette by applying negative pressure. The aspiration pressure was kept low to avoid sucking the cell into the pipette and damaging the cell (see suction device in Figure 5.10 (b)). The cell was then brought to the size matching jaw stage and released by removing the aspiration pressure. Figure 5.11 schematically summarizes the entire cell placing procedure. This manipulation procedure required 15-25 minutes (for each cell) mainly due to difficulties in handling individual cells with the micropipette.

(a) (b)

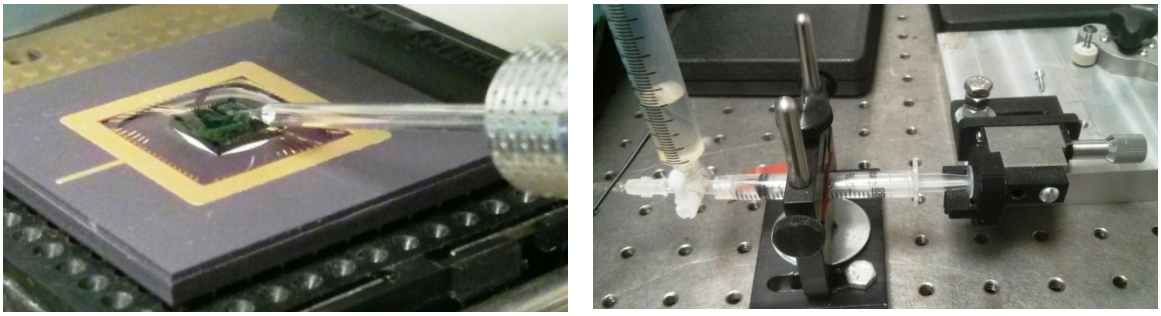

Figure 5.10: (a) Micropipette inserted underwater. (b) Suction device.

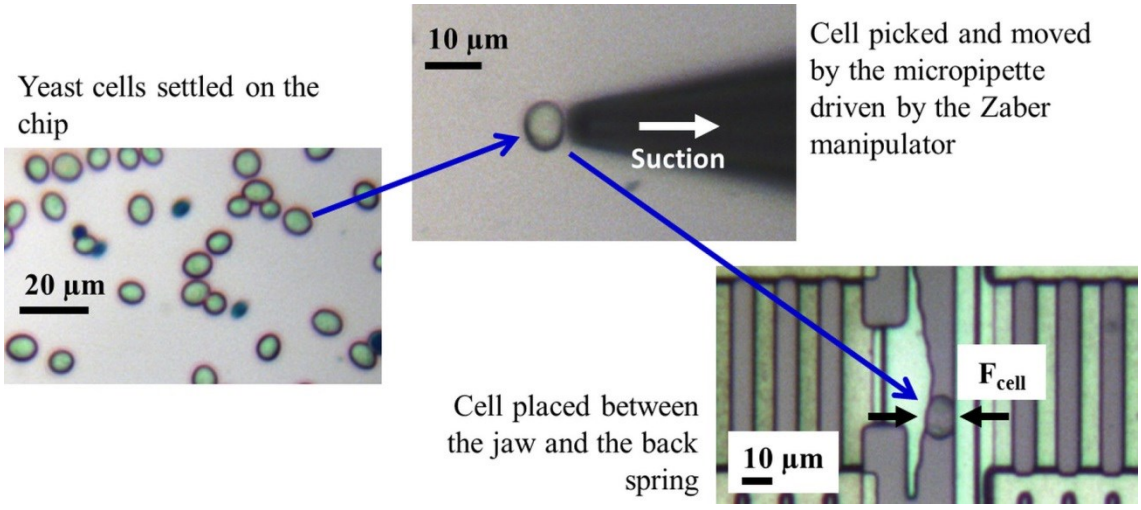

Figure 5.11: Viable cell captured, moved and placed in between the jaws and the back spring.

5.4 Cell Squeezing and Data Acquisition

For all tests underwater the chevron actuators were driven by a function generator (Keysight™ 33210A 10MHz) in series with a voltage amplifier (Thorlabs™ HVA200). AC sinewaves of 1 MHz were generated and the voltage amplified by a factor of ~15x to drive the device. The high frequency input avoids water electrolysis [30] and the RMS voltage of the signal works as a DC source activating the thermal actuators. In most squeezing cycles the driving voltage was incremented several times by a fixed voltage step until the final voltage was reached; then, the voltage was incrementally reduced by the same steps to zero volts. The Point Grey™ colour CCD camera (1280 × 960 pixels) attached to the Wentworth™ Probe station microscope, acquired an image at every voltage step. For the configuration used (25x objective, 2x zoom), the measured pixel size of the images is 144 nm. All the apparatus used in this process (function generator, electrical amplifier, oscilloscope and microscope camera) were automatically controlled by a LabVIEW algorithm. Between each voltage change and the image acquisition there was delay of 0.25 seconds. A complete squeezing cell cycle with 10 voltage steps lasted approximately 13 seconds and returned 11 images, approximately 1.2 seconds per image. In the end, a sequence of pictures showing the MEMS motion as the voltage change is saved at the computer hard disk. Figure 5.12 shows a schematic representation of the data acquisition procedure.

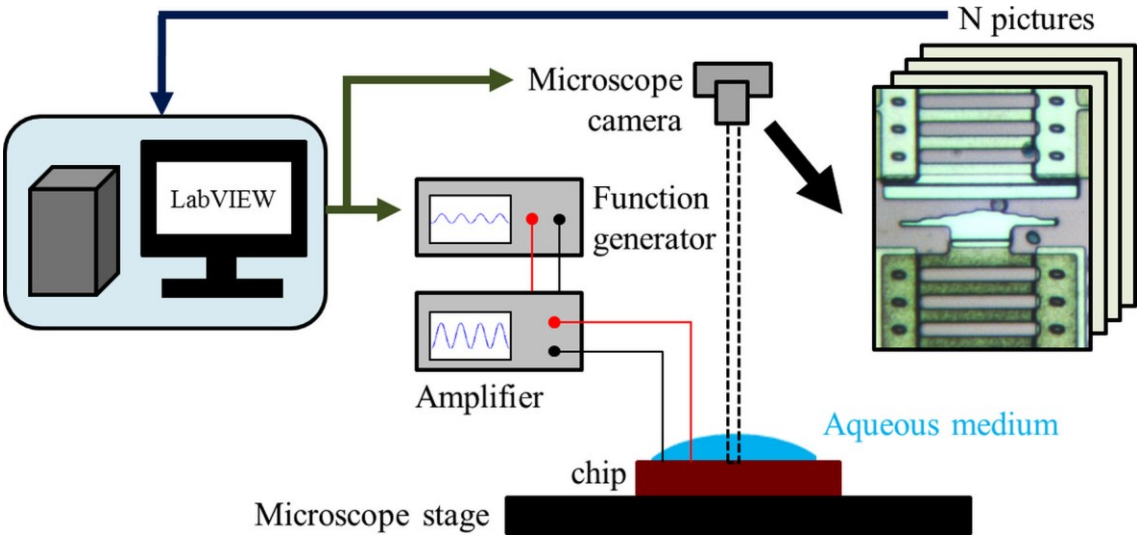

Figure 5.12: Schematic representation of the general data acquisition procedure.

5.5 FFT Image Analysis

The camera photographs taken during one cycle captured moving and fixed periodic structures (combs or dimples). The moving structures are attached to the actuator (chevron shuttles and jaw) and to the back spring; and the fixed reference structures are attached to the substrate (see Figure 4.1 to Figure 4.4). The images were cropped to the region of interest (ROI) around the periodic structures and the ROI was then column averaged to produce a one dimensional pixel light intensity profile which is a waveform with a defined wavelength (10 μm in this case) and phase (Figure 5.13).

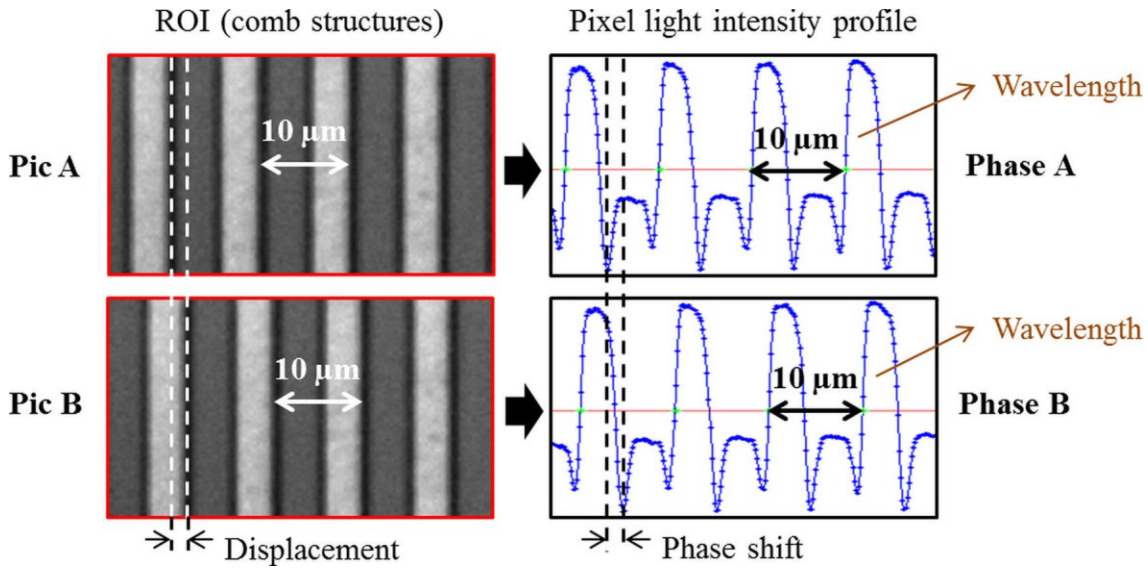

Figure 5.13: Pixel light intensity profile of ROIs of two different photographs. The photographs have different phases but the same wavelength, 10 µm.

Based on the technique developed by Yamahata et al [90] a Fast Fourier Transform (FFT) was performed on the pixel intensity profiles and returned the phase shift of each picture in relation to the first picture. The phase shift is multiplied by the spatial wavelength to calculate the displacement. See an illustration of the entire image analysis procedure in Figure 5.14.

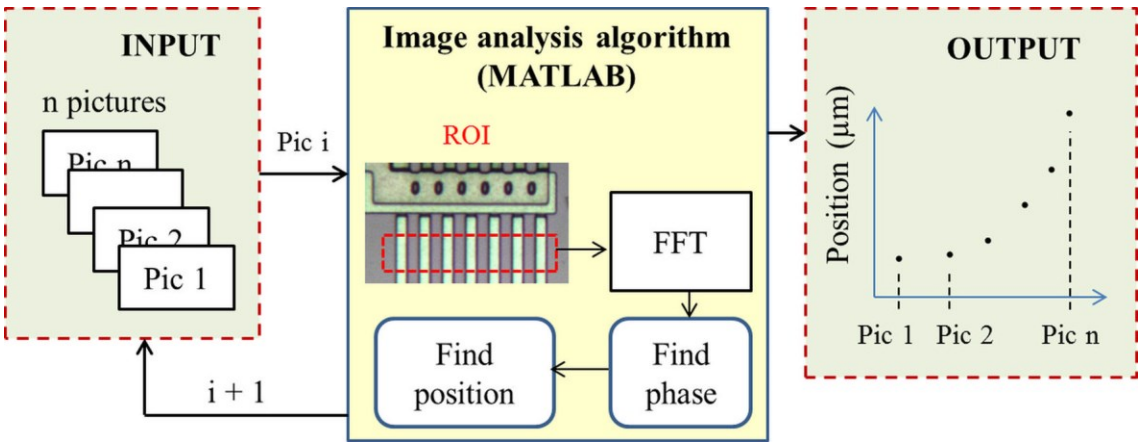

Figure 5.14: Schematic illustration of the data analysis procedure.

The motion of the reference structure was subtracted from the motion of the moving parts (actuator and back spring) to remove frame vibrations. This method was shown to have a resolution on the order of 10 nm underwater [91].

The main sources of errors of this analysis were associated to vibrations and image contrast. In order avoid vibration tests were conducted over an anti-vibration table. Good image contrast was important for the algorithm to accurately detect the profile of the periodic structures (combs and dimples). In order to increase the contrast Poly 0 was removed from underneath the comb structures as can be seen in Figure 4.3. The contrast between the combs (Poly 1) and the Nitride was higher than the contrast between the combs and Poly 0.

Chapter 6: MEMS Squeezer Simulations

6.1 Actuator Model Set up

One concern with the use of thermal actuators is the temperature increase at the cell test location. Therefore, finite element analysis (FEA) was used to predict the temperature distribution over the MEMS actuator. Furthermore, the analysis also calculated the device's performance (motions of chevrons and jaws) in order to compare with the displacement measurements.

The FEA was performed using a 3D mesh over the entire geometry of MEMS squeezer actuator. The two dimensional design of the cell tester actuator was imported from the CAD tool L-Edit™ to COMSOL™ and then extruded in the 'z' direction by 2 µm, the height of Poly 1 layer. After the actuator geometry was set up, one of the anchors of each chevron was defined as the electrical ground while the others the electrical potential. Moreover, all 4 anchors (2 for each chevron) were set as fixed mechanical constraints. Figure 6.1 shows the 3D final geometry used for the simulations.

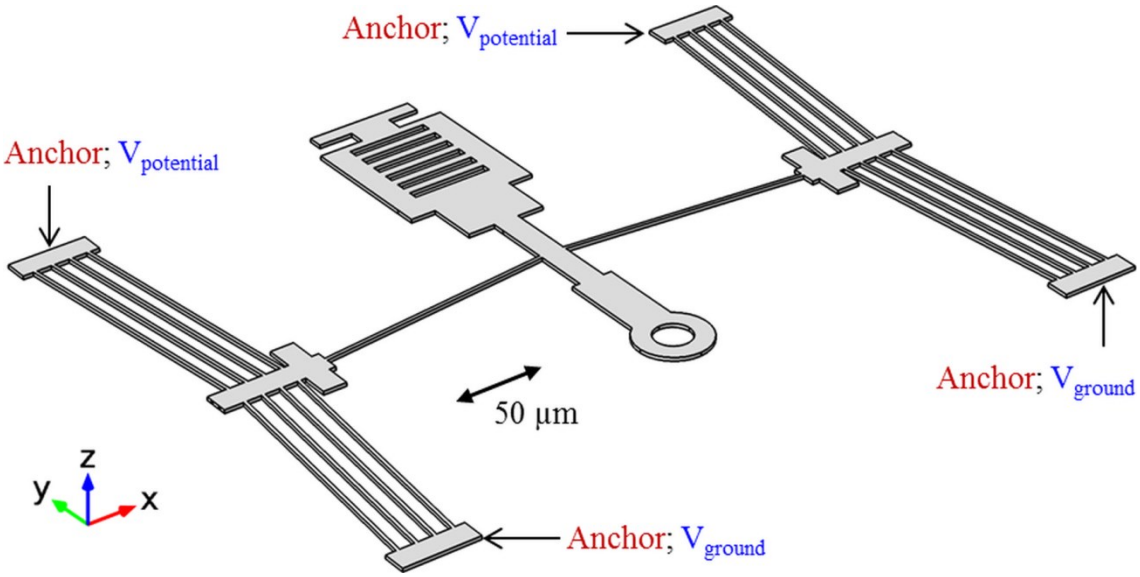

Figure 6.1: MEMS actuator geometry created on COMSOL™ for simulations.

A 3D tetrahedral mesh was created along the entire actuator volume (Figure 6.2). A predefined fine mesh with minimum element size of 4.26 μm and a total number of elements on the order of 30,000 was used. To investigate whether changing the mesh size would modify the FEA results, the simulations were re-run with a finer mesh (minimum element size 2x smaller). The results for the finer mesh were within 2%, of the original mesh results, indicating that the original results had converged and the initial mesh was sufficiently fine. Physical parameters such as temperature and displacement were calculated for each node of this mesh.

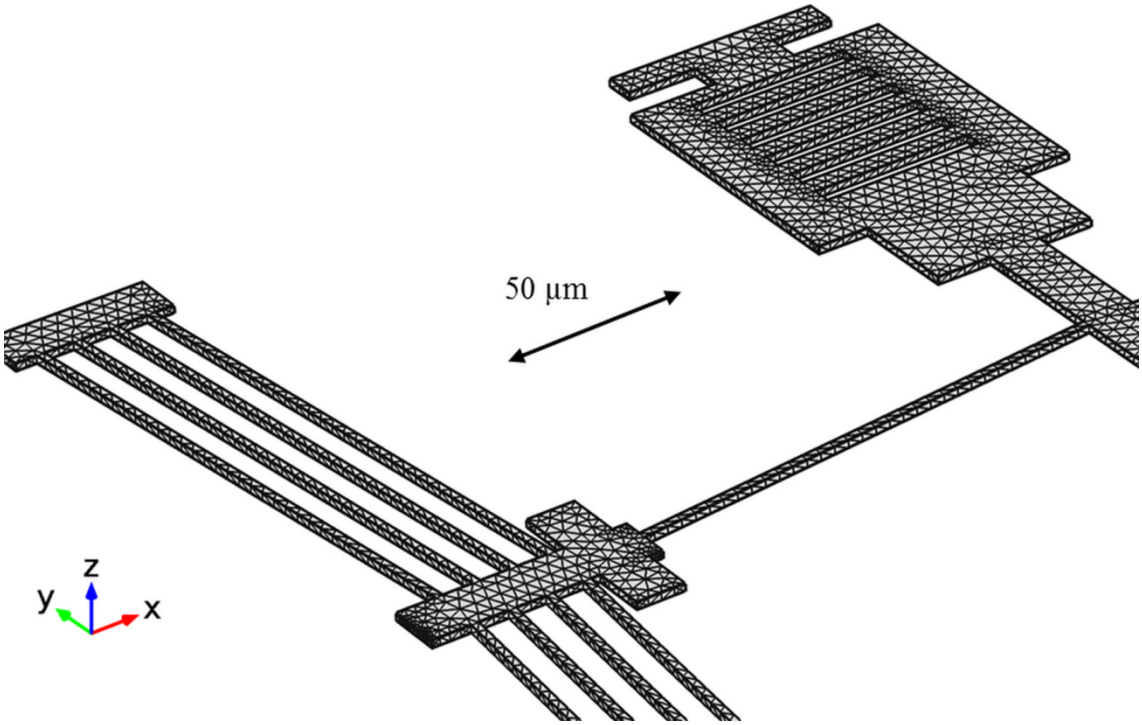

Figure 6.2: Tetrahedral mesh used at the MEMS actuator geometry for the FEA calculations.

The Joule heat physics was integrated with heat transfer physics in order to better model the boundary conditions of the system. Differential equations were used to calculate the temperature distribution along the squeezer actuator structure. The model used temperature dependent parameters (polysilicon: heat capacity, thermal expansion coefficient, thermal conductivity, and electrical conductivity; water: thermal conductivity) retrieved from [92], [93]. Other materials properties needed for the

simulations were provided by the COMSOL™ material database. Due to the small dimensions of the system (micro-scale), thermal conduction was considered the only mode of heat transfer; see below the heat flux equation used to estimate the heat flux between the polysilicon and the media:

$$q = \frac{k}{L}(T_{ext} - T) \tag{12}$$

where, q is the heat flux, k is the thermal conductivity of the media, L is the linear distance between the heat source and the boundary surface, T_{ext} is the external temperature and T is the surface temperature of at the actuator's beams. The actuator's side and bottom faces were selected to trade heat with the substrate, located 2 μm underneath (L = 2 μm). The top face of the actuator was selected to trade heat with the top imaginary boundary surface located 60 μm above (L = 60 μm). 60 μm is an arbitrary value as simulations showed that results were not significantly influenced by values of L greater than 30 μm for the top surface calculation. Finally, the boundary surfaces and all 4 chevron anchors were set to room temperature, T_{ext} = 20 °C.

6.2 Temperature at the Cell Test Location

The results showed that even for the maximum voltage used (12 V_{RMS}) there is a negligible temperature increase (< 0.01 °C) at the cell test location. This is due to the large distance between the cell test location and the heat generators (chevron arms). Therefore, the cells do not experience induced temperature changes during the tests. Figure 6.3 shows the temperature increase profile along the entire actuator surface at 6 V_{RMS}. The maximum temperature increase was ~25 °C and occurred at the center of the chevron arms.

Experimental confirmation of the simulated temperature of the MEMS device was not performed due to difficulties of doing so. Thermocouples could not be used due to their bigger dimensions (minimum of 50-100 μm). Raman spectroscopy might be used to

measure MEMS temperature, but calibrating the measurements is difficult without detailed knowledge of the material's optical properties. One indication that the temperature simulations were reliable (and by implication that the cell temperature rise is negligible) was the good agreement between the measured and the simulated motion of the MEMS device (section 8.2), as the displacement is proportional to the temperature rise.

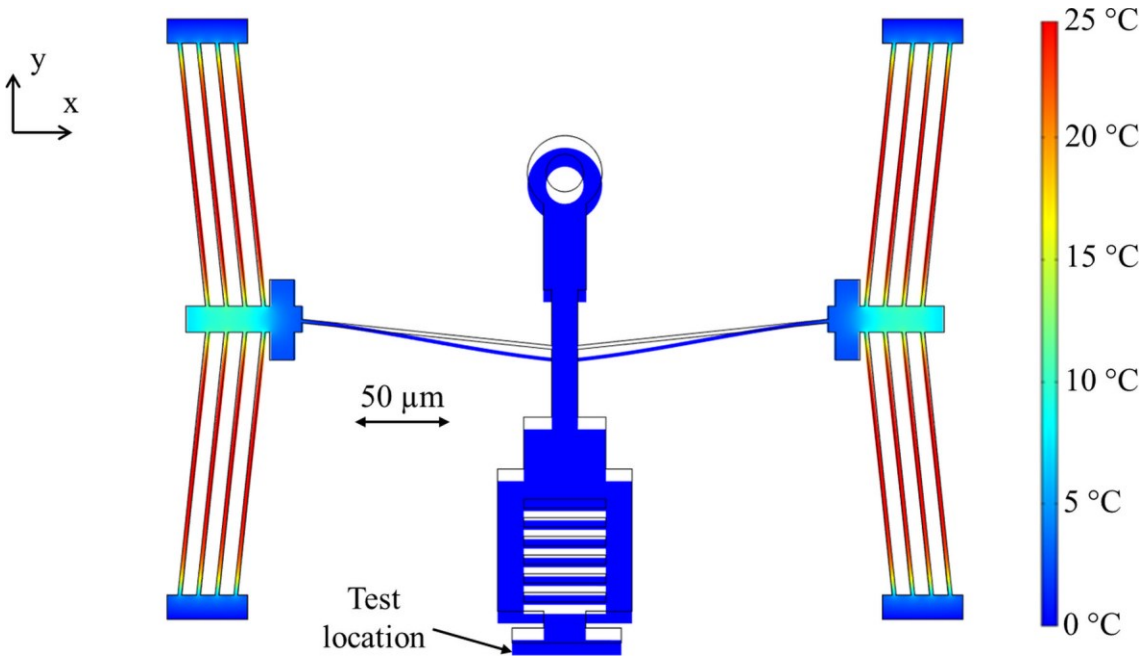

Figure 6.3: Simulated temperature distribution at 6 V_{RMS}. Colour indicates temperature increase (Max ΔT = ~25 °C). Simulated displacement exaggerated by 10x.

6.3 Maximum Temperature at the MEMS Actuator

The maximum temperature over the entire MEMS geometry occurred at the center of the chevron arm as could be seen in the previous sub-section. Figure 6.4 (a) shows the simulated temperature increase profile along one of the chevron arms. The maximum temperature increase is reached at a distance of ~30 µm from the anchor. It remained constant for ~70 µm and started to drop at ~30 µm from chevron shuttle. Different arms showed negligible changes at their temperature profile and maximum temperatures (< 1%). Figure 6.4 (b) shows the simulated maximum temperature increase at one of the

chevron arms vs. applied voltage. Note that the net temperature was proportional to voltage squared (parabolic fit of $R^2 > 0.9999$) as stated by equation (5). The maximum temperature rise at 12 V was 88.6 °C which results in an absolute temperature of 108.6 °C. This may explain the bubble formation when the applied voltage reached 11-12 V_{RMS} during the experiments. The bubbles could be caused by water boiling.

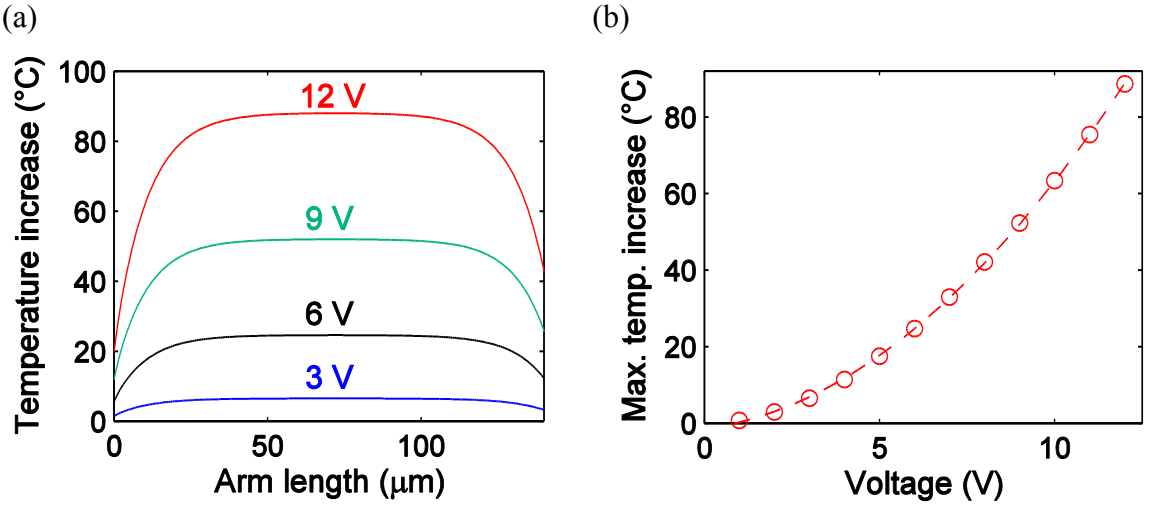

Figure 6.4: (a) Simulated temperature increase along the chevron arm at different voltages, 0 µm of arm length is at the anchor and 140 µm is at the shuttle. (b) Simulated maximum temperature increase at the chevron arm vs. applied voltage.

6.4 Actuator Simulated Performance

Simulations estimated the displacements of the chevron shuttle and of the jaw. Figure 6.5 shows their motion vs. the applied voltage which was incremented up to 12 V by fixed voltage steps of 1 V. Second degree polynomial functions were used to fit the data. Both curves confirmed the quadratic relation between displacement and voltage ($R^2 > 0.9999$). The displacements of the chevron and the jaw at 12 V_{RMS} were 0.29 and 2.7 µm respectively. The simulated motion amplification factor provided by the mechanical amplifier was 9.3.

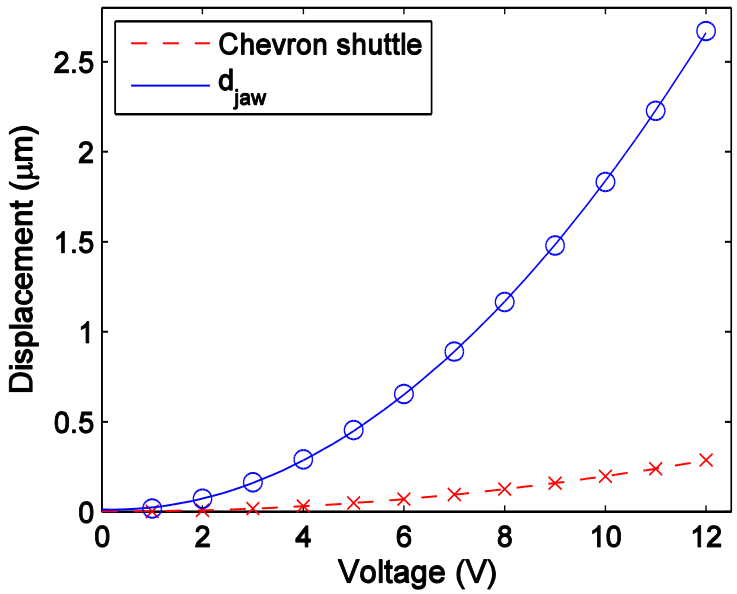

Figure 6.5: Simulated performance of MEMS device at 0 to 12 V_{RMS} range.

Figure 6.6 shows the simulated motion of the MEMS actuator at 12 V (with an exaggeration factor of 2x) in both the X direction (a) and in the Y direction (b). The design of the MEMS actuator does not allow the jaw to twist or move laterally when it is activated as shown in Figure 6.6 (a).

(a) X direction displacement:

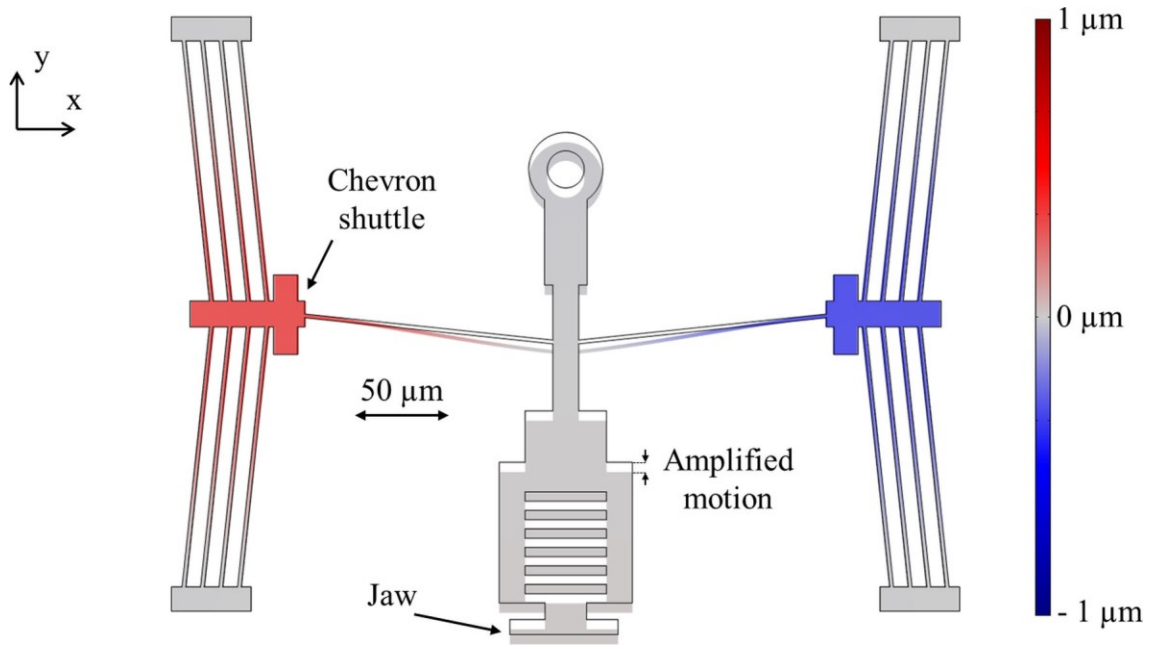

(b) Y direction displacement:

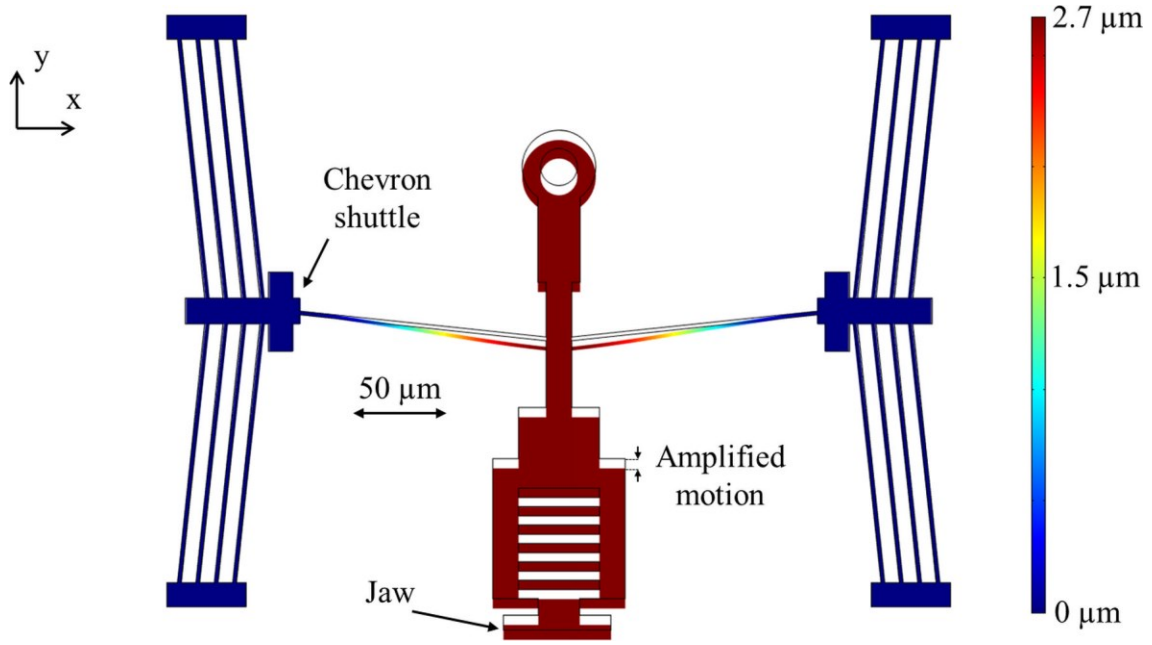

Figure 6.6: Simulated MEMS displacement at 12 V with an exaggeration factor of 2x. (a) Colour map shows X direction displacement. (b) Colour map shows Y direction displacement.

6.5 Back Spring Elastic Constant

FEA of the back springs was conducted in order to assess their elastic constant. 2D solid mechanics models of the springs were set up (Figure 6.7). After importing the spring design to COMSOL^{TM} the four anchors were set as fixed constrains and a free triangular mesh was created over the entire spring planar geometry (Figure 6.8). A predefined normal mesh with a minimum element size of 0.15 µm and a total number of elements on the order of 2,500 was used. To investigate whether changing the mesh size would modify the FEA results, the simulations were re-run with a finer mesh (minimum element size 2x smaller). The results for the finer mesh were within 1% of the original results, indicating that the original results had converged and the initial mesh was sufficiently fine. Polysilicon material properties were retrieved from COMSOL^{TM} database (density: 2320 kg/m^3, Young's Modulus: 160 GPa, Poisson's ratio: 0.22).

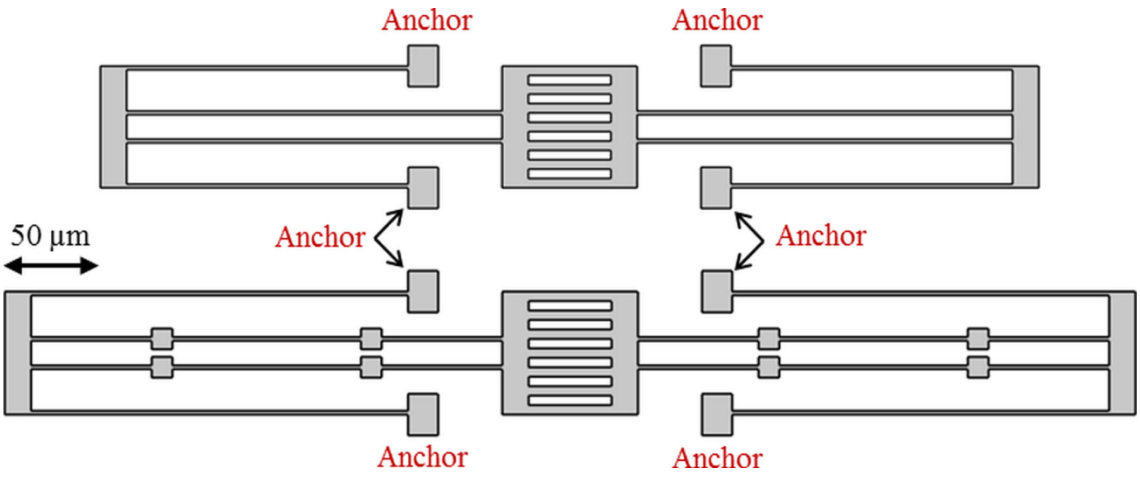

Figure 6.7: 2D solid mechanics model of the 2 back spring designs used in this study. Top back spring: L_1= 200 µm; bottom back spring: L_1= 250 µm.

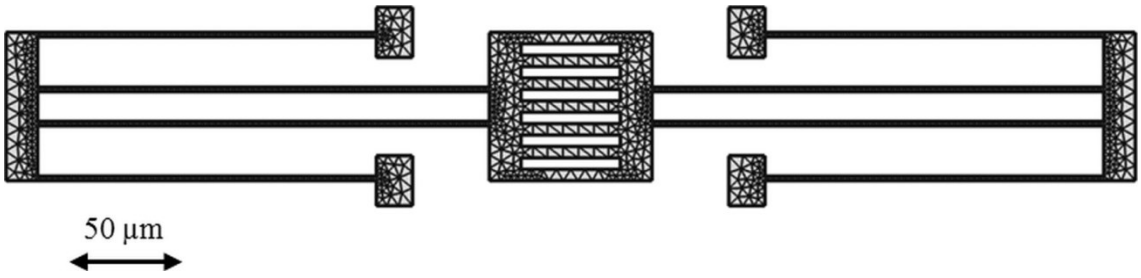

Figure 6.8: Free triangular mesh used at the back spring geometry for the FEA calculations.

The displacement of the accordion spring was simulated for a transversal force of 1 µN applied to the bottom of the comb box. The back spring stiffness (in the transversal direction) was calculated by taking the ratio of the applied force and the simulated displacement. The stiffness of the back springs designed with arm lengths of 200 and 250 µm (L_1) were 0.92 and 0.43 respectively. The difference between the FEA and calculated stiffness (section 4.6) was less than 3%. Figure 6.9 shows the transversal displacement of the accordion spring when it is pushed upwards with F = 1 µN.

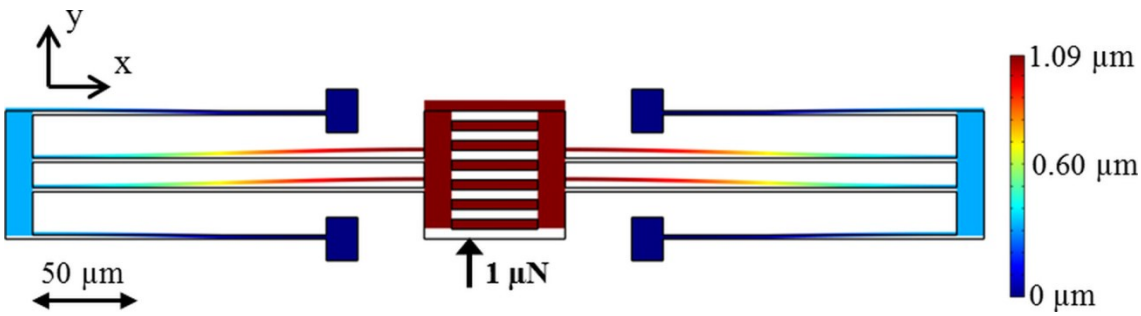

Figure 6.9: Simulated displacements of the back spring with an exageration factor of 2x. Colour map and legend shows transverse (y) motion.

The selective compliance of the accordion spring reduced its longitudinal (x direction) displacement to negligible values. Figure 6.10 shows the spring longitudinal displacement when the force is applied to the comb box extremity. Note that the maximum displacement is on the order of 0.002 µm. Therefore, since the forces used in this study are on the range of 0 to 1.5 µN, the rotation or twist of the back spring was considered negligible.

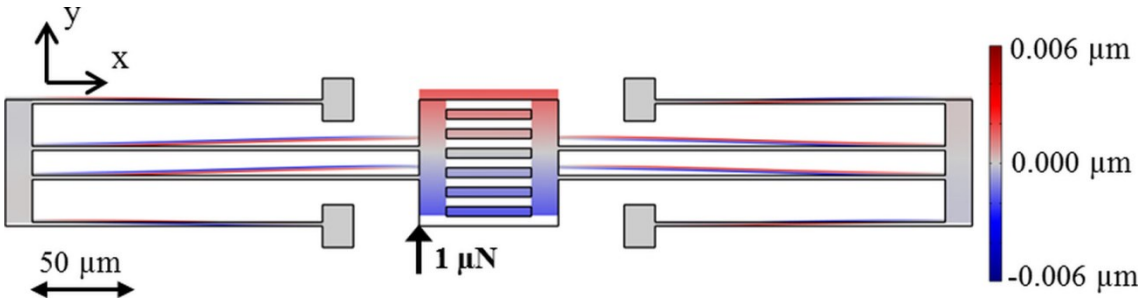

Figure 6.10: Simulated displacement of the back spring with an exageration factor of 2x. Colour map and legend shows longitudinal (x) motion.

Chapter 7: Cell Mechanical Model

7.1 Cell Squeezing Model Set up

The compression of single yeast cells by the MEMS device was simulated. The influence of the cell's Young's modulus and geometry on the cell stiffness was considered. Note that in order to simulate the cell stiffness, the cell Young's Modulus must be known or assumed. Using modulus values obtained from previous studies, the following Finite Element Analyses were conducted. Firstly, using AFM reported modulus value; cell stiffness was estimated by simulating cell deformation for different compression forces. Then, the effect of varying the Young's modulus on cell stiffness was assessed by repeating the procedure to estimate cell stiffness for different values of cell modulus. Finally, for a fixed value of Young's modulus (AFM), cells stiffness was calculated for different combinations of the cell geometric characteristics: diameter, shape, position, and contact area.

A 3D model built in COMSOL™ was used to simulate the cell compression test described on the previous sections. The cell was represented by a microscopic solid elastic sphere or ellipsoid with homogeneous properties. The back spring (Poly 1) planar dimensions were imported from L-Edit™ and extruded in Z by 2 μm. The cell was placed in contact with the back spring and an external force was applied to push the cell against the back spring as shown in Figure 7.1. A 3D tetrahedral mesh with a minimum element size of 0.75 μm was used over the entire system (cell plus back spring). The total number of elements over the entire geometry was on the order 50,000. The number of elements considering only the cell was on the on the order of 3,000 (for a 6 μm diameter spherical cell). Figure 7.2 shows the mesh used to discretize the cell.

(a)

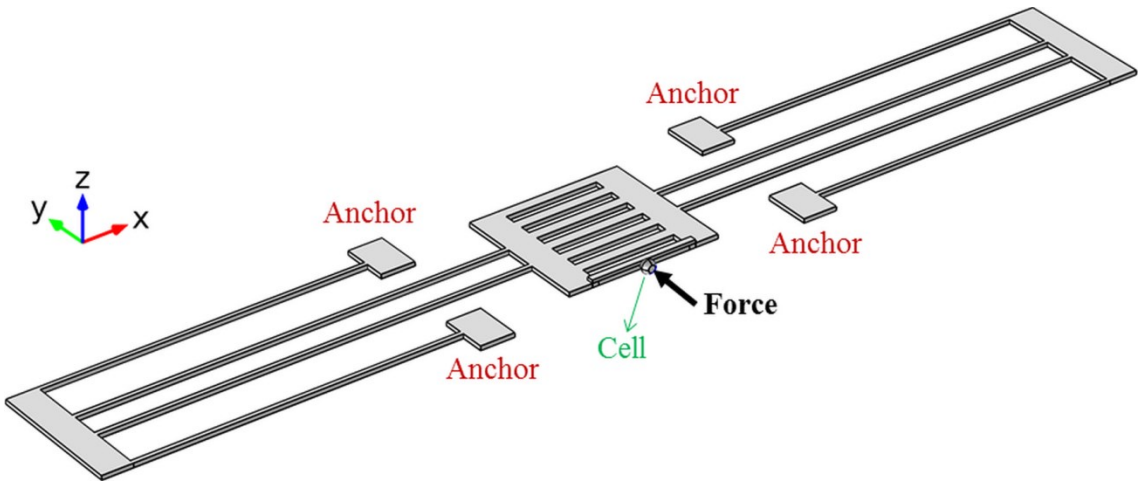

(b)

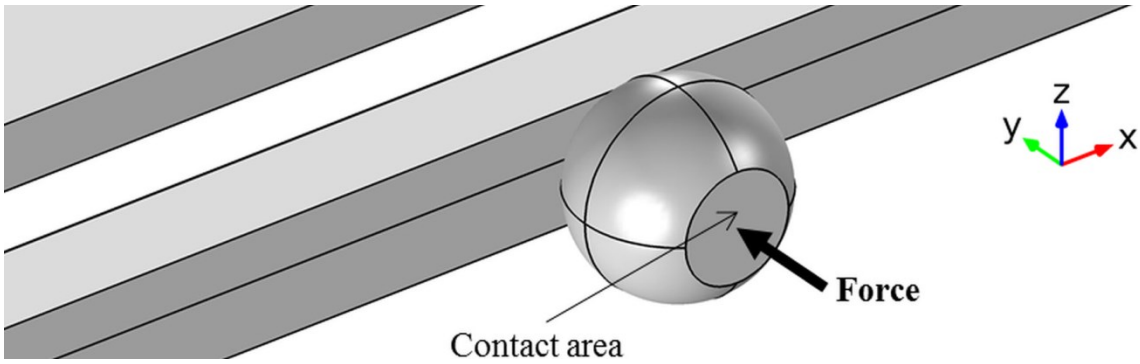

Figure 7.1: (a) Cell squeezing model built in COMSOL™. (b) Zoom in at cell location.

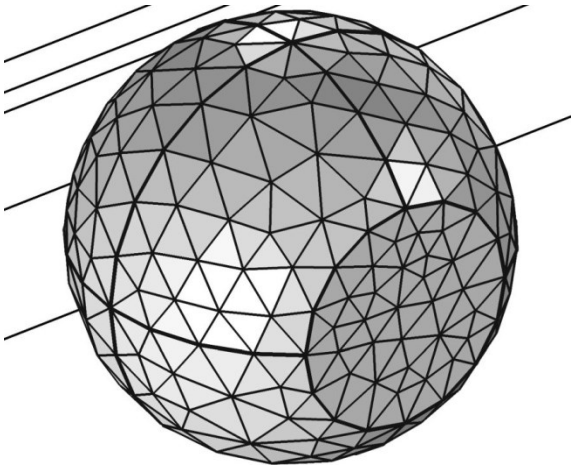

Figure 7.2: Mesh used to discretize the entire volume of the cell model.

7.2 Calculation of Cell Stiffness from Simulations

In order to numerically estimate cell stiffness, the displacements of the front surface of the cell where the force was applied (d_{jaw}), and of the back surface of the cell in contact with back spring (d_{spring}) were simulated. The force was increased from 0 to 1 µN by a fixed step of 0.05 µN and the cell deformation (d_{jaw} - d_{spring}) calculated for each applied force. The ratio of force and deformation indicated the cell stiffness. Figure 7.3 shows the force vs. deformation graph of a spherical cell of: 6 µm of diameter, contact circular diameter of 3.3 µm (contact area is discussed later), density = 1,100 kg/m^3 [94], Poisson's ratio = 0.49 [78], and Young's Modulus = 1 MPa [46], [83], [95]. Polysilicon properties were retrieved from COMSOL^{TM} as in section 6.5. For this configuration, the cell elastic constant (slope of the linear fit) was 3.0 N/m. Figure 7.4 shows the colour map of the simulated total displacement (y direction displacement) of the cell and the back spring at 0.5 µN. Note the simulated displacements of the jaw (d_{jaw}) and of the back spring (d_{spring}) in zoomed in image. Figure 7.5 highlights the cell displacement (for F = 0.5 µN) with a colour map restricted to the cell displacement range (0.57 to 0.75 µm).

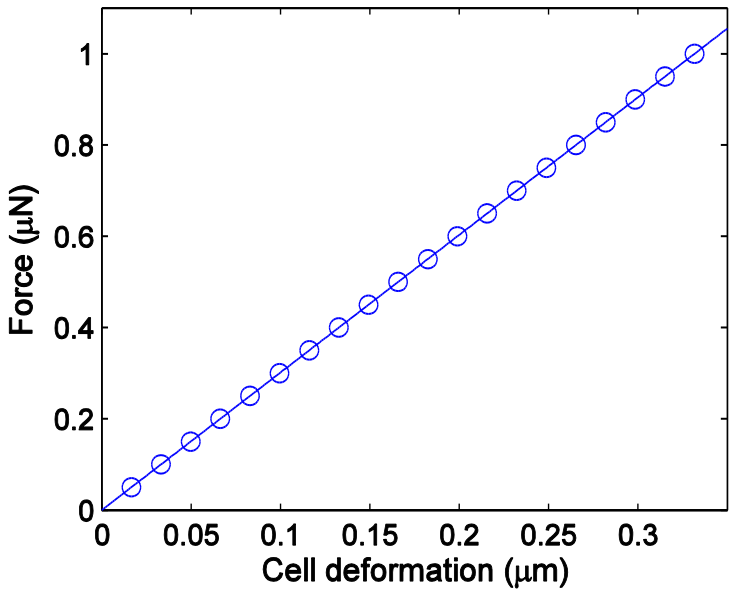

Figure 7.3: Simulated force vs. deformation for a spherical cell of 6 µm of diameter. Slope is the cell elastic constant.

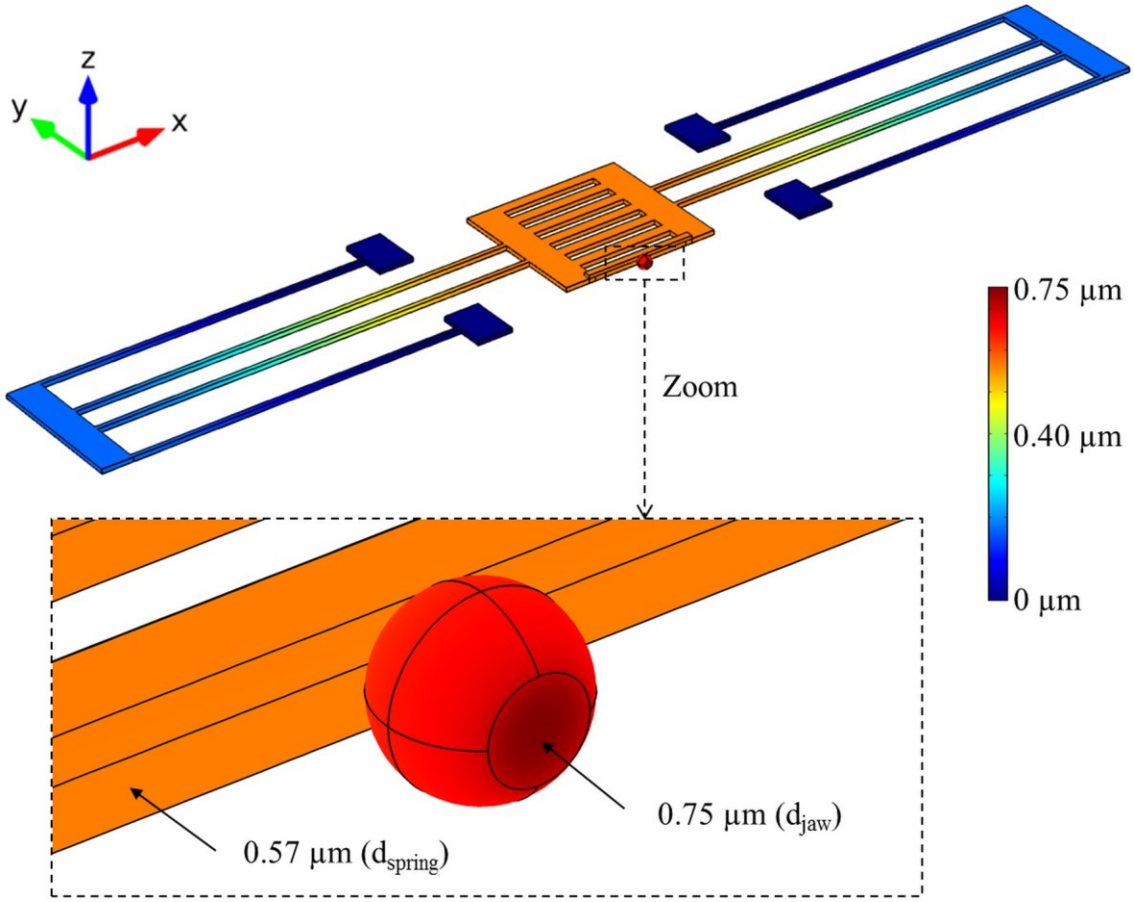

Figure 7.4: Colour map of the simulated displacement for 0.5 µN over the entire system, and zoomed in at the cell location.

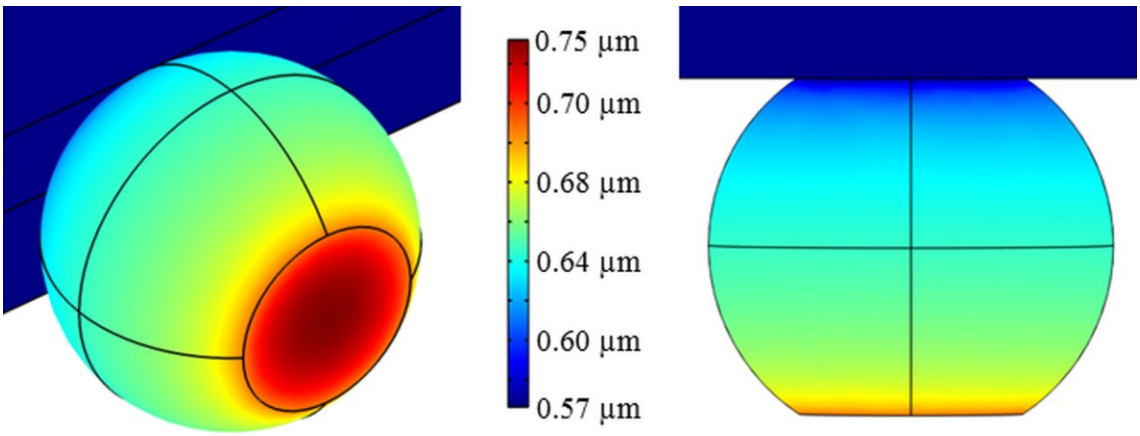

Figure 7.5: Spherical cell displacement colour map for an applied force of 0.5 µN. LEFT: isometric view. RIGHT: top view.

7.3 Cell Stiffness and Young's Modulus

The relation between the cell stiffness and its Young's modulus was simulated. The cell stiffness was calculated (as above) for different values of Young's modulus while keeping all the other parameters fixed (same as in section 7.2). Simulations showed that the stiffness is directly proportional to the Young's Modulus as can be seen in Figure 7.6. The proportionality constant (slope of the linear fit) is 2.93 ± 0.01.

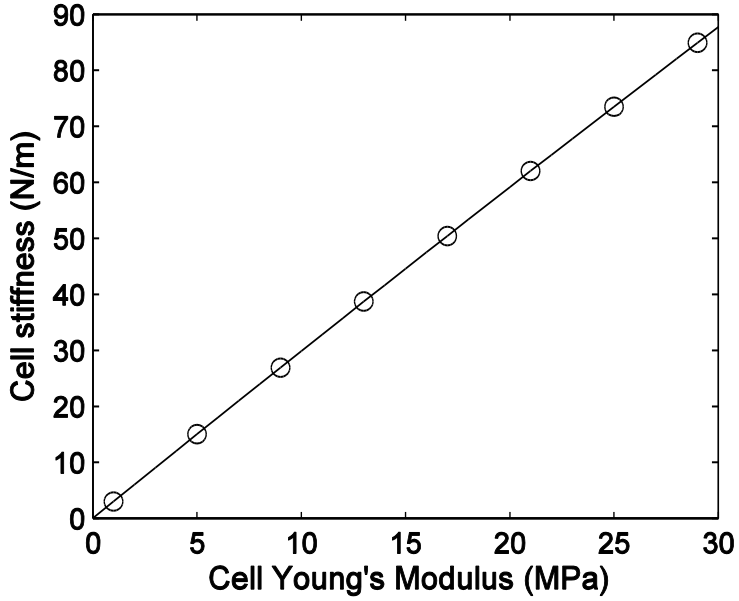

Figure 7.6: Simulated cell stiffness vs. cell Young's modulus for the same parameters used at the section 7.2.

7.4 Cell Stiffness and Geometrical Parameters

The influence of cell size and shape on the cell stiffness was analyzed. The top view (under the microscope) of the great majority of the cells tested could be roughly described as ellipses with major and minor diameters in the 5 to 8 μm range. Figure 7.7 (a) illustrates the top view of a cell with main diameters D_1 and D_2 under compression. The third diameter D_3 (into the page) can be seen in Figure 7.7 (b) that shows the isometric view of the cell. D_3, which could not be measured from the in-plane images provided by the microscope, was varied in the same range of D_1 and D_2, from 5 to 8 μm.

(a) Top view (b) Isometric view

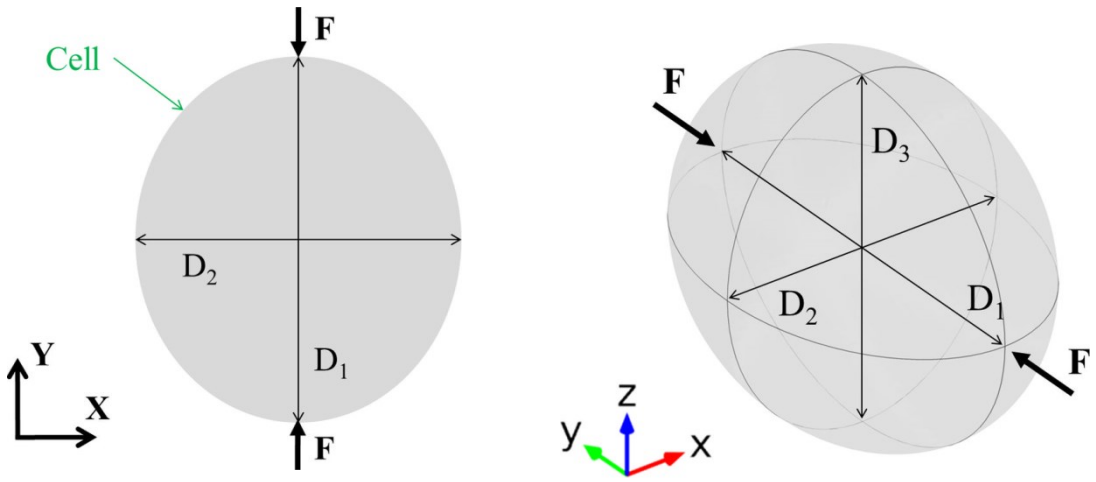

Figure 7.7: Schematic of a generic cell (main dimeters: D_1 and D_2) during compression.

Firstly, the influence of size on cell stiffness was analyzed. Considering the cells as spheres ($D_1 = D_2 = D_3$), FEA was used to calculate their stiffness for diameters ranging from 5 to 8 µm. All other parameters were the same of section 7.2. Simulations indicated that spherical cell stiffness drops as its diameter increases. The maximum diameter increase (from 5 to 8 µm) caused a stiffness drop of approximately 24% (from 3.5 to 2.7 N/m). Figure 7.8 shows the simulated cell stiffness for different cell diameters, the fit is a power regression ($y = ax^b$) with $R^2 = 0.9725$.

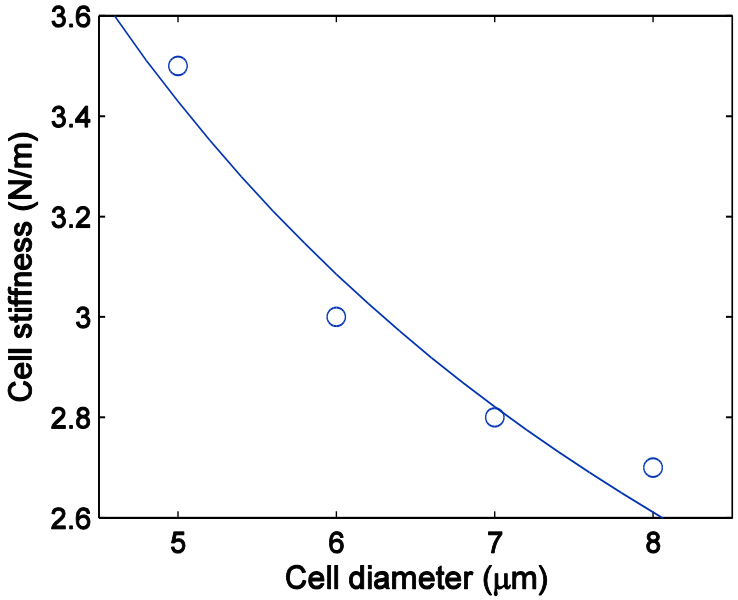

Figure 7.8: Simulated spherical cell stiffness vs. cell diameter.

FEA was also used to estimate the relation between cell stiffness and its shape by comparing the stiffness of ellipses and spheres with the same average diameter 6 μm (approximately the same volume). D_1 and D_2 were varied in the 5-7 μm range while D_3 was fixed to 6 μm. All other parameters were the same as in section 7.2 and the same procedure to calculate cell stiffness was used. Table 7.1 shows the 5 different combinations of diameters simulated and the calculated stiffness at each case.

Table 7.1: Simulated cell stiffness (k_{cell}) for different combinations of the cell diameters.

D_1 (μm)	D_2 (μm)	D_3 (μm)	$D_{ave.}$ (μm)	D_2/D_1	k_{cell} (N/m)
7.0	5.0	6.0	6.0	0.7	2.7
6.5	5.5	6.0	6.0	0.8	2.8
6.0	6.0	6.0	6.0	1.0	3.0
5.5	6.5	6.0	6.0	1.2	3.2
5.0	7.0	6.0	6.0	1.4	3.4

Cell stiffness increased as D_2 / D_1 increased. When D_2 / D_1 increased by a factor of 2 the cell stiffness increased by 22%. It is worth noting that some cells in Table 7.1 could be observed as the same cells but rotated in plane by 90°. This indicates that cells with the same shape can have different stiffness depending on their orientation (rotation angle)

during compression. These results indicate that the shorter the distance between the two compressing plates the higher the cell stiffness, the same as observed for the cell diameter. Figure 7.9 shows the cell stiffness vs the ratio of its main diameters D_2/D_1. A linear regression of $R^2 = 0.9964$ was used to fit the data.

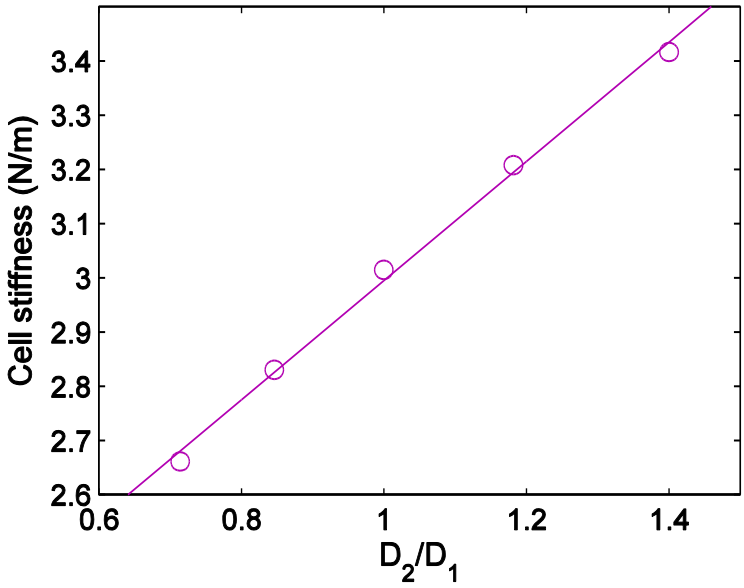

Figure 7.9: Simulated elliptical cell stiffness vs. cell diameters ratio (D_2/D_1).

Finally, the influence of the contact areas on cell stiffness was investigated via FEA. The contact areas are the surfaces of the cell in contact with the jaw and with the back spring. In order to simplify the analysis a spherical cell was modeled and both contact areas (jaw and back) were considered the same. Note that during actual cell experiments this parameter could change due to differences in the cell height when it is positioned at the test location. The cell height is difficult to control since only the top view of the cell testing is provided by the microscope. Different cell orientations could also result in slight changes in the contact area due to the non-flat shape of the jaw and the small size of its step length as commented in section 4.5.

The contact area can be approximated to a circular surface characterized by a contact diameter. Cell stiffness was simulated for different contact diameters ranging from 1.5 to 3.8 µm keeping all the other parameters fixed and the same as in section 7.1. However,

since the height of the squeezing plates is 3.5 µm contact diameters larger than that would not be possible. Results indicated that cell stiffness is proportional to the contact diameter (Figure 7.10). When comparing the compression of cells with the lowest (1.5 µm) and the highest contact diameters (3.3 µm) the change of cell stiffness was ~46% Figure 7.10 shows cell stiffness vs contact diameter. The linear fit over the points excluding the diameter larger than 3.5 µm showed a correlation coefficient of R^2 = 0.9998.

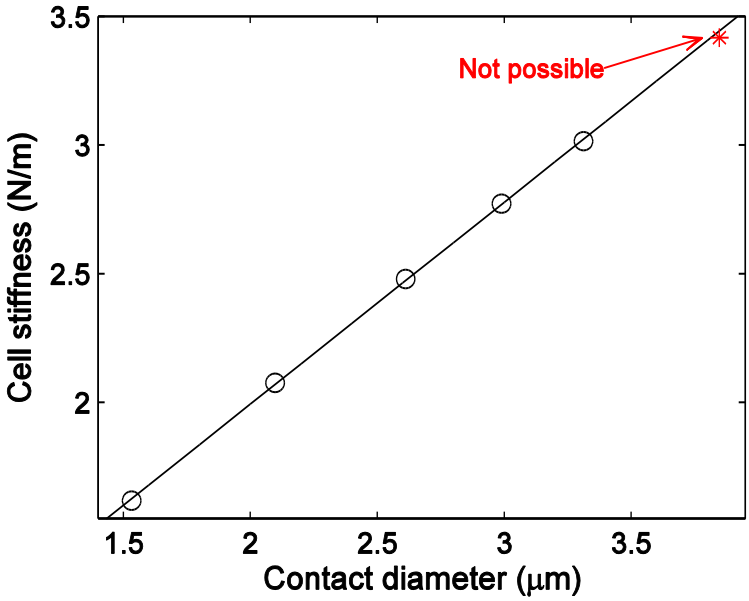

Figure 7.10: Simulated cell stiffness vs. contact diameter.

Chapter 8: MEMS Characterization

8.1 Chevron and Jaw Measured Displacements

In order to characterize the actuator performance (chevron and jaw motions), data was acquired with no cell placed at the testing location. After rinsing the chip with DI water, it was directly flooded with filtered tap water and mounted over the microscope stage. To activate the actuators, AC voltages were used in order to avoid water electrolysis as explained in previous sections. The input voltage (AC, 1 MHz sinewave) was increased up to 12 V_{RMS} by ~10 fixed voltage steps. Then, the voltage was reduced back to zero by the same number of steps to check for backlash.

Figure 8.1 shows the measured displacement of the chevron shuttle vs the applied voltage (0 to 12 V_{RMS}). Each point is the average of three trials with the error bars showing the standard deviation. The data showed a repeatability of ± 5-6 nm and a parabolic fit of R^2 > 0.995. The quadratic relation between displacement and voltage was expected since displacement is proportional to electrical power or voltage squared (see section 2.6). For the maximum input voltage (12 V_{RMS}) the chevron total displacement was 0.346 ± 0.005 μm when attached to a single arm amplifier. The chevron attached to a double arm amplifier showed a total displacement of 0.299 ± 0.004 μm at 12 V_{RMS}. The total displacement difference was of approximately 50 nm.

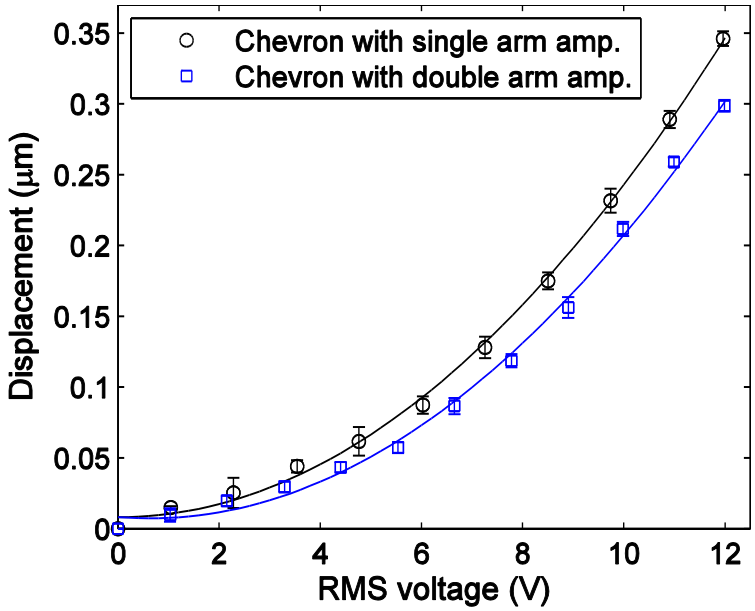

Figure 8.1: Measured chevron electrothermal actuator performance underwater (average of 3 trials). Parabolic relation with voltage as predicted.

Figure 8.2 shows the measured displacement of the jaw vs. the applied voltage. The points on the graph are the average of 3 trials with error bars showing the standard deviation. Measurements showed a repeatability of ± 5 nm and parabolic curves of $R^2 >$ 0.996 were used to fit the data. The jaw attached the single arm amplifier showed a final displacement of 2.433 ± 0.005 µm while the jaw attached to the double arm amplifier moved in total 2.373 ± 0.005 µm. Thus, the jaw with the stiffer amplifier moved about 60 nm less than the jaw attached to the less stiff amplifier.

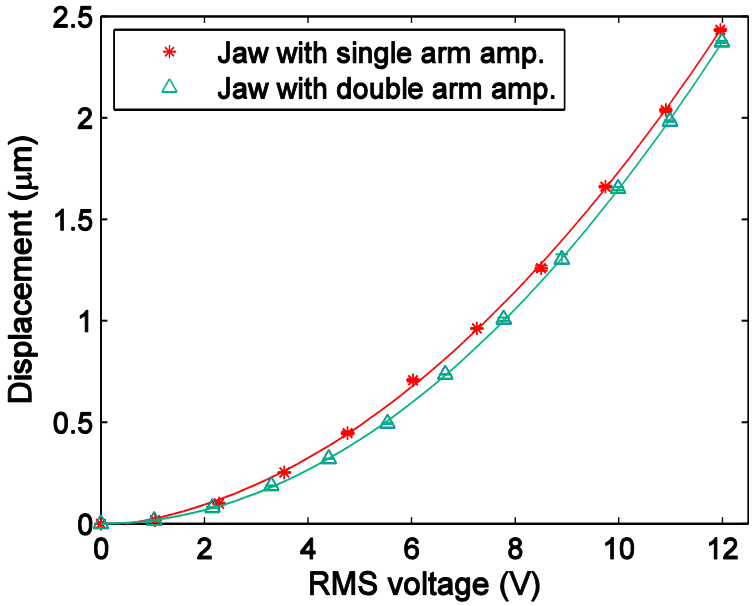

Figure 8.2: Measured jaw displacement in the 0-12 V_{RMS} range. Average of 3 trials, error bars are standard deviations.

In order to estimate the motion amplification provided by the mechanical amplifier the measured displacements of the chevron and the jaw vs. the square of the applied voltage was plotted in the same graph (Figure 8.3). The data was fit with linear functions of $R^2 > 0.995$. The motion amplification was calculated by taking the ratio of the slopes of the linear fits (slope $_{jaw}$ / slope $_{chevron}$). The amplification factors calculated for the single and double arm amplifiers were 7.4 and 7.9 respectively. The simulated amplification factor for the single arm amplifier was 9.3 (see section 6.4), a difference of 20%.

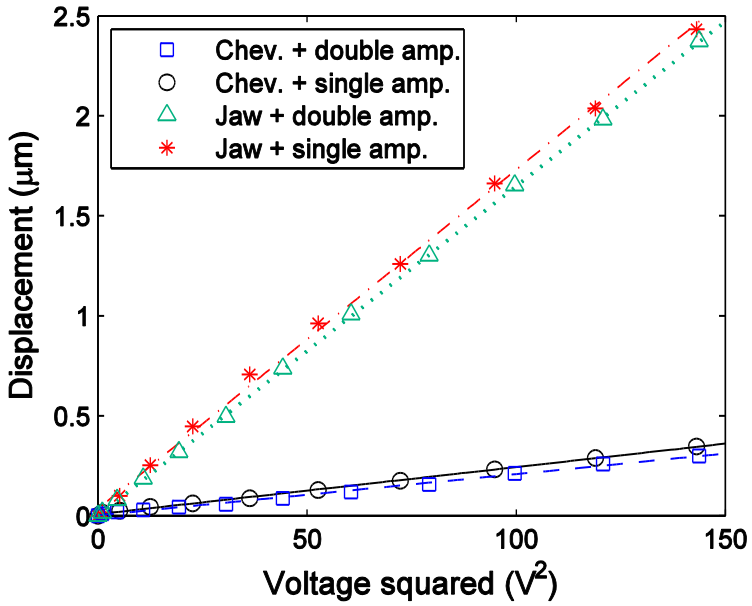

Figure 8.3: Measured chevron and jaw displacements vs. voltage squared and linear fits. Points are the average of 3 trials.

8.2 Simulated and Measured Performances

The measured MEMS performance was compared with the simulation results derived from the squeezer designed with a single arm amplifier (section 6). Figure 8.4 shows both the simulated and measured actuator's (chevron and jaw) displacements vs. applied voltage squared. The difference between the simulated and measured motions was ~13% for the chevron and ~8% for the jaw.

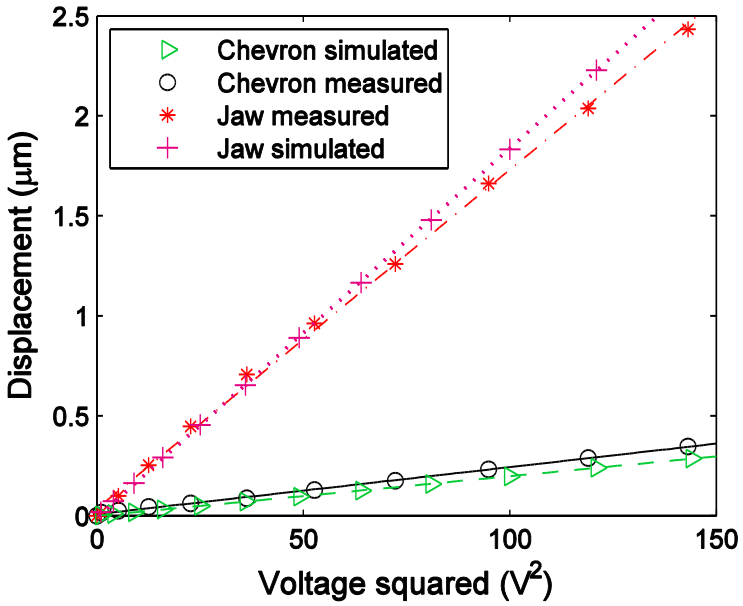

Figure 8.4: MEMS actuator's simulated and measured displacements in the 0-12 V_{RMS} range. Measured points are the average of 3 trials.

8.3 Measured Actuator Hysteresis

In order to measure the chevron backlash (hysteresis) its backwards motion was measured by reducing the voltage back to 0 V. Figure 8.5 shows the measured forward and backwards displacements of the chevron in the 0-12 V range. Each point in the graph is an average of 3 trials. A slight hysterectic behaviour was noticed; the maximum difference occured at the second highest applied voltage (11 V_{RMS}) when the displacement difference reached 44 nm (~13%).

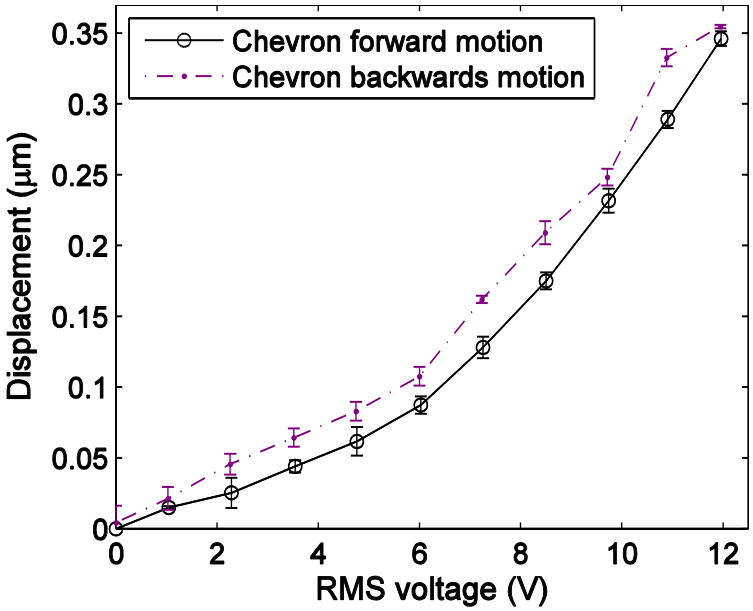

Figure 8.5: Measured hysteresis curve of the chevron attached to a single arm amplifier.

The backlash of the jaw connected to the single arm amplifier was measured in the 0-12 V range (Figure 8.6). As it occurred with the chevron the largest backlash error happened at ~11 V_{RMS}; the displacement difference at this voltage was about 250 nm (11%). The average backlash error was approximately 56 nm.

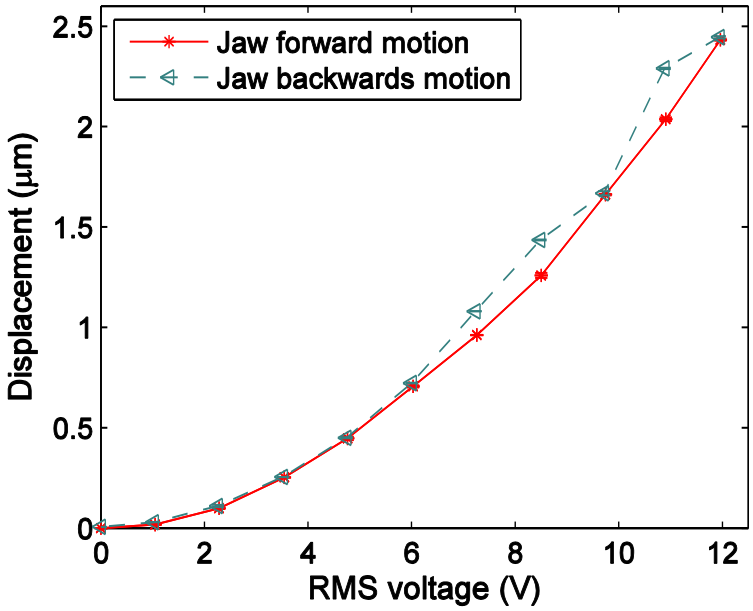

Figure 8.6: Measured hysteresis curve of the jaw attached to a single arm amplifier.

Chapter 9: Baker's Yeast Cell Measurements

9.1 Cell Stiffness in Low Force Tests

Baker's yeast cells had their stiffness measured in tests with no rupture. Cells were individually placed at the jaw and squeezed 3 times in succession. The voltage was incremented from 0 to 6 V_{RMS} with a voltage step of 0.6 V_{RMS} (10 steps).

Figure 9.1 (a) shows a cell during the low force compression test while Figure 9.1 (b) shows the force (k_{spring}*d_{spring}) vs. deformation (d_{jaw} - d_{spring}) data of this particular cell test. Each point in the graph is the average of the 3 trials/cycles and error bars are the standard deviations. The cell showed a linear force response; a linear fit of $R^2 = 0.9945$ was used to fit the data. The force was increased from zero (no cell deformation) to ~0.27 μN when cell deformation reached ~55 nm. The cell stiffness was calculated by taking the slope of the linear fit which was 5.4 ± 0.1 N/m.

In total, 7 different yeast cells were tested under the conditions described above. The measured cell stiffness ranged from 3.5 to 6.8 N/m with an average of 4.7 ± 1.2 N/m. Table 9.1 shows the experimental results for each of the tested cells. The measurements were smaller than but comparable to values reported by [80] who measured an average cell stiffness of ~11 N/m performing the microplate compression of single yeast cells (*Saccharomyces cerevisiae*).

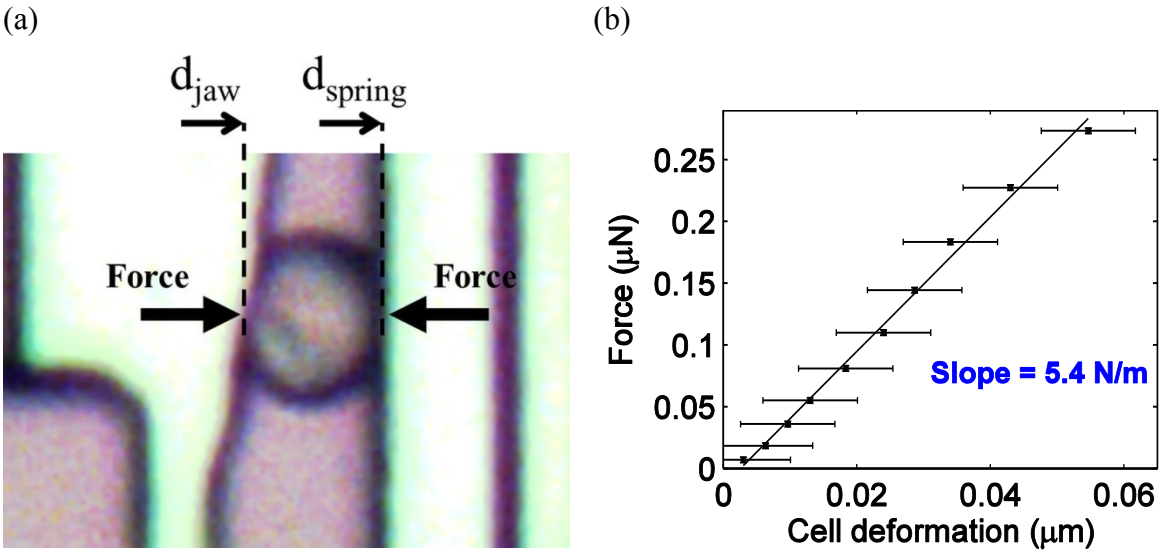

Figure 9.1: (a) Microphotograph of a cell during low force test (test # 2 in Table 9.1). (b) Force vs deformation (d_{jaw} - d_{spring}) data, slope is cell stiffness.

Note that repeated manipulation of the cells can affect their mechanical properties. However over the short test sample (n = 3 trials), no drift was observed. The individual 1st, 2nd and 3rd trials typically varied 2-7% from the average of the 3 trials. The average slope of the stiffness change vs. trial number was below 1%, indicating no net trend or drift to the 3 trials.

The effect of cell size on stiffness was investigated: cell size was estimated by fitting an ellipse (error of ± 0.2 μm) to the cell contour. Major diameters ranged from 6.5 to 7.6 μm (average = 7.0 ± 0.4 μm); minor diameters ranged from 5.0 to 5.7 μm (average = 5.3 ± 0.3 μm). Over this range of cell sizes, no correlation was found between stiffness and cell diameters, area or aspect ratio. Table 9.1 shows the main diameters of the cells.

Table 9.1: Cells low force tests results.

Test (#)	Minor diameter (µm)	Major diameter (µm)	Max force (µN)	Max def. $d_{jaw} - d_{spring}$ (µm)	Stiffness (N/m)
1	5.3	7.6	0.26	0.083	3.4 ± 0.4
2	5.3	7.2	0.27	0.055	5.4 ± 0.1
3	5.7	6.5	0.27	0.065	4.9 ± 0.2
4	5.5	6.6	0.27	0.055	6.8 ± 0.6
5	5.0	7.1	0.27	0.073	5.0 ± 0.3
6	5.0	7.0	0.26	0.092	3.6 ± 0.2
7	5.0	6.8	0.26	0.084	3.5 ± 0.1
Avg.	5.3 ± 0.3	7.0 ± 0.4	0.27	0.072 ± 0.015	4.7 ± 1.2

9.2 Effect of Cell Position offset on Measured Stiffness

During cell placement, the cell may be positioned at different squeezing gaps (section 4.5) and this may affect the stiffness measurement. In order to quantify this effect the same cell was tested in two different positions, one of them closer to the jaw centerline than the other. Figure 9.2 shows the microphotographs of the same cell located (a) ~0.3 µm and (b) ~4.8 µm from the jaw centerline: the measured stiffness were 7.7 ± 0.9 N/m and 6.9 ± 0.8 N/m respectively. In total, 6 cells were tested at two different locations and each of them showed similar results as can be seen in Table 9.2. Increasing the cell offset from the jaw centerline always resulted in a measured stiffness drop. The maximum stiffness drop observed was 15% for a 5 µm offset increase. On average each additional 1 µm of centerline offset decreased the measured stiffness by ~2.5%.

(a) Position 1:

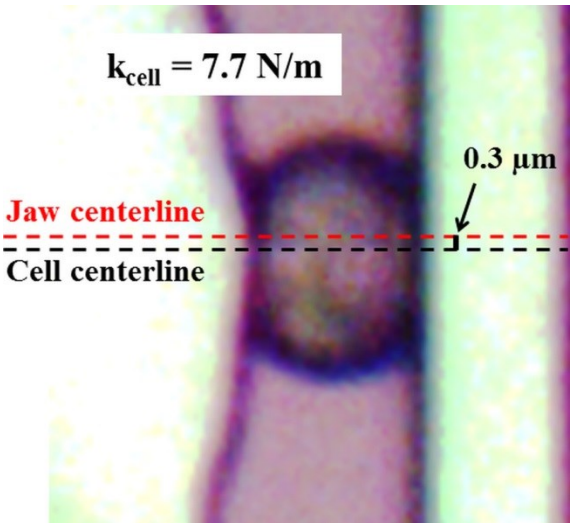

(b) Position 2:

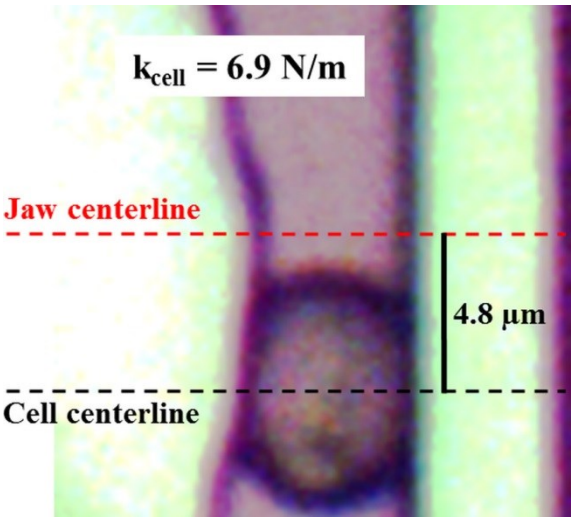

Figure 9.2: Same cell (test # 12 in Table 9.2) placed and tested in two different positions: (a) cell 0.3 µm from the jaw centerline and (b) cell 4.8 µm from the jaw centerline.

Table 9.2: Measured stiffness of cells tested in different positions.

Test (#)	Position (#)	Distance to center (µm)	Stiffness (N/m)	Stiffness drop (%)	Stiffness drop per µm (%)
8	1	5.1	4.7	15.4	3.2
	2	9.9	4.0		
9	1	0.6	5.1	1.8	0.5
	2	4.4	5.0		
10	1	1.9	4.4	13.3	5.2
	2	4.5	3.8		
11	1	1.9	2.5	4.0	1.1
	2	5.7	2.4		
12	1	0.3	7.7	9.9	2.2
	2	4.8	6.9		
13	1	0.2	5.9	5.3	1.7
	2	3.3	5.6		
Avg.	-	-	-	8.3	2.3

This observed drop in measure stiffness is likely due to rotational compliance of the actuator suspension. The amplifier and back spring suspensions (B and D respectively in Figure 4.3 and Figure 4.4) are stiff with respect to rotation, but not infinitely so. The offset cell applies a torque to the squeezer which slightly rotates it, and the ideally axial

squeezing force now includes a small shear component. COMSOL^{TM} simulations of the actuator suspension showed that an offset force tends to increase d_{jaw} but not d_{spring} since the back suspension has higher rotational stiffness compared to the amplifier. This leads to a measured stiffness slightly lower than if the cell was perfectly centered. This effect is small (a few percent) compared to the measurement uncertainty and could be counteracted in designs with stiffer amplifiers.

9.3 Cell Rupture Force and Stiffness Change

To measure cell rupture force and stiffness change yeast cells were squeezed only one time up to the maximum 12 V_{RMS} with a voltage step of 1.2 V_{RMS} (10 steps). Figure 9.3 shows a sequence of three microphotographs of one such test. Note the dark crack that appeared on the cell surface at Figure 9.3 (b). The crack indicated that the cell rupture force was reached.

(a) F = 0 (b) F = $F_{rupture}$ (c) F = F_{max}

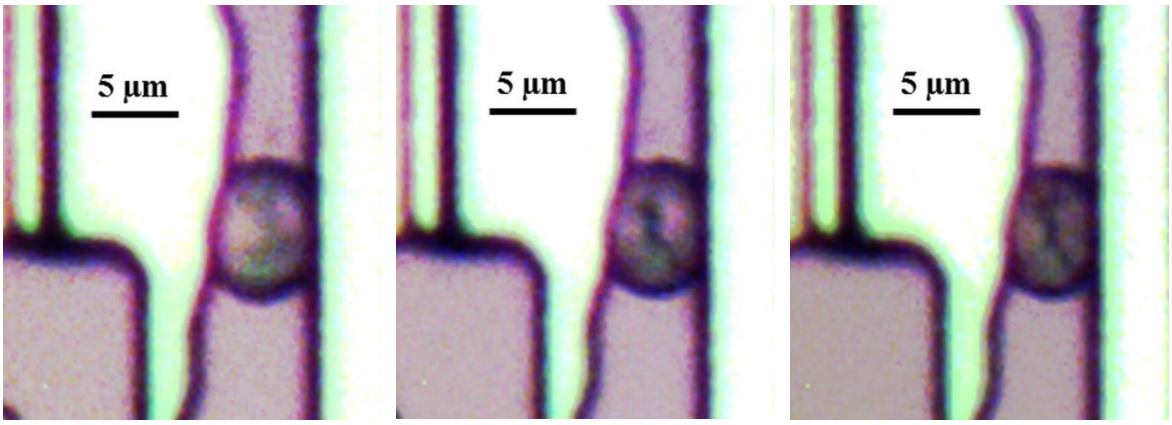

Figure 9.3: Yeast cell (test # 17 in Table 9.3) during a rupture squeezing test: (a) at the beginning of the test (F = 0), (b) when rupture occurs (F = $F_{rupture}$), and (c) at maximum compression (F = F_{max}).

Figure 9.4 shows the force vs. deformation data of one the tests that led to cell rupture. As only a single trial was conducted on these tests, the deformation error bar are derived from the MEMS displacements uncertainties (section 8.1) and the force error bars indicate the back spring displacement uncertainty multiplied by the back spring stiffness.

The maximum force in this case was 0.65 µN and rupture occurred at ~0.4 µN with a ~110 nm discontinuity in the deformation axis. Note the cell linear force response before and after rupture (linear fits of $R^2 > 0.997$). The measured slopes of the linear fits (cell stiffness) were 7.5 ± 0.7 N/m before rupture and 0.28 ± 0.04 N/m after rupture, a drop of 95%. In this particular test the cell was pushed against the softer back spring (k_{spring} = 0.43 N/m).

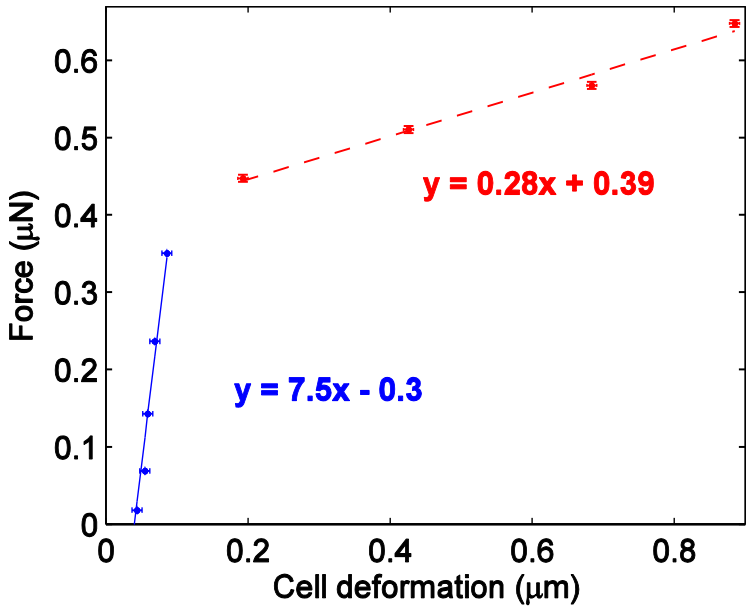

Figure 9.4: Force vs deformation (d_{jaw} - d_{spring}) data of a cell (test # 22 in Table 9.3) that ruptured during compression. The slope of the linear fits changed dramatically after rupture. Back spring elastic constant equals to 0.43 N/m.

Figure 9.5 shows the force vs. deformation of another cell tested beyond its rupture. This cell was compressed against the stiffer back spring (k_{spring} = 0.92 N/m) which led to a higher maximum force of ~1.21µN. The cell rupture occurred at ~0.45 µN where there is a ~180 nm discontinuity in the deformation. The measured slope was 5.5 ± 0.1 N/m before rupture and 1.4 ± 0.1 N/m after it, a stiffness drop of 75%.

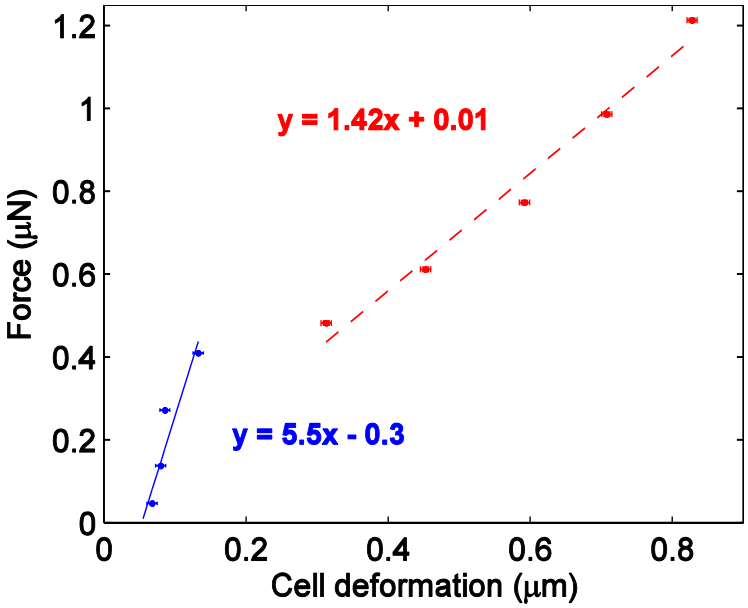

Figure 9.5: Force vs. deformation with linear fits for the pre and post-rupture data (test # 14 in Table 9.3). Back spring elastic constant equals to 0.92 N/m.

In total 9 different baker's yeast cells were tested past rupture and had their stiffness and rupture forces measured as can be seen in Table 9.3. An average cell rupture force of 0.47 ± 0.10 μN was measured. The average stiffness pre and post-rupture were 9.3 ± 3.1 N/m and 0.94 ± 0.57 N/m respectively. The average pre-rupture stiffness was approximately 10x the post-rupture stiffness indicating the severe damage caused at the cell wall. All 9 cells turned blue due to intake of methylene blue after the test indicating that they became non-viable. Figure 9.6 shows the pre and post-rupture stiffness of the 9 baker's yeast cells.

Table 9.3: Rupture force, pre and post-rupture stiffness of baker's yeast cells.

Test (#)	Rupture force (μN)	Stiffness pre-rupture (N/m)	Stiffness post-rupture (N/m)
14	0.45	5.5 ± 1.0	1.42 ± 0.13
15	0.56	13.4 ± 5.2	1.28 ± 0.09
16	0.59	11.6 ± 1.3	0.65 ± 0.12
17	0.46	10.9 ± 1.4	1.12 ± 0.18
18	0.57	12.2 ± 3.0	1.15 ± 0.31
19	0.54	10.8 ± 1.8	1.88 ± 0.34
20	0.31	7.6 ± 0.7	0.38 ± 0.04
21	0.39	4.6 ± 0.3	0.29 ± 0.05
22	0.40	7.5 ± 0.7	0.28 ± 0.02
Avg.	0.47 ± 0.10	9.3 ± 3.1	0.94 ± 0.57

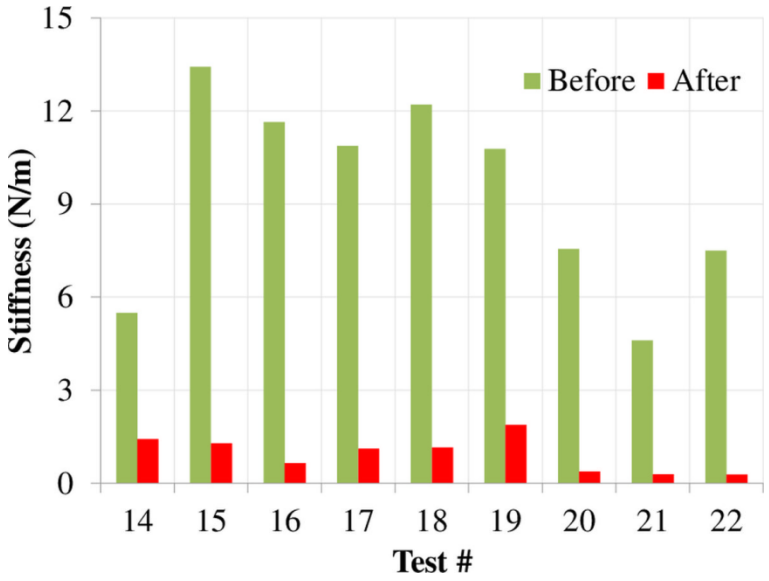

Figure 9.6: Baker's yeast cell stiffness before and after rupture.

The measured pre-rupture stiffness of ruptured cells was higher than the measured stiffness of the cells tested with low forces which experienced maximum forces on the order of 0.27 μN. That could be explained by an initial non-linearity of the cell stiffness as reported by [63] who used a MEMS device to evaluate the force response of single fibroblasts.

9.4 Hysteresis Analysis of Rupture and Non-Ruptured Cells

Baker's yeast cells tested in low force tests (test # 1 to 7) and beyond rupture (test # 14 to 22) were photographed both on compression and on release in order to measure the cells hysteresis. Cells tested below their rupture force showed a residual deformation smaller than 100 nm while ruptured cells showed residual deformations larger than 400 nm. Figure 9.7 (a) shows the force vs. deformation data of a low force test in which the cell showed a residual deformation below 50 nm. Figure 9.7 (b) shows the data of a ruptured cell with a residual deformation higher than 900 nm. The error bars in Figure 9.7 (a) and in Figure 9.7 (b) were calculated as per Figure 9.1 (b) and Figure 9.4 respectively. The area under the curve of these graphs is the energy loss during cell compression. For the cell tests shown in Figure 9.7 (a) and (b) the calculated energy loss was 0.003 pJ and 0.485 pJ respectively. The ~160x increase in energy loss for a ~2-3x increase in maximum force is further evidence that the cell wall was ruptured.

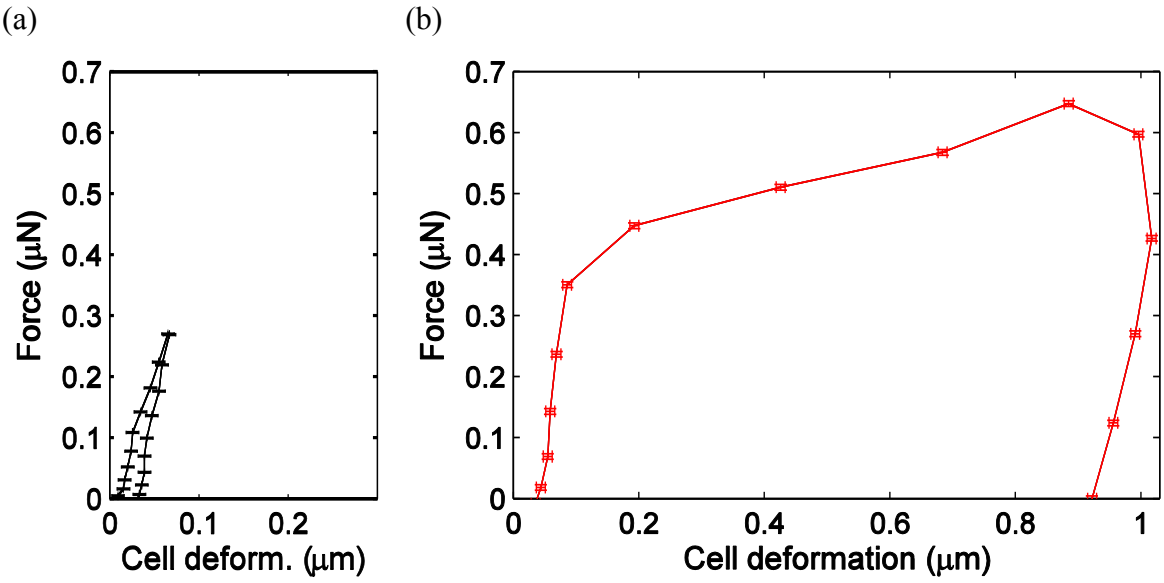

Figure 9.7: (a) Low force test with no cell rupture and residual deformation <50 nm (test # 3 in Table 9.4). (b) Test with cell rupture and residual deformation >900 nm (test # 22 in Table 9.4).

Similar results were observed for all tested cells as can be seen in Table 9.4. Ruptured cells had on average 12x the residual deformation of un-ruptured cells. The average

residual deformation for ruptured and non-ruptured cells was 0.72 ± 0.18 µm and 0.06 ± 0.02 respectively. Ruptured cells had on average ~80x the energy loss of un-ruptured cells, 0.553 ± 0.165 pJ for the ruptured and 0.007 ± 0.002 pJ for the non-ruptured. Figure 9.8 compares the average curves of force vs. deformation of the 5 lowest maximum force tested (no rupture) with the 5 largest maximum force tested. Each point in the graph is an average of 5 different cells tested, with error bars indicating standard deviations. Similar behaviour was shown by [63] that reported plastic deformation of fibroblasts after damaging the cells with a compression force of ~0.4 µN.

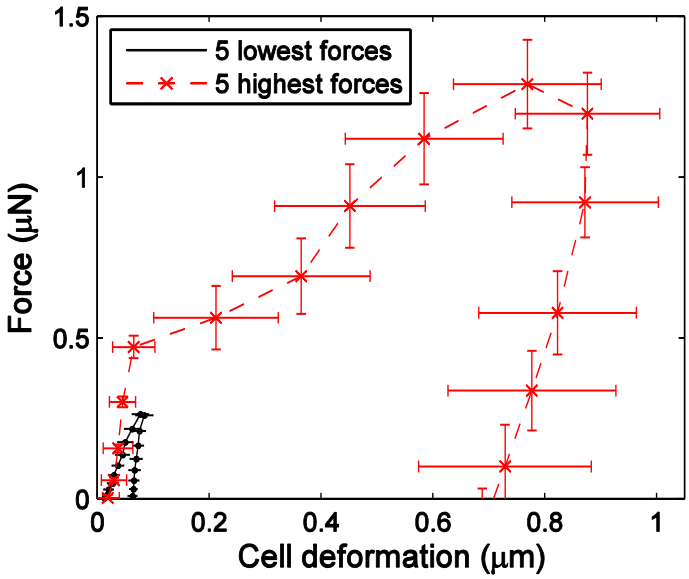

Figure 9.8: Force vs. deformation curves of ruptured (dashed red line) and non-ruptured cell tests (solid black line). Curves are the average of the 5 highest and 5 lowest maximum forces (see Table 9.4).

Table 9.4: Residual deformation and energy loss of ruptured and non-ruptured cells.

Test (#)	**Max. force (µN)**	**Rupture (YES/NO)**	**Residual deform. (µm)**	**Force * Δx Energy loss (pJ)**
1	0.26		0.05	0.009
2	0.27		0.06	0.008
3	0.27		0.03	0.003
4	0.27	NO	0.06	0.007
5	0.27		0.06	0.005
6	0.26		0.08	0.007
7	0.26		0.06	0.008
Avg.	0.27 ± 0.01		0.06 ± 0.02	0.007 ± 0.002
14	1.21		0.73	0.537
15	1.33		0.47	0.525
16	0.85		0.47	0.345
17	1.09		0.96	0.718
18	1.36	YES	0.72	0.849
19	1.44		0.68	0.676
20	0.69		0.70	0.375
21	0.65		0.87	0.465
22	0.65		0.92	0.485
Avg.	1.03 ± 0.32		0.72 ± 0.18	0.553 ± 0.165

9.5 Fatigue

9.5.1 Procedure and Durations of Cell Fatigue Tests

The stiffness of the cells as a function of the number of compressing cycles was investigated. During a squeezing cycle, the initial zero voltage was incremented 10 times by a fixed voltage step and then reduced back to zero in one single step. As the goal was to investigate mechanical fatigue of cells over a large number of cycles, not every cycle was photographed. The voltage was ramped up and then back down for each cycle, thus mechanically cycling the cell each time, but only a sample of the cycles was photographed. A test period of N cycles consisted of N_p photographed cycles, followed by a larger number of non-photographed cycles N_n; therefore, $N = N_p + N_n$. Depending on the type of test, N_p was 1 or 3 and N_n was 5, 20 or 50. To take M measurements, M*N - N_n cycles are required (the last non-photographed cycles are not done).

Three different durations of tests were conducted with individual baker's yeast cells: 20 cells were tested for 37 cycles, 5 cells were tested for 118 cycles, and 3 cells were tested for 268 cycles. The longest cell fatigue tests (268 cycles) took approximately 25 minutes to complete, apart from the cell manipulation time.

9.5.2 Cell Fatigue for Different Maximum Forces

Firstly, cell stiffness was measured over a total of 37 cycles observing the effects of varying the maximum force. Cell stiffness was measured for four different fixed maximum forces: 0.24 μN (6 cells), 0.29 μN (5 cells), 0.31 μN (5 cells) and 0.33 μN (4 cells). Each of these cells were subjected to 37 loading cycles ($M = 7$, $N = 6$, $N_p = 1$, $N_n = 5$, as defined above). Figure 9.9 shows cell stiffness (normalized by the cell stiffness measured on cycle 1) for the four different forces vs. cycle number. Each point in the graph is the average of 4 to 6 cells tested) at the same force and the same cycle number (cycles: 1, 7, 13, 19, 25, 31, and 37). The error bars are the average of the standard deviations of the cell stiffness in each point. Note that for the lowest force 0.24 μN the

average stiffness remained approximately constant after the 37 cycles (increased 6%). At larger forces cell stiffness tended to drop as the number of cycles increased; and the larger the force the greater was the drop. After 37 cycles cell stiffness decreased -17% for 0.29 μN, -32% for 0.31 μN and -44% for 0.33 μN. The lines are linear fits to the measured data of each force. Table 9.5 shows the measured stiffness along the cycles of each cell tested.

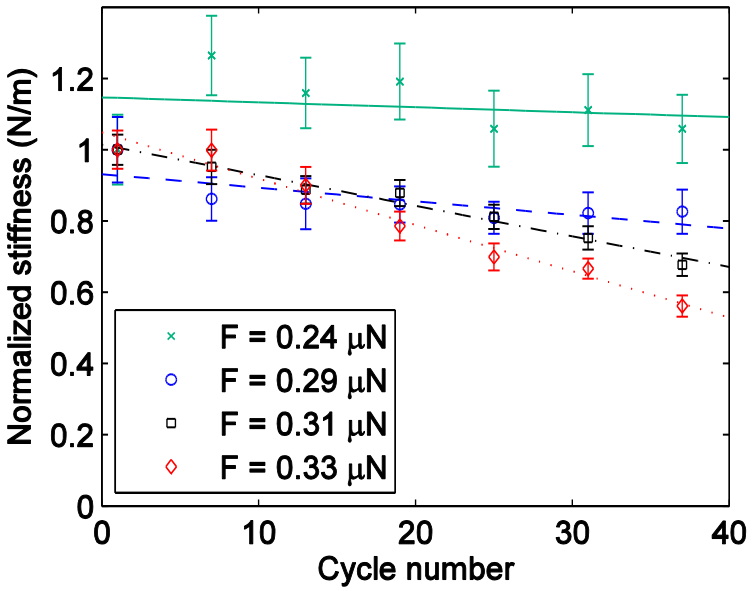

Figure 9.9: Normalized stiffness decay over 37 cycles for 4 different forces. The higher the force the faster is the stiffness decay. Each point is an average of 4 to 6 cells at the same force and cycle number.

Table 9.5: Measured cell stiffness over the cycles for each cell tested up to 37 cycles.

Test (#)	Force (μN)	Cell stiffness from cycles 1 to 37 (N/m)							Ratio 37/1 (%)	Ratio Avg. (%)
		1	7	13	19	25	31	37		
23	0.24	4.2	4.8	4.3	5.5	4.8	4.3	3.3	79	
24		2.3	3.9	3.6	3.1	3.4	3.8	3.5	152	
25		4.3	4.8	5.0	5.5	4.0	4.5	3.7	86	
26		4.6	5.7	4.9	4.4	4.2	4.3	4.2	91	
27		3.3	4.2	3.9	4.1	3.8	3.5	4.2	127	
28		4.0	4.5	3.9	4.0	3.1	3.8	4.1	103	106
29	0.29	5.2	5.7	5.0	4.4	4.7	4.4	4.4	85	
30		9.1	7.3	8.1	7.9	8.2	7.1	7.0	77	
31		10.4	8.4	8.3	8.2	6.8	8.9	8.4	81	
32		6.6	6.0	6.1	6.0	6.3	6.0	6.5	98	
33		7.3	5.0	5.0	6.0	4.7	5.4	5.3	73	83
34	0.31	3.6	3.5	3.3	3.3	2.7	2.1	2.1	58	
35		6.5	5.3	5.0	5.0	4.7	5.0	4.6	71	
36		5.8	5.8	5.1	5.3	5.0	3.8	2.9	50	
37		5.4	5.7	5.1	5.3	4.7	4.9	4.2	78	
38		4.5	4.1	4.2	3.7	3.8	3.8	3.7	82	68
39	0.33	6.4	4.6	5.6	4.3	3.9	4.0	3.5	55	
40		8.6	10.4	8.0	5.6	5.4	5.9	4.2	49	
41		4.1	4.8	4.1	4.1	3.5	2.6	2.4	59	
42		6.0	5.4	4.7	5.0	4.2	4.4	3.7	62	56

The cell pigmentation also changed according to the cycle number and the applied force. In order to quantify this change, the pixel light intensity of each cell was measured: an ellipse of equal area (15.8 ± 0.3 μm^2) was drawn inside each cell and its average pixel intensity was calculated via the image editing software GIMP™. Higher forces led to darker blue cell colouration and consequently lower light pixel intensity after 37 squeezing cycles as can be seen in Figure 9.10 (a). The graph on Figure 9.10 (b) shows the average ratio of the cell pixel intensity at the last and the first cycles for each applied force (0.24, 0.29, 0.31 and 0.33 μN), error bars are the standard deviations. The pixel intensity ratios for forces 0.24, 0.29, 0.31 and 0.33 μN were 99% ± 3%, 98 ± 2%, 95% ± 2% and 93 ± 5% respectively.

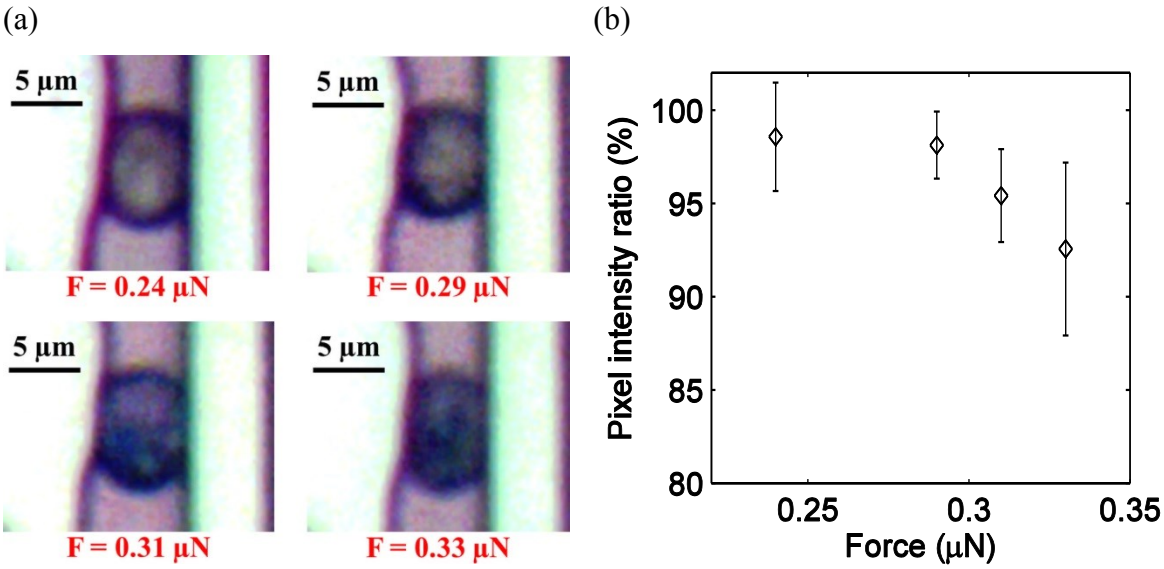

Figure 9.10: (a) Cells photographs at the 37th cycle for different forces. The cell selected was the one with measured pixel intensity closest to the average. (b) Cell average pixel intensity ratio between the 37th and the 1st cycle for different forces.

9.5.3 Cell Fatigue for Higher Cycle Counts

Cell fatigue was also investigated for a higher number of cycles. In total, 5 different cells were compressed up to 118 cycles (M = 6, N = 23, N_p = 3, N_n = 20), and had their stiffness accessed at cycles: 3, 26, 49, 72, 95 and 118. Figure 9.11 shows the force vs. deformation data for one of these cells (only the data from alternate cycles 3, 49, 95 and 118 is shown in the figure for clarity). Each group of points in the graph is an average from 3 consecutive cycles: data from cycle 3 is the average data from cycles 1, 2, and 3; data from cycle 49 is the average data from cycles 47, 48 and 49; and so on. Note the reduction in slope (lower stiffness) as the number of cycles increased, the stiffness on cycles 3, 49, 95, and 118 was 5.7 ± 1.2, 4.1 ± 0.4, 3.4 ± 0.2, and 2.4 ± 0.1 N/m respectively. In this example, the stiffness dropped 57% after 118 cycles.

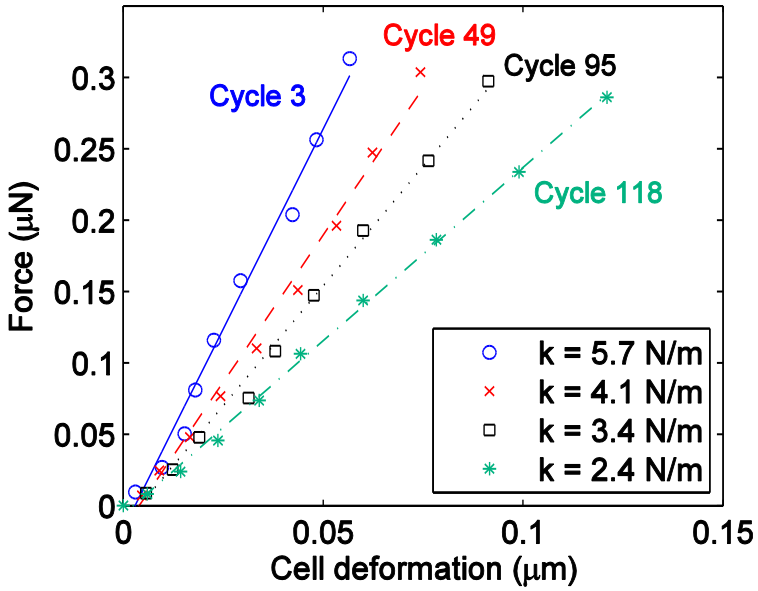

Figure 9.11: Force vs. deformation data of a single cell (test # 44 in Table 9.6) for loading cycles 3, 49, 95 and 118.

Figure 9.12 (a) shows normalized stiffness measurements vs. cycle number for a cell fatigued over 118 cycles. Each point is the average stiffness of 3 consecutive cycles and error bars are standard deviations. In this example, cell stiffness dropped 82% after 118 cycles. Figure 9.12 (b) shows the normalized average stiffness of all 5 cells vs. number of cycles: each point is the average stiffness at the same cycle of the 5 tested cells and the error bars are the standard deviations. After 118 cycles the cells experienced an average stiffness drop of 68%.Table 9.6 shows the measured stiffness along the cycles of each of the 5 cells tested up to 118 cycles.

The maximum force applied to the cells tested up to 118 cycles was in the 0.27-0.30 μN range but was not constant. In addition to the decrease in stiffness, there was a slight reduction on the maximum force as the cycle number increased (see Figure 9.11). The input voltage and the motion of the jaw (d_{jaw}) were identical at each cycle during a test; however, as the cell stiffness (k_{cell}) dropped (with increasing cycles), from equation (11), the back spring motion (d_{spring}) reduced, causing a drop in the maximum applied force ($d_{spring}*k_{spring}$). This force reduction was negligible for the tests with lower cycle counts since the stiffness drop was smaller.

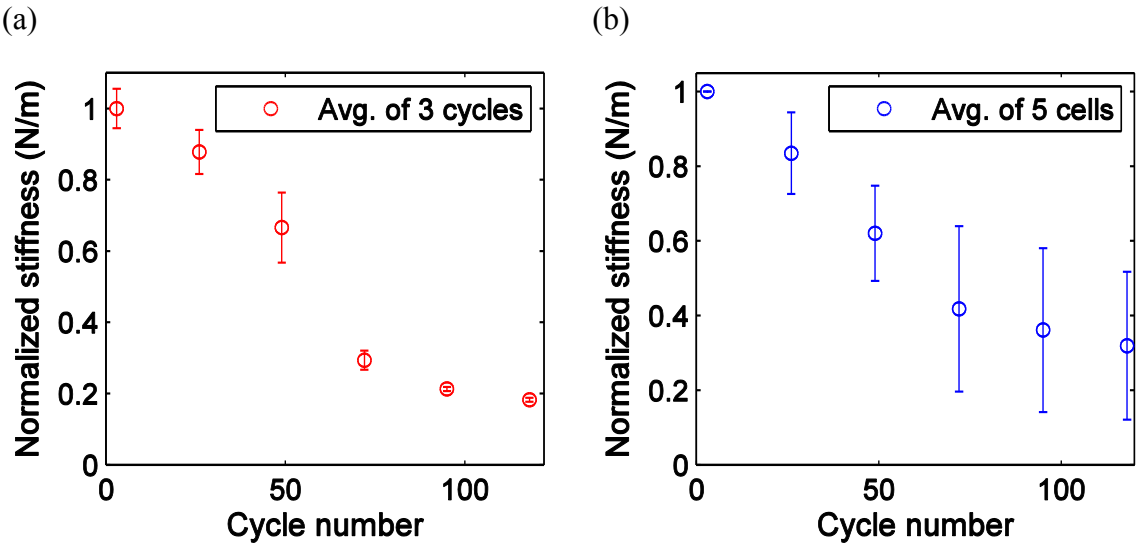

Figure 9.12: (a) Normalized stiffness drop of one cell (test # 47 in Table 9.6) tested up to 118 cycles (b) Average of normalized cell stiffness (total of 5 cells) vs. cycle number up to cycle 118.

Table 9.6: Measured stiffness along the cycles of cells tested up to 118 cycles.

Test (#)	Stiffness (N/m)					
	Cycle 3	Cycle 26	Cycle 49	Cycle 72	Cycle 95	Cycle 118
43	3.92 ± 0.56	3.17 ± 0.16	2.93 ± 0.13	2.51 ± 0.15	2.33 ± 0.2	2.33 ± 0.18
44	5.71 ± 1.18	4.78 ± 0.42	4.11 ± 0.41	3.83 ± 0.37	3.36 ± 0.21	2.43 ± 0.15
45	7.48 ± 0.94	7.30 ± 0.79	3.51 ± 0.79	2.22 ± 0.06	2.24 ± 0.10	2.24 ± 0.10
46	6.99 ± 1.25	4.73 ± 0.66	3.50 ± 0.79	1.32 ± 0.19	0.79 ± 0.02	0.66 ± 0.04
47	4.93 ± 0.27	4.33 ± 0.31	3.28 ± 0.49	1.45 ± 0.13	1.05 ± 0.03	0.90 ± 0.03

3 different cells were tested up to 268 cycles (M = 6, N = 53, N_p = 3, N_n = 50) with a maximum force between 0.28 and 0.29 μN and had their stiffness measured at cycles 3, 56, 109, 162, 215, 268. Figure 9.13 (a) shows the stiffness drop of a single cell as the cycle number increased up to 268. Each point is the average stiffness of 3 consecutive cycles, error bars are standard deviations. By the end of 268 cycles, the cell had a stiffness drop of 73%.Cell stiffness appeared to stop dropping after cycle 215 when it was ~26% of the original stiffness (74% drop). An optimal logistic sigmoid curve was used to fit the experimental data with minimum error; < 0.0001.The obtained curve had a correlation factor of R^2 = 0.9999 and an asymptote (plateau value) of 0.26 N/m.

Figure 9.13 (b) shows the average cell stiffness change of the 3 cells as the number of cycles increased up to 268. Each point is the average stiffness of the 3 cells at the same cycle with error bars showing the standard deviation and the line is a parabolic fit of R^2 = 99%. At the 162th cycle the stiffness variability reduced significantly; after cycle 215 the stiffness seemed to reach a baseline of ~23% of the initial cell stiffness (stiffness drop of 77%). Again, a logistic sigmoid curve was optimized to fit the data (error < 0.001). The final function's correlation factor and asymptote were 0.999 and 0.22 N/m respectively. Table 9.7 shows the measured stiffness along the cycles of the 3 cells tested up to 268 cycles.

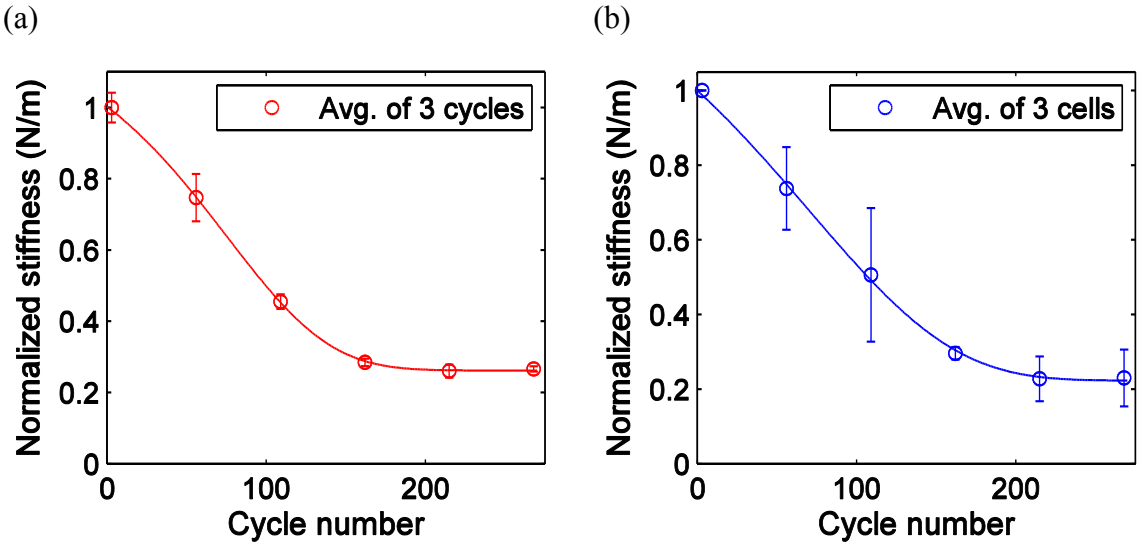

Figure 9.13: (a) Normalized stiffness drop of one cell (test # 49 in Table 9.7) tested up to 268 cycles (b) Average of normalized cell stiffness (total of 3 cells) vs. cycle number up to cycle 268.

Table 9.7: Measured stiffness along the cycles of cells tested up to 268 cycles.

Test (#)	Stiffness (N/m)					
	Cycle 3	Cycle 56	Cycle 109	Cycle 162	Cycle 205	Cycle 268
48	5.79 ± 0.16	3.6 ± 0.21	2.07 ± 0.02	1.66 ± 0.04	1.53 ± 0.08	1.62 ± 0.06
49	6.01 ± 0.25	4.49 ± 0.40	2.74 ± 0.12	1.71 ± 0.06	1.56 ± 0.11	1.60 ± 0.05
50	5.96 ± 0.47	5.03 ± 0.51	4.20 ± 0.17	1.88 ± 0.11	0.94 ± 0.11	0.85 ± 0.02

The pixel light intensity of the cells was measured at cycles 3, 56, 109, 162, 215 and 268 from the first photograph (zero voltage) of each of these cycles. The cell pixel intensity in relation to the substrate reduced over the cycles as the cells turned into blue and darker blue as can be seen in Figure 9.14 (a). The cells started the test averaging 79% of the pixel light intensity of the substrate, but after 268 cycles reduced to 69% Figure 9.14 (b) shows the average pixel light intensity (relative to the substrate) of the 3 cells tested up to 268 cycles (black circles), error bars are standard deviations. To determine if the colour intensity changed simply due to elapsed time, as opposed to fatigue testing, a control cell was used. The control cell in the same graph was squeezed just 3 times but with the same total test time of the other cells, the voltage was discontinued after the third cycle. The control cell showed constant relative pixel intensity in the 78-79% range. Furthermore two other cells were squeezed only at the initials 56 cycles but tested for 268 cycle's time. During the 212 cycles which the cell was not squeezed the drop was of ~1.8%. Therefore, the contribution of elapsed time on cell staining was small to negligible.

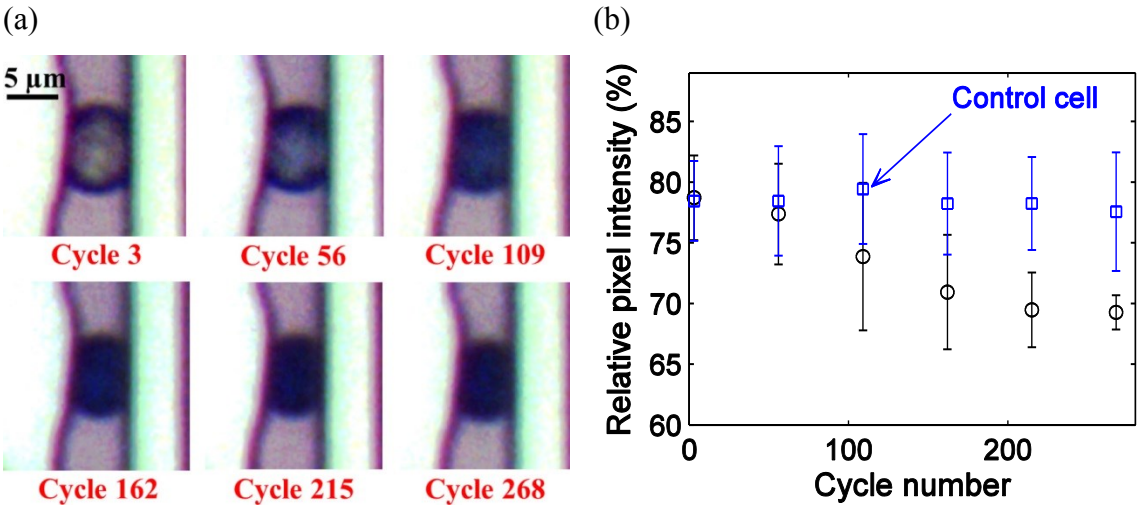

Figure 9.14: (a) Microphotographs of a cell (test # 49 in Table 9.7) at different cycles: it turned darker blue as the number of cycles increased, (b) 3 cells average pixel light intensity relative to the substrate as a function of the cycle number.

Chapter 10: Brewer's Yeast cell measurements

10.1 Determination of Brewing Yeast Cells Rupture Force

Individual brewing yeast cells were also tested: brewing cell preparation was described in section 5.2.2 while cell placement, test and analysis were conducted following the same procedure used for the baker's yeast cells described in section 5. All brewer's yeast cells were squeezed increasing the voltage from 0 to 12 V_{RMS} in a total of 15 steps. This led to the rupture of all the 32 brewing cells (ales and lagers) tested.

The appearance of cracks and cell shrinkage were visual evidence that the cell rupture had been reached. At the end of the test, all cells turned blue indicating they had become non-viable due to cell wall rupture. Figure 10.1 shows a sequence of microphotographs of a brewer's cell (lager) during compression, the applied force ranged from zero to 1.01 μN. From (a) to (c), no significant changes can be seen despite the increase of the squeezing force. In (d), a dark line (a crack) appears on the cell wall indicating a rupture force of 0.45 μN. The last two microphotographs (e) and (f) show the same dark line and a significant cell area reduction compared to the first three microphotographs.

The cell's force vs. deformation (d_{jaw} - d_{spring}) data from this test is shown in Figure 10.2. Each microphotograph in Figure 10.1 corresponds to one of the points in the graph of Figure 10.2. Note that the cell showed a total deformation of 1.29 μm, but only 0.2 μm (16%) occurred before rupture. The measured rupture force of each cell tested at the three different fermentation phases (start, middle, and end) are shown in Table 10.1. The cells fermentation phase is identified by the letters S (start), M (middle), and E (end). The cell species is identified by the letters L (lager) and A (ale). At least 5 cells of each species at each fermentation phase were tested.

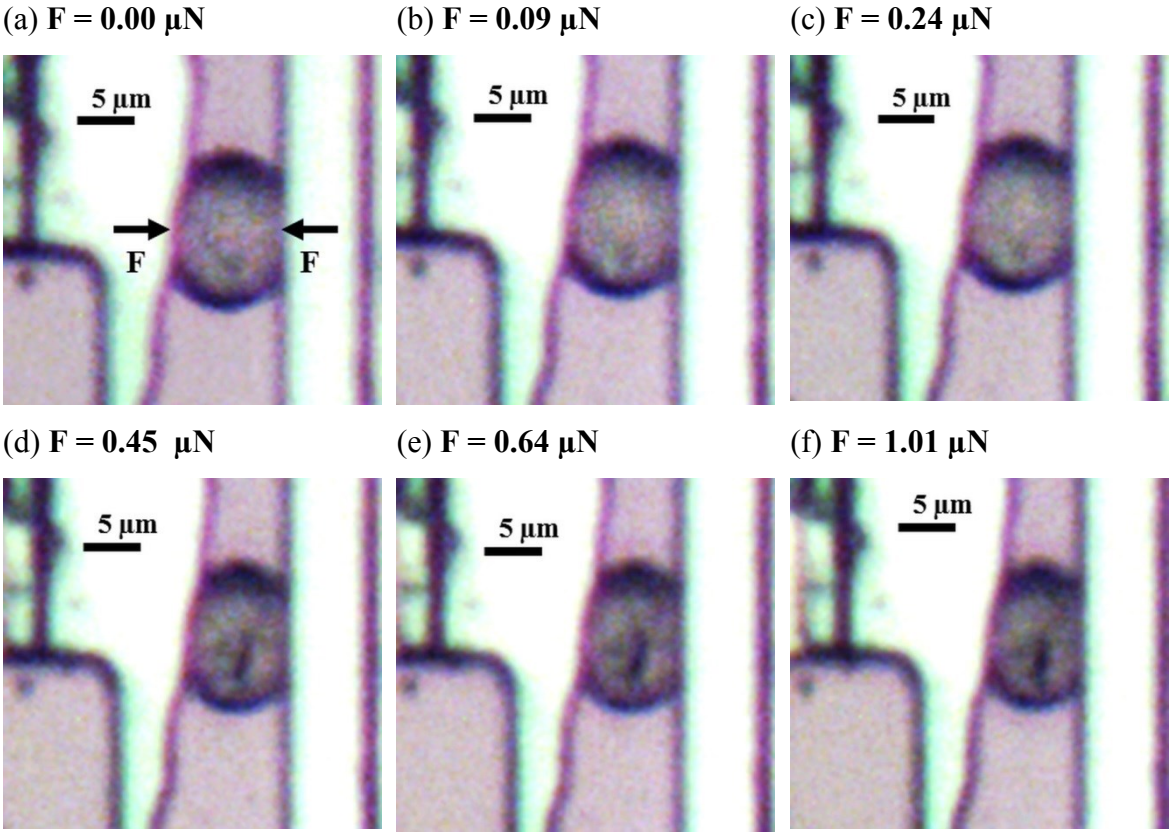

Figure 10.1: Compression of a brewing lager cell (ML4 in Table 10.1). Force increases from zero (a) to 1.01 µN (f). Rupture occurs at (d) when the force is 0.45 µN.

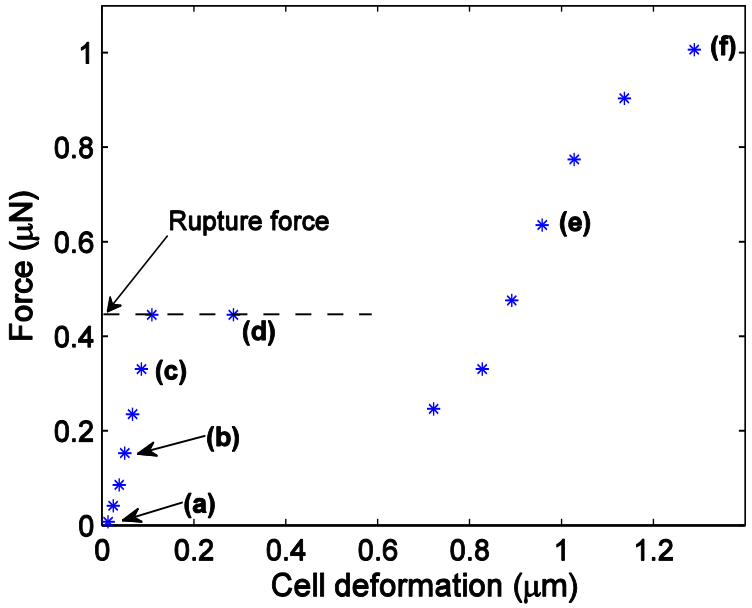

Figure 10.2: Force vs. deformation (d_{jaw} - d_{spring}) data of the tested lager yeast cell (ML4 in Table 10.1). Letters (a) to (f) correspond to the microphotographs in Figure 10.1.

Table 10.1: Rupture force of all brewing cells tested; lagers and ales at start, middle, and end of the fermentation.

Cell species	Start		Middle		End	
		Rupture force (μN)		Rupture force (μN)		Rupture force (μN)
LAGER	SL1	0.45	ML1	0.56	EL1	0.57
	SL2	0.55	ML2	0.41	EL2	0.23
	SL3	0.57	ML3	0.34	EL3	0.58
	SL4	0.47	ML4	0.45	EL4	0.44
	SL5	0.59	ML5	0.45	EL5	0.41
	Avg.	0.53 ± 0.06	Avg.	0.44 ± 0.08	Avg.	0.45 ± 0.14
ALE	SA1	0.22	MA1	0.26	EA1	0.32
	SA2	0.23	MA2	0.23	EA2	0.34
	SA3	0.27	MA3	0.26	EA3	0.35
	SA4	0.24	MA4	0.25	EA4	0.29
	SA5	0.33	MA5	0.24	EA5	0.19
	-		-		EA6	0.33
	-		-		EA7	0.34
	Avg.	0.26 ± 0.05	Avg.	0.25 ± 0.01	Avg.	0.31 ± 0.05

For both species tested, no significant difference in the rupture force was observed at the three fermentation phases. The average rupture force for lager cells was 0.53 ± 0.06 μN, 0.44 ± 0.08 μN and 0.45 ± 0.14 μN for start, middle, and end of fermentation respectively. The average rupture force for ale cells was smaller: 0.26 ± 0.05 μN, 0.25 ± 0.01 μN, and 0.31 ± 0.05 μN for start, middle, and end of fermentation respectively. Figure 10.3 shows the average rupture force values at each fermentation phase: each point in the graph is an average of at least 5 tested cells and error bars are the standard deviations of the averages.

Averaging all the cells of the same species, the measured rupture force of the lager cells was ~1.7x that of the ale cells: 0.47 ± 0.10 μN for lager and 0.28 ± 0.05 μN for ale. This may be linked to the typically higher environmental stress resistance of lager cells (at least with respect to temperature). Note that these results were found for two specific strains of ale and lager; however, whether they are representative of the species as a whole remains to be found. It should be noted that the rupture force given in this

experiment was assessed by compressing the cell between two plates. Other studies such as [96] have reported that yeast can withstand high hydrostatic pressure far in excess of the rupture force measured at this study.

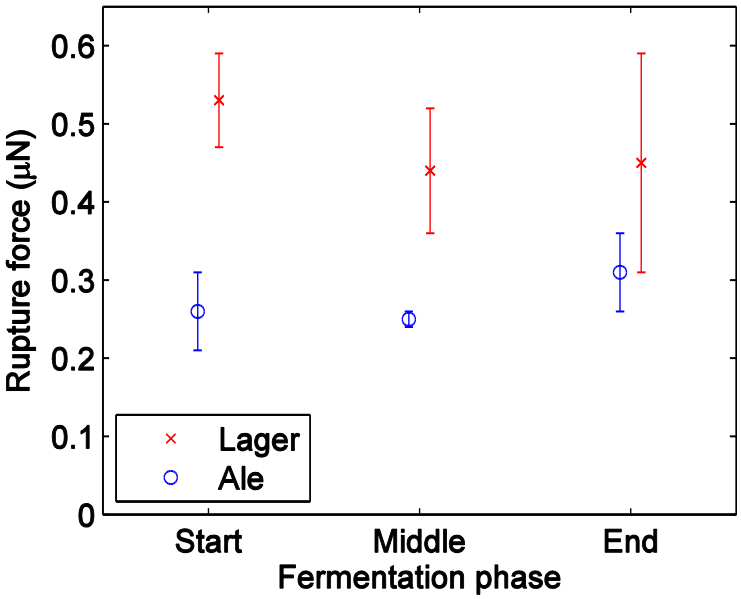

Figure 10.3: Cell rupture forces for ale and lager cells from different fermentation phases. Average of at least 5 tested cells for each point, error bars show standard deviation.

All cells tested were ellipsoids that had their in-plane dimensions estimated by fitting an ellipse to their contour (error of ~0.2 μm). The cells major diameters ranged from 7.2 to 10.4 μm (average of 8.4 ± 1.0 μm) while their minor diameter ranged from 5.5 to 7.8 μm (average of 6.6 ± 0.7 μm). For both species, cells at the start of fermentation showed slightly smaller dimensions than the cells in the middle and in the end of fermentation (approximately 90% of the average diameter). Lager cells tested were slightly larger than ale cells: the major diameter of lager cells was on average 7.7 ± 0.9 μm compared to 7.3 ± 0.6 for the ale cells. Inside each of the 6 groups of cells, no significant correlation between the cell geometry (diameters, area or aspect ratio) and rupture force or stiffness was observed.

10.2 Pre and Post-Rupture Stiffness of Brewing Yeast Cells

This section compares the pre and post-rupture stiffness of ale and lager cells in the middle phase of the fermentation. The pre and post-rupture stiffness were calculated by plotting the force vs. deformation data of each cell and then taking the slopes of the linear fits. All cells showed a linear force response before and after rupture with a discontinuity on the order of 0.5 µm. After cell rupture, the force reduced considerably before it started increasing again. This is due to the cell shrinkage due to rupture which causes the back spring to deflect back, reducing the force on the cell. Figure 10.4 shows the force vs. deformation data of a lager cell of pre-rupture stiffness of 5.3 ± 0.3 N/m and post-rupture stiffness of 0.82 ± 0.02 N/m (slopes of the linear fits). Figure 10.5 shows an ale cell of pre-rupture stiffness of 4.6 ± 0.2 N/m and a post-rupture stiffness of 0.99 ± 0.06 N/m. Note the higher force required to rupture the lager species. The pre and post-rupture stiffness of each mid-fermentation cell tested can be seen in Table 10.2.

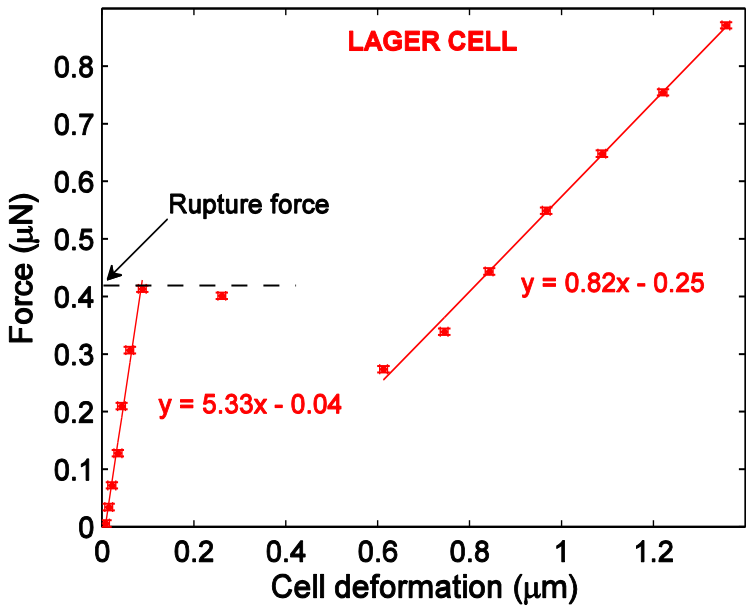

Figure 10.4: Force vs deformation for a lager cell (ML2 in Table 10.2). The two linear fits are separated by a discontinuity of about 0.53 µm. The error bars were calculated as per Figure 9.4.

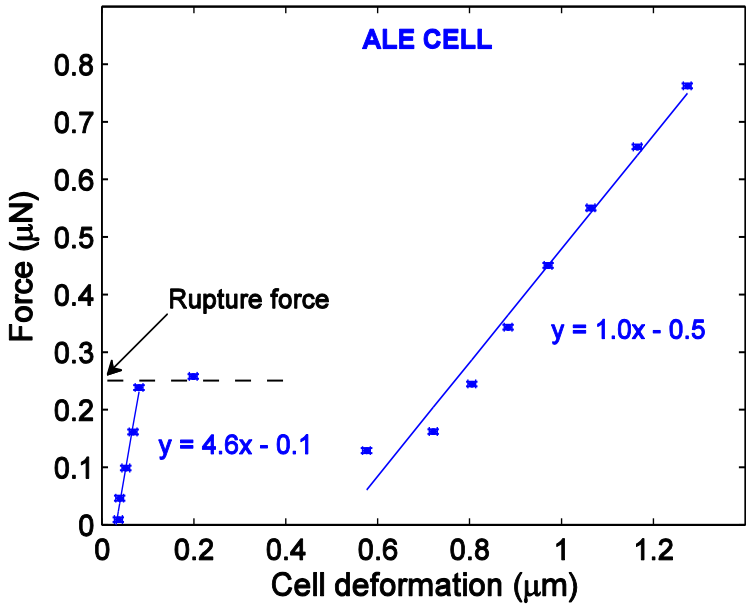

Figure 10.5: Force vs. deformation for an ale cell (MA4, in Table 10.2). The two linear fits are separated by a discontinuity of approximately 0.50 μm. The error bars were calculated as per Figure 9.4.

Table 10.2: Pre and post-rupture stiffness of lager and ale cells in the middle of fermentation.

Cell species	#	**Pre-rupture stiffness (N/m)**	**Post-rupture stiffness (N/m)**
LAGER	ML1	4.8 ± 0.2	0.90 ± 0.02
	ML2	5.3 ± 0.3	0.82 ± 0.02
	ML3	4.6 ± 0.1	1.07 ± 0.11
	ML4	4.7 ± 0.1	1.47 ± 0.14
	ML5	6.8 ± 0.4	1.38 ± 0.05
	Avg.	5.3 ± 0.9	1.13 ± 0.29
ALE	MA1	5.4 ± 0.4	1.08 ± 0.09
	MA2	3.2 ± 0.2	1.06 ± 0.09
	MA3	5.7 ± 0.8	0.70 ± 0.04
	MA4	4.6 ± 0.2	0.99 ± 0.06
	MA5	5.0 ± 0.3	1.03 ± 0.09
	Avg.	4.8 ± 1.0	0.97 ± 0.16

In total, five mid-fermentation ale and five mid-fermentation lager cells had their pre and post-rupture stiffness measured. The average lager pre and post-rupture stiffness was 5.3 ± 0.9 N/m and 1.13 ± 0.29 N/m respectively. For the ale population, the average pre and post-rupture stiffness was 4.8 ± 1.0 N/m and 0.97 ± 0.16 N/m respectively. For both species, the pre-rupture stiffness is ~5x the post-rupture stiffness. Ale and lager cells showed similar pre and post-rupture stiffness. This indicates that throughout most brewing processes in which stiffness is a potential limiting factor (such as centrifugation, pumping, etc.), ale and lager cells will behave similarly. Figure 10.6 shows the average pre and post-rupture stiffness of the brewing cells in the middle of the fermentation, error bars are the averages standard deviations.

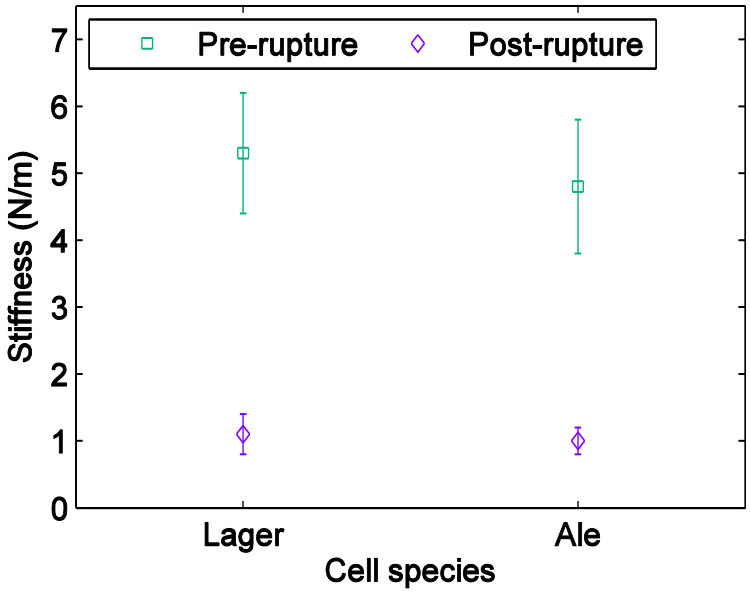

Figure 10.6: Pre and post-rupture stiffness of ale and lager mid-fermentation brewing yeast cells. Each point is the average 5 tested cells, error bars are the standard deviations.

10.3 Stiffness and Fermentation Phase

Figure 10.7 shows the pre-rupture stiffness of ale and lager cells over 3 different fermentation phases: start, middle and end. Each point in the graph is the average of five tested cells with error bars indicating standard deviations. The average ale pre-rupture stiffness increased over the fermentation phases: 3.8 ± 1.2 N/m (start), 4.8 ± 1.0 N/m

(middle), and 7.5 ± 1.9 N/m (end). The average lager pre-rupture stiffness decreased over time: 11.5 ± 3.3 N/m (start), 5.3 ± 0.9 N/m (middle), and 5.6 ± 1.5 N/m (end). The considerable higher stiffness of lager cells at the start phase was unexpected. This may be due to residual cold storage adaptions present in some pitched yeast after 24 [97]. Further work will assess the impact of long term cold storage and improper hydration processes on yeast characteristics. Alternatively, this may be a consequence of the limited sample size (5 cells sample). A larger sample size (>5 cells/phase) would represent better the entire population; however, the sample was limited to five cells/phase to ensure the cells were tested within a 2-3 hour window, keeping them in the same fermentation phase.

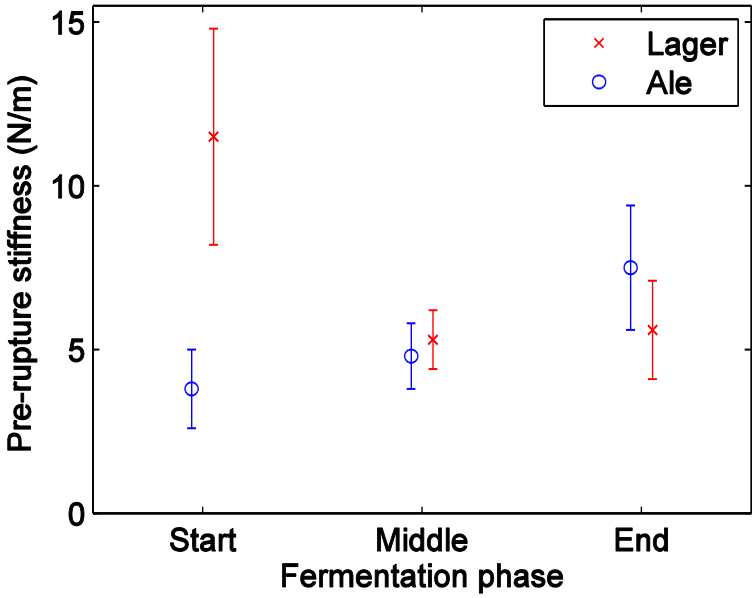

Figure 10.7: Pre-rupture stiffness for ale and lager cells at three different fermentation phases: start, middle and end.

The post-rupture stiffness of ale and lager cells was also measured at the 3 different phases of fermentation. Both species showed similar post-rupture stiffness measurements at each phase and for both species the cell post-rupture stiffness in the two last phases was ~3x that of the first fermentation phase. The average ale post-rupture stiffness was 0.30 ± 0.01, 0.97 ± 0.16, and 0.88 ± 0.23 N/m for start, middle and end of fermentation respectively. The average lager post-rupture stiffness was 0.36 ± 0.08, 1.13 ± 0.29, and 0.98 ± 0.16 N/m for start, middle and end of fermentation respectively. The lower post-

rupture stiffness of cells in the start of fermentation may be because they had not undergone conditioning; and therefore, have slightly different characteristics, such as a thinner cell wall, compared to cells in the middle and end of fermentation [23].

Overall, it should be noted that a slurry with a high concentration of ruptured yeast cells is likely to exhibit different mechanical properties than a slurry full of non-ruptured yeast cells. Figure 10.8 shows the ratio (%) of post and pre-rupture stiffness of the cells through the fermentation phases. The cells post-rupture stiffness is always lower than 30% of the pre-rupture stiffness.

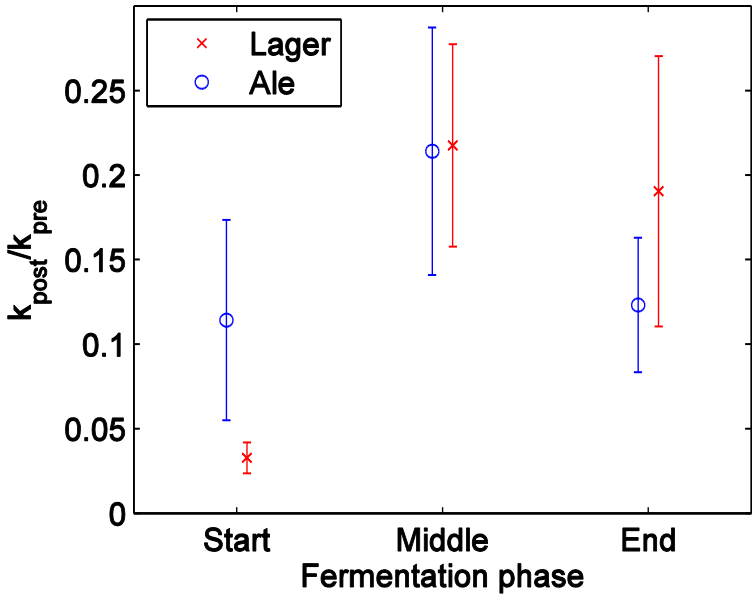

Figure 10.8: Ratio of post and pre-stiffness of lager an ale cells through the fermentation phases.

Chapter 11: Conclusion and Future Work

11.1 MEMS Cell Testing Device

This thesis described the design and test of an electrothermal MEMS device able to measure mechanical properties of single living microbial cells in aqueous media. The planar polysilicon structure amplified the electrothermal chevron motion (diminished by the high thermal conductivity of the water) reaching relatively high displacements (2.3-2.5 μm) with average motion repeatability below 10 nanometers. Individual cells were pushed against a compliant accordion spring able to measure their mechanical response. The squeezer's final displacement was large enough to compress single baker's and brewer's yeast cells causing rupture by purely mechanical means. The device successfully measured cell stiffness, rupture force, hysteresis, and fatigue of more than 80 individual yeast cells.

11.2 Simulations

Finite Element Analysis was used to simulate a number of physical quantities. In addition to the estimated temperature rise of the thermal actuator, the displacements of chevron and jaw were also simulated. Experimental measurements showed good agreement with the displacements predictions (~10% difference), and FEA calculations of the back spring stiffness matched the analytical calculations (less than 3% difference). Furthermore, a yeast cell mechanical model estimated the relation between cell stiffness and Young's model, and the influence of cell shape, size and contact area on its stiffness.

11.3 Baker's Yeast Measurements

Baker's yeast (*Saccharomyces Cerevisiae*) cells showed linear force response before and after rupture which was characterized by the appearance of cracks on the cell wall and a considerable drop of cell stiffness (~10x). Ruptured cells showed much stronger hysteretic behaviour than non-ruptured cells resulting in evident plastic deformation.

An average baker's yeast cell rupture force of 0.47 ± 0.10 μN was measured. Previous microplate compression studies reported an yeast cell (*Saccharomyces Cerevisiae*) rupture force between 50 and 250 μN [76]-[80] while a penetration force in the range of 0.09-0.23 μN was measured using AFM for a wild-type yeast [83]. In this study, the contact area was higher than the AFM but lower than the microplate; and therefore, the rupture forces measured were between AFM and microplate reported values.

In the case of fatigue or cyclic loading (tests performed below the rupture limit), cell stiffness decreased with the number of cycles. However, after ~200 cycles the stiffness seemed to plateau at ~20% of the initial stiffness value. Moreover, cell viability seemed to be related to stiffness decay. All cells that experienced a reduction in stiffness showed a visible increase in blue pigmentation. This could indicate that the cell becomes less stiff as it is becomes non-viable.

11.4 Brewer's Yeast Measurements

The study also measured the cell stiffness and rupture force of two brewing yeast species, ale (*Saccharomyces cerevisiae*) and lager (*Saccharomyces pastorianus*), at three different fermentation phases. As occurred with the baker's yeast cells, the brewer's cells showed linear force response and cell rupture was characterized by the visualization of cracks on the cell wall followed by a significant drop of cell stiffness.

It was found that the cell rupture force of the lager strain was ~2x the rupture force of the ale strain. Brewers typically set their equipment specifically to avoid compromising yeast viability. Therefore, brewers who have optimized their processes for lagers may have difficulties incorporating some ale strains due to lower mechanical resistance.

No significant difference on the rupture force was observed due to fermentation phase (start, middle or end). It is possible that the miniature fermentation assay utilized did not result in sufficient environmental stress for the yeast to undergo observable adaption, or that adaption did occur without resulting in changes to the rupture force of these strains.

11.5 Future Work

1) Different working media could be tested in order to observe how the cell mechanical properties change due to the environment. Additionally, the tests could be conducted in solutions more similar to the real cell media.

2) The bulk of the testing work in this thesis was on Bakers' yeast. In the brewing sector, the mechanical characteristics of extreme strains of brewer's yeast could be assessed; for example, high gravity fermentation yeast [98] used to produce beer with high alcoholic percentage could be analyzed.

3) One of the limitations the current device is low throughput, each cell must be manipulated and tested one by one. A micro fluidic system (or a robotic apparatus) able to control the motion of the cells around the chip could be integrated with the squeezer in the future.

References

[1] D. Kim, P. K. Wong, J. Park, A. Levchenko and Y. Sun. Microengineered platforms for cell mechanobiology. *Annu. Rev. Biomed. Eng. 11*pp. 203-233. 2009. . DOI: 10.1146/annurev-bioeng-061008-124915.

[2] M. Nagayama, H. Haga and K. Kawabata. Drastic change of local stiffness distribution correlating to cell migration in living fibroblasts. *Cell Motil. Cytoskeleton 50(4),* pp. 173-179. 2001. . DOI: 10.1002/cm.10008.

[3] K. Tsukada, E. Sekizuka, C. Oshio and H. Minamitani. Direct measurement of erythrocyte deformability in diabetes mellitus with a transparent microchannel capillary model and high-speed video camera system. *Microvasc. Res. 61(3),* pp. 231-239. 2001. . DOI: 10.1006/mvre.2001.2307.

[4] S. Suresh. Biomechanics and biophysics of cancer cells. *Acta Biomaterialia 3(4),* pp. 413-438. 2007.

[5] S. Suresh, J. Spatz, J. P. Mills, A. Micoulet, M. Dao, C. T. Lim, M. Beil and T. Seufferlein. Connections between single- cell biomechanics and human disease states: Gastrointestinal cancer and malaria. *Acta Biomaterialia 1(1),* pp. 15. 2005.

[6] G. Y. H. Lee and C. T. Lim. Biomechanics approaches to studying human diseases. *Trends Biotechnol. 25(3),* pp. 111-118. 2007. . DOI: 10.1016/j.tibtech.2007.01.005.

[7] X. Cai, X. Xing, J. Cai, Q. Chen, S. Wu and F. Huang. Connection between biomechanics and cytoskeleton structure of lymphocyte and jurkat cells: An AFM study. *Micron 41(3),* pp. 257-262. 2010. . DOI: http://dx.doi.org/10.1016/j.micron.2009.08.011.

[8] S. E. Cross, Y. S. Jin, J. Rao and J. K. Gimzewski. Nanomechanical analysis of cells from cancer patients. *Nature Nanotechnology 2(12),* pp. 780-3. 2007.

[9] N. Bontoux, L. Dauphinot, M. Potier and o. C. Royal Society. *Unravelling Single Cell Genomics : Micro and Nanotools* 2010.

[10] J. Pi, H. Cai, H. Jin *et al*. Qualitative and quantitative analysis of ROS- mediated oridonin- induced oesophageal cancer KYSE- 150 cell apoptosis by atomic force microscopy. *PloS One 10(10),* pp. e0140935. 2015. . DOI: 10.1371/journal.pone.0140935.

[11] G. K. Ananthasuresh. *Micro and Smart Systems : Technology and Modeling* 2012.

[12] W. M. Van Spengen, R. Puers and I. De Wolf. On the physics of stiction and its impact on the reliability of microstructures. *J. Adhes. Sci. Technol. 17(4),* pp. 563-582. 2003. . DOI: 10.1163/15685610360554410.

[13] C. Liu, V. B. Mungurwadi and A. V. Nandi. *Foundations of MEMS* 2012.

[14] J. N. James, V. Mukundan, D. Bernstein and L. P. Beth. Microsystems for biomechanical measurements. *Pediatr. Res. 63(5),* pp. 576-583. 2008. . DOI: 10.1203/PDR.0b013e31816b2ec4.

[15] C. G. Galbraith and M. P. Sheetz. A micromachined device provides a new bend on fibroblast traction forces. *Proc. Natl. Acad. Sci. U. S. A. 94(17),* pp. 9114-9118. 1997.

[16] S. Youn, W. L. Dong and Young-Ho Cho. Cell- deformability- monitoring chips based on strain- dependent cell-lysis rates. *Microelectromechanical Systems, Journal Of 17(2),* pp. 302-308. 2008. . DOI: 10.1109/JMEMS.2007.912724.

[17] Y. H. Anis, M. R. Holl and D. R. Meldrum. Automated selection and placement of single cells using vision- based feedback control. *Automation Science and Engineering, IEEE Transactions On 7(3),* pp. 598-606. 2010. . DOI: 10.1109/TASE.2009.2035709.

[18] M. T. Madigan. *Brock Biology of Microorganisms* (Fourteenth edition, Global edition.. ed.) 2015.

[19] G. M. Walker. *Yeast Physiology and Biotechnology* 1998.

[20] M. El-Mansi and C. F. A. Bryce. *Fermentation Microbiology and Biotechnology* (2nd ed.. ed.) 2007.

[21] Canadean, "Beer, Cider and Flavored Alcoholic Beverages Market," 2011.

[22] V. Vidgren, J. Multanen, L. Ruohonen and J. Londesborough. The temperature dependence of maltose transport in ale and lager strains of brewer's yeast. *FEMS Yeast Research 10(4),* pp. 402-411. 2010. . DOI: 10.1111/j.1567-1364.2010.00627.x.

[23] B. R. Gibson, S. J. Lawrence, J. P. R. Leclaire, C. D. Powell and K. A. Smart. Yeast responses to stresses associated with industrial brewery handling. *FEMS Microbiol. Rev. 31(5),* pp. 535-569. 2007. . DOI: 10.1111/j.1574-6976.2007.00076.x.

[24] T. Gualtieri, E. Ragni, L. Mizzi, U. Fascio and L. Popolo. The cell wall sensor Wsc1p is involved in reorganization of actin cytoskeleton in response to hypo-osmotic shock in saccharomyces cerevisiae. *Yeast 21(13),* pp. 1107-1120. 2004. . DOI: 10.1002/yea.1155.

[25] X. Li and J. Wang, "Strengthening of Cell Wall Structure Enhances Stress Resistance and Fermentation Performance in Lager Yeast," *J. Am. Soc. Brew. Chem.,* vol. 72, pp. 88-94, 2014.

[26] Z. Zhou, Z. Wang and L. Lin. *Microsystems and Nanotechnology* 2012.

[27] G. Gerlach. *Introduction to Microsystem Technology : A Guide for Students* 2008.

[28] M. J. Madou. *Fundamentals of Microfabrication the Science of Miniaturization* 2002*Second Edition*.

[29] J. Carter, A. Cowen, B. Hardy, R. Mahadevan, M. Stonefield and S. Wilcenski. *PolyMUMPs Design Handbook: A Mumps (R) Process* 2005.

[30] D. Sameoto, T. Hubbard and M. Kujath. Operation of electrothermal and electrostatic MUMPs microactuators underwater. *J Micromech Microengineering 14(10),* pp. 1359-1366. 2004.

[31] N. Scuor, P. Gallina, H. Panchawagh, R. Mahajan, O. Sbaizero and V. Sergo. Design of a novel MEMS platform for the biaxial stimulation of living cells. *Biomed. Microdevices 8(3),* pp. 239-246. 2006. . DOI: 10.1007/s10544-006-8268-3.

[32] F. Antoniolli, S. Maggiolino, N. Scuor, P. Gallina and O. Sbaizero. A novel MEMS device for the multidirectional mechanical stimulation of single cells: Preliminary results. *Mechanism and Machine Theory 78*pp. 131-140. 2014. . DOI: 10.1016/j.mechmachtheory.2014.03.009.

[33] S. Warnat, C. Forbrigger and T. Hubbard, "Thermal MEMS actuator operation in aqueous media/seawater: Performance enhancement through atomic layer deposition post processing of PolyMUMPs devices," *Journal of Vacuum Science & Technology A,* vol. 33, pp. A126-1-A126-8, 2015.

[34] L. Que, J. Park and Y. B. Gianchandani. Bent-beam electrothermal actuators--part I: Single beam and cascaded devices. *J Microelectromech Syst 10(2),* pp. 247-254. 2001.

[35] M. Chiao and L. Lin. Self- buckling of micromachined beams under resistive heating. *Microelectromechanical Systems, Journal Of 9(1),* pp. 146-151. 2000. . DOI: 10.1109/84.825789.

[36] R. Hickey, M. Kujath and T. Hubbard. Heat transfer analysis and optimization of two-beam microelectromechanical thermal actuators. *J.Vac.Sci.Technol.A Journal of Vacuum Science & Technology A: Vacuum, Surfaces, and Films 20(3),* pp. 971-974. 2002.

[37] Y. Lai, J. McDonald, M. Kujath and T. Hubbard. Force, deflection and power measurements of toggled microthermal actuators. *J Micromech Microengineering 14(1),* pp. 49-56. 2004.

[38] R. Hickey, D. Sameoto, T. Hubbard and M. Kujath. Time and frequency response of two-arm micromachined thermal actuators. *J Micromech Microengineering 13(1),* pp. 40-46. 2003.

[39] C. Moraes, C. A. Simmons and Y. Sun, "Cell Mechanics Meets MEMS," *CSME Bulletin SCGM CSME, University of Toronto,* pp. 15-18, 2006.

[40] M. J. Rosenbluth, W. A. Lam and D. A. Fletcher. Force microscopy of nonadherent cells: A comparison of leukemia cell deformability. *Biophys. J. 90(8),* pp. 2994-3003. 2006.

[41] Q. S. Li, G. Y. H. Lee, C. N. Ong and C. T. Lim. AFM indentation study of breast cancer cells. *Biochem. Biophys. Res. Commun. 374(4),* pp. 609-613. 2008. . DOI: http://dx.doi.org/10.1016/j.bbrc.2008.07.078.

[42] T. D. Pollard and G. G. Borisy. Cellular motility driven by assembly and disassembly of actin filaments. *Cell 112(4),* pp. 453-465. 2003. . DOI: http://dx.doi.org/10.1016/S0092-8674(03)00120-X.

[43] B. A. Brown. *Hematology : Principles and Procedures* 1993.

[44] C. Pallister and M. Watson. *Haematology* 2011.

[45] A. Z. Szeri. Fluid film lubrication (2nd edition). Available: http://app.knovel.com/hotlink/toc/id:kpFFLE000F/fluid-film-lubrication.

[46] A. Touhami, B. Nysten and Y. F. Dufrene. Nanoscale mapping of the elasticity of microbial cells by atomic force microscopy. *Langmuir 19*pp. 4539-4543. 2003.

[47] M. Li, L. Liu, N. Xi, Y. Wang, Z. Dong, X. Xiao and W. Zhang. Atomic force microscopy imaging and mechanical properties measurement of red blood cells and aggressive cancer cells. *Science China.Life Sciences 55(11),* pp. 968-73. 2012.

[48] Schmid-Schönbein GW, Sung KL, Tözeren H, Skalak R,Chien S,. Passive mechanical properties of human leukocytes. *Biophys. J. 36(1),* pp. 243-56. 1981.

[49] O. Loh, A. Vaziri and H. Espinosa. The potential of MEMS for advancing experiments and modeling in cell mechanics. *Exp. Mech. 49(1),* pp. 105-124. 2009. . DOI: 10.1007/s11340-007-9099-8.

[50] K. Addae-Mensah and J. P. Wikswo. Measurement techniques for cellular biomechanics in vitro. *Exp. Biol. Med. (Maywood) 233(7),* pp. 792. 2008. . DOI: 10.3181/0710-MR-278.

[51] I. Ahmad and M. Ahmad. Trends in characterizing single cell's stiffness properties. *Micro and Nano Syst Lett 2(1),* pp. 1-11. 2014. . DOI: 10.1186/s40486-014-0008-5.

[52] R. M. Hochmuth. Micropipette aspiration of living cells. *J. Biomech. 33(1),* pp. 15-22. 2000. . DOI: 10.1016/S0021-9290(99)00175-X.

[53] Mashmoushy, H., Zhang, Z.,Thomas, C.R.,. Micromanipulation measurement of the mechanical properties of baker's yeast cells. *Biotechnol. Tech. 12(12),* pp. 925. 1998.

[54] J. Guck, R. Ananthakrishnan, H. Mahmood, T. J. Moon, C. C. Cunningham and J. Käs. The optical stretcher: A novel laser tool to micromanipulate cells. *Biophys. J. 81(2),* pp. 767-784. 2001. . DOI: http://dx.doi.org/10.1016/S0006-3495(01)75740-2.

[55] Y. Tan, D. Sun, J. Wang and W. Huang. Mechanical characterization of human red blood cells under different osmotic conditions by robotic manipulation with optical tweezers. *Biomedical Engineering, IEEE Transactions On 57(7),* pp. 1816-1825. 2010. . DOI: 10.1109/TBME.2010.2042448.

[56] D. Desmaële, M. Boukallel and S. Régnier. Actuation means for the mechanical stimulation of living cells via microelectromechanical systems: A critical review. *J. Biomech. 44(8),* pp. 1433-1446. 2011. . DOI: 10.1016/j.jbiomech.2011.02.085.

[57] J. Rajagopalan and M. T. Saif. Mems sensors and microsystems for cell mechanobiology. *MEMS Sensors and Microsystems for Cell Mechanobiology 21(5),* pp. 054002. 2011. . DOI: 10.1088/0960-1317/21/5/054002.

[58] X. R. Zheng and X. Zhang. Microsystems for cellular force measurement: A review. *Microsystems for Cellular Force Measurement 21(5),* pp. 054003. 2011. . DOI: 10.1088/0960-1317/21/5/054003.

[59] D. Serrell, T. Oreskovic, A. Slifka, R. Mahajan and D. Finch. A uniaxial bioMEMS device for quantitative force- displacement measurements. *Biomed. Microdevices 9(2),* pp. 267-275. 2007. . DOI: 10.1007/s10544-006-9032-4.

[60] V. Mukundan and B. L. Pruitt. MEMS electrostatic actuation in conducting biological media. *J Microelectromech Syst Journal of Microelectromechanical Systems 18(2),* pp. 405-13. 2009.

[61] V. Mukundan, W. Nelson and B. Pruitt. Microactuator device for integrated measurement of epithelium mechanics. *Biomed. Microdevices 15(1),* pp. 117-123. 2013. . DOI: 10.1007/s10544-012-9693-0.

[62] T. S. Yang Shengyuan. Reversible and repeatable linear local cell force response under large stretches. *Exp. Cell Res. 305(1),* pp. 42-50. 2005. . DOI: 10.1016/j.yexcr.2004.12.026.

[63] S. Yang and M. T. Saif. Force response and actin remodeling (agglomeration) in fibroblasts due to lateral indentation. *Acta Biomaterialia 3(1),* pp. 77-87. 2007. . DOI: 10.1016/j.actbio.2006.07.005.

[64] Y. Shengyuan and S. Taher. Micromachined force sensors for the study of cell mechanics. *Rev. Sci. Instrum. 76(4),* pp. 044301-13. 2005. . DOI: 10.1063/1.1863792.

[65] Y. Sun, K. -. Wan, K. P. Roberts, J. C. Bischof and B. J. Nelson. Mechanical property characterization of mouse zona pellucida. *NanoBioscience, IEEE Transactions On 2(4),* pp. 279-286. 2003. . DOI: 10.1109/TNB.2003.820273.

[66] S. Petronis, J. Gold and B. Kasemo. Microfabricated force- sensitive elastic substrates for investigation of mechanical cellsubstrate interactions. *Microfabricated Force-Sensitive Elastic Substrates for Investigation of Mechanical Cell-Substrate Interactions 13(6),* pp. 900-913. 2003. . DOI: 10.1088/0960-1317/13/6/313.

[67] J. Tan, J. Tien, D. Pirone and D. Gray. Cells lying on a bed of microneedles: An approach to isolate mechanical force. *Proc. Natl. Acad. Sci. U. S. A. 100(4),* pp. 1484. 2003.

[68] Y. Zhao, C. C. Lim, D. B. Sawyer, R. Liao and X. Zhang. Cellular force measurements using single- spaced polymeric microstructures: Isolating cells from base substrate. *Cellular Force Measurements using Single-Spaced Polymeric Microstructures 15(9),* pp. 1649-1656. 2005. . DOI: 10.1088/0960-1317/15/9/006.

[69] Y. Zhao and X. Zhang. Cellular mechanics study in cardiac myocytes using PDMS pillars array. *Sensors & Actuators: A.Physical 125(2),* pp. 398-404. 2006. . DOI: 10.1016/j.sna.2005.08.032.

[70] T. Herricks, M. Antia and P. K. Rathod. Deformability limits of plasmodium falciparum - infected red blood cells. *Cell. Microbiol. 11(9),* pp. 1340-1353. 2009. . DOI: 10.1111/j.1462-5822.2009.01334.x.

[71] H. Bow, I. V. Pivkin, M. Diez-silva, S. J. Goldfless, M. Dao, J. C. Niles, S. Suresh and J. Han. A microfabricated deformability-based flow cytometer with application to malaria. *Lab on a Chip; Lab Chip 11(6),* pp. 1065-1073. 2011. . DOI: 10.1039/c0lc00472c.

[72] J. S. Dudani, D. R. Gossett, H. T. K. Tse and D. Di Carlo. Pinched- flow hydrodynamic stretching of single-cells. *Lab on a Chip; Lab Chip 13(18),* pp. 3728-3734. 2013. . DOI: 10.1039/c3lc50649e.

[73] I. Doh, W. C. Lee, Y. -. Cho, A. P. Pisano and F. A. Kuypers. Deformation measurement of individual cells in large populations using a single- cell microchamber array chip. *Appl. Phys. Lett. 100(17),* 2012. . DOI: 10.1063/1.4704923.

[74] W. Zhang, M. Gnerlich, J. J. Paly, Y. Sun, G. Jing, A. Voloshin and S. Tatic-Lucic. Apolymer v-shaped electrothermal actuator array for biological applications. *A*

Polymer V-Shaped Electrothermal Actuator Array for Biological Applications 18(7), pp. 075020. 2008. . DOI: 10.1088/0960-1317/18/7/075020.

[75] K. Kim, X. Liu, Y. Zhang and Y. Sun. Nanonewton force-controlled manipulation of biological cells using a monolithic mems microgripper with two-axis force feedback. *Nanonewton Force-Controlled Manipulation of Biological Cells 18(5),* pp. 055013. 2008. . DOI: 10.1088/0960-1317/18/5/055013.

[76] J. Arfsten, C. Bradtmöller, I. Kampen and A. Kwade, "Compressive testing of single yeast cells in liquid environment using a nanoindentation system," *J. Mater. Res.,* vol. 23, pp. 3153-3160, 2008.

[77] A. Overbeck, I. Kampen and A. Kwade. Mechanical characterization of yeast cells: Effects of growth conditions. *Lett. Appl. Microbiol. 61(4),* pp. 333-338. 2015. . DOI: 10.1111/lam.12468.

[78] J. D. Stenson. "Investigating the Mechanical Properties of Yeast Cells," PhD, 2009.

[79] Stenson, John D., Hartley, Peter, Wang, Changxiang, Thomas,Colin R.,. Determining the mechanical properties of yeast cell walls. *BTPR Biotechnology Progress 27(2),* pp. 505-512. 2011.

[80] E. Smith, Z. Zhang, C. R. K. Thomas, E. Moxham and A. P. J. Middelberg. The mechanical properties of saccharomyces cerevisiae. Presented at Proc. Natl. Acad. Sci. U.S.A. 2000, .

[81] J. Arfsten, S. Leupold, C. Bradtmöller, I. Kampen and A. Kwade. Atomic force microscopy studies on the nanomechanical properties of saccharomyces cerevisiae. *Colloids and Surfaces B: Biointerfaces 79(1),* pp. 284-290. 2010. . DOI: 10.1016/j.colsurfb.2010.04.011.

[82] A. Pelling, S. Sehati, E. Gralla, J. Valentine and J. Gimzewski. Local nanomechanical motion of the cell wall of saccharomyces cerevisiae. *Science 305(5687),* pp. 1147-50. 2004.

[83] M. R. Ahmad, M. Nakajima, S. Kojima, M. Homma and T. Fukuda. The effects of cell sizes, environmental conditions, and growth phases on the strength of individual W303 yeast cells inside ESEM. *NanoBioscience, IEEE Transactions On 7(3),* pp. 185-193. 2008. . DOI: 10.1109/TNB.2008.2002281.

[84] S. Warnat, H. King, C. Forbrigger and T. Hubbard. Polymumps mems device to measure mechanical stiffness of single cells in aqueous media. *PolyMUMPs MEMS Device to Measure Mechanical Stiffness of Single Cells in Aqueous Media 25(2),* pp. 025011. 2015. . DOI: 10.1088/0960-1317/25/2/025011.

[85] B. Barazani, S. Warnat and T. Hubbard. Simulation and optical measurement of MEMS thermal actuator sub- micron displacements in air and water. Presented at The 28Th Canadian Conference on Electrical and Computer Engineering (CCECE 2015, IEEE). 2015, . DOI: 10.1109/CCECE.2015.7129090.

[86] D. C. Miller, B. L. Boyce, M. T. Dugger, T. E. Buchheit and K. Gall. Characteristics of a commercially available silicon-on-insulator MEMS material. *Sensors & Actuators: A.Physical 138(1),* pp. 130-144. 2007. . DOI: 10.1016/j.sna.2007.04.023.

[87] R. C. Juvinall. "Appendix D-3," in *Fundamentals of Machine Component Design* (5th ed.), K. M. Marshek, Ed. 2012, .

[88] American Society of Brewing Chemists. *Methods of Analysis, Yeast-14 Miniature Fermentation Assay; Yeast-3A Methylene Blue Dead Yeast Cell Stain*, American Society of Brewing Chemists, Ed. 2011, .

[89] A. J. MacIntosh, A. Maclead, A. Beattie, A. Eck, M. Edney, B. Rossnagel and R. A. Speers, "Assessing the effect of fungal infection of barley and malt on premature yeast flocculation," *J. Am. Soc. Brew. Chem.,* vol. 72(1), pp. 66-72, 2013.

[90] C. Yamahata, E. Sarajlic and G. Krijnen J.M. Subnanometer translation of microelectromechanical systems measured by discrete fourier analysis of CCD images. *J Microelectromech Syst Journal of Microelectromechanical Systems 19(5),* pp. 1273-5. 2010.

[91] S. Warnat, H. King, R. Schwartz, M. Kujath and T. Hubbard. Submicron displacement measurements of MEMS using optical microphotographs in aqueous media: Enhancement using color image processing. Presented at Materials Research Society Symposium Proceedings. 2014, . DOI: 10.1557/opl.201.58.

[92] A. A. Geisberger, N. Sarkar, M. Ellis and G. D. Skidmore. Electrothermal properties and modeling of polysilicon microthermal actuators. *Microelectromechanical Systems, Journal Of 12(4),* pp. 513-523. 2003. . DOI: 10.1109/JMEMS.2003.815835.

[93] R. W. Johnstone and M. Parameswaran. Modelling surface- micromachined electrothermal actuators. *Electrical and Computer Engineering, Canadian Journal Of 29(3),* pp. 193-202. 2004. . DOI: 10.1109/CJECE.2004.1532523.

[94] A. K. Bryan, A. Goranov, A. Amon and S. R. Manalis. Measurement of mass, density, and volume during the cell cycle of yeast. *Proc. Natl. Acad. Sci. U. S. A. 107(3),* pp. 999-1004. 2010. . DOI: 10.1073/pnas.0901851107.

[95] T. Svaldo Lanero, O. Cavalleri, S. Krol, R. Rolandi and A. Gliozzi. Mechanical properties of single living cells encapsulated in polyelectrolyte matrixes. *J. Biotechnol. 124(4),* pp. 723-731. 2006. . DOI: 10.1016/j.jbiotec.2006.02.016.

[96] P. M. B. Fernandes. How does yeast respond to pressure? *Braz. J. Med. Biol. Res. 38(8),* pp. 1239-1245. 2005.

[97] C. D. Powell, D. E. Quain and K. A. Smart. The impact of brewing yeast cell age on fermentation performance, attenuation and flocculation. *FEMS Yeast Research 3(2),* pp. 149-157. 2003. . DOI: 10.1016/S1567-1356(03)00002-3.

[98] X. Tao, D. Zheng, T. Liu, P. Wang, W. Zhao, M. Zhu, X. Jiang, Y. Zhao and X. Wu. A novel strategy to construct yeast saccharomyces cerevisiae strains for very high gravity fermentation (A novel strategy to construct yeast strains). *PLoS ONE 7(2),* pp. e31235. 2012. . DOI: 10.1371/journal.pone.0031235.

Appendix A: Copyright Permission Letters

Part of the text and figures of this thesis were previously published/accepted to publication in two different journal papers, in conference proceedings as a full paper, and in other conference proceedings as an abstract (poster presentation). See below the complete citation of these publications and the corresponding copyright letters.

B. Barazani, S. Warnat and T. Hubbard. Simulation and optical measurement of MEMS thermal actuator sub- micron displacements in air and water. Presented at The 28Th Canadian Conference on Electrical and Computer Engineering (CCECE 2015, IEEE). 2015, . DOI: 10.1109/CCECE.2015.7129090.

B. Barazani, S. Warnat, A. Fine and T. Hubbard. MEMS squeezer for the measurement of single cell rupture force, stiffness change, and hysteresis. J Micromech Microengineering 27(2), pp. 025002. 2017. . DOI: 10.1088/1361-6439/27/2/025002.

B. Barazani, A. J. MacIntosh, S. Warnat and T. Hubbard, "Mechanical characterization of individual brewing yeast cells using MEMS: Cell rupture force and stiffness," in World Brewing Congress 2016 Proceedings, Denver, Colorado, U.S.A., 2016.

B. Barazani, A. J. MacIntosh, S. Warnat and T. Hubbard, "Mechanical characterization of individual brewing yeast cells using MEMS: cell rupture force and stiffness," Journal of the American Society of Brewing Chemists, vol. 3, 2017, in press.

IEEE permission grant

http://ieeexplore.ieee.org/document/7129090/

The IEEE does not require individuals working on a thesis to obtain a formal reuse license, however, you may print out this statement to be used as a permission grant:

Requirements to be followed when using any portion (e.g., figure, graph, table, or textual material) of an IEEE copyrighted paper in a thesis:

1) In the case of textual material (e.g., using short quotes or referring to the work within these papers) users must give full credit to the original source (author, paper, publication) followed by the IEEE copyright line © 2011 IEEE.
2) In the case of illustrations or tabular material, we require that the copyright line © [Year of original publication] IEEE appear prominently with each reprinted figure and/or table.
3) If a substantial portion of the original paper is to be used, and if you are not the senior author, also obtain the senior author's approval.

Requirements to be followed when using an entire IEEE copyrighted paper in a thesis:

1) The following IEEE copyright/ credit notice should be placed prominently in the references: © [year of original publication] IEEE. Reprinted, with permission, from [author names, paper title, IEEE publication title, and month/year of publication]
2) Only the accepted version of an IEEE copyrighted paper can be used when posting the paper or your thesis on-line.
3) In placing the thesis on the author's university website, please display the following message in a prominent place on the website: In reference to IEEE copyrighted material which is used with permission in this thesis, the IEEE does not endorse any of [university/educational entity's name goes here]'s products or services. Internal or personal use of this material is permitted. If interested in reprinting/republishing IEEE copyrighted material for advertising or promotional purposes or for creating new collective works for resale or redistribution, please go to http://www.ieee.org/publications_standards/publications/rights/rights_link.html to learn how to obtain a License from RightsLink.

If applicable, University Microfilms and/or ProQuest Library, or the Archives of Canada may supply single copies of the dissertation.

BACK ••• CLOSE WINDOW

Copyright © 2016 Copyright Clearance Center, Inc. All Rights Reserved. Privacy statement. Terms and Conditions.
Comments? We would like to hear from you. E-mail us at customercare@copyright.com

Assignment of copyright and publication agreement

IOP Publishing Limited ("IOP") agrees to publish:

Manuscript Title: MEMS squeezer for the measurement of single cell rupture force, stiffness change, and hysteresis (the "Article") written by

Names of all authors: Barazani, Bruno; Warnat, Stephan; Fine, Alan; Hubbard, Ted ("the Named Authors") in the following journal Journal of Micromechanics and Microengineering ("the Journal")

Name of copyright owner(s) (if not the Named Author(s) – see Important Information above):

("the Institution")

IOP Ref: JMM-102219

Part 1 - Subscription Copyright Assignment

Assignment of copyright

1.1 In consideration for acceptance and publication of the Article, the Named Authors of the Article and/or the Institution hereby assign, where necessary by present assignment of future copyright, to IOP with full title guarantee the entire copyright in all original material published as part of the Article (which expression includes but is not limited to the text, abstract, tables, figures and graphs, related corrigenda or "comments" and multimedia content but excludes any other item referred to as supplementary material) throughout the world for the full term of copyright (including any extensions or renewals thereof) for all media and formats, whether known or unknown. Such assignment shall be effective only if the Article (or any resubmission of the Article) is accepted for publication. For the avoidance of doubt, copyright does not subsist in any fundamental data underlying the Article and nothing in this agreement is intended to limit access to or use of such data.

1.2 If the Article, or any part of it, is protected by Crown Copyright, in consideration for acceptance and publication of the Article, the relevant Named Authors and the relevant originating department or agency hereby grant IOP a royalty-free worldwide freely-transferrable licence for the full term of copyright (including any extensions or renewals thereof) for all media and formats, whether known or unknown, to do in relation to the Article all acts restricted by copyright worldwide including, but not limited to, the right of action under section 101A of the Copyright Designs and Patents Act 1988. Such licence shall be effective only if the Article is accepted for publication and shall be exclusive to IOP for a period of twelve calendar months following the date of online publication of the Article. Thereafter, the licence shall be non-exclusive.

1.3 In consideration for acceptance and publication of the Article, the Named Authors and/or the Institution hereby grant IOP a royalty-free non-exclusive worldwide freely transferrable licence for the full term of copyright (including any extensions or renewals thereof) to do in relation to any supplementary material not deemed to be part of the Article and/or any video abstract all acts restricted by copyright worldwide. This shall include, but not be limited to, making the material available under any licence that IOP deems appropriate for purposes including, but not limited to, the maximisation of visibility and the long term preservation of the content.

1.4 Each of the Named Authors consents to the publication and processing by IOP of their email addresses.

Representations and warranties

2.1 The Institution and/or the Submitting Author on behalf of the Named Authors (as appropriate) represent and warrant that:

2.1.1 the Article is the original work of the Named Authors;

2.1.2 the Article has not been published previously in any form, other than as part of the Named Authors' research theses or dissertations (which fact has been notified to IOP in writing) or as a preprint, for example on the arXiv.org service;

2.1.3 each of the Named Authors has made a material contribution to the conception and/or writing of the Article, has received the final version of the Article, has agreed to its submission on the terms contained herein and takes responsibility for it and submission has been approved as necessary by the authorities at the establishment where the research was carried out;

2.1.4 the Submitting Author completes and returns this agreement as authorised agent for and on behalf of all the Named Authors and has the full power to enter into this agreement and to make the grants and assignments it contains;

2.1.5 the Article has not been and shall not be submitted to another publisher prior to withdrawal or rejection by IOP;

2.1.6 the Article does not infringe any third party rights, it contains nothing libellous or unlawful, all factual statements are to the best of the Named Authors' knowledge true or based on valid research conducted according to accepted norms and all required permissions have been obtained in writing;

2.1.7 the Article expressly acknowledges any third party funding and/or potential conflicts of interest; and

2.1.8 any supplementary material or video abstract is the original work of the Named Authors, or is the property of the Institution, or permission has been obtained from its owner(s) for its publication by IOP and permission has been obtained for the inclusion of any third party content (including music).
2.2 The Named Authors and/or the Institution (as appropriate) indemnify and will keep indemnified IOP against all costs and expenses suffered or incurred by IOP as a result of and/or arising out of any breach of the representations and/or warranties in this section 2.

The Named Authors' rights

3.1 IOP grants the Named Authors the rights specified in paragraphs 3.2 and 3.3. All such rights must be exercised solely for non-commercial purposes. Where possible, any use should display citation information and IOP's copyright notice, and, for electronic use, best efforts must be made to include a link to the online abstract in the Journal.

Exercise of the rights in paragraph 3.2 may use the version of the Article published in the Journal ("Final Published Version").

Exercise of the rights referred to in paragraph 3.3 must not use the Final Published Version and extend only to the Named Authors' own format (which may include amendments made following peer review but not any editing, typesetting or other changes made by IOP) (the "Accepted Manuscript") and must be accompanied by the following statement of provenance:

'This is an author-created, un-copyedited version of an article accepted for publication in Journal of Micromechanics and Microengineering.
IOP Publishing Ltd is not responsible for any errors or omissions in this version of the manuscript or any version derived from it. The Version of Record is available online at [insert DOI].'

3.2 The rights are:

3.2.1 To make copies of the Article (all or part) for teaching purposes;

3.2.2 To include the Article (all or part) in a research thesis or dissertation;

3.2.3 To make oral presentation of the Article (all or part) and to include a summary and/or highlights of it in papers distributed at such presentations or in conference proceedings; and

3.2.4 To use figures and text from the Article falling within the quota outlined in the STM Permissions Guidelines (http://www.stm-assoc.org/permissions-guidelines/) at the relevant time in force.
For the avoidance of doubt, the Named Authors retain all proprietary rights in the Article other than copyright.

3.3 Additional rights of the Named Authors are to:

3.3.1 Use the Accepted Manuscript (all or part) without modification in personal compilations of the Named Authors' own works (provided not created by a third party publisher); and

3.3.2 Include the Accepted Manuscript (all or part) on the Named Authors' own personal website(s), institutional website(s) and third party websites in accordance with the Author Rights set out at the following url legal.ioppublishing.org/author-rights on the date of submission of this agreement.
Miscellaneous

4. To the extent that there are moral rights in the Article, all the Named Authors expressly reserve and assert their moral rights to be identified as the authors of the Article.

5. The Named Authors and/or the Institution shall execute such further documents, and take such actions and do such things, as may be requested by IOP at IOP's reasonable expense to give full effect to the terms of this agreement.

6. For the avoidance of doubt, the grants and assignment envisaged herein shall become effective only upon acceptance of the Article for publication. In the event that the Article is withdrawn prior to acceptance, or is rejected, this agreement shall have no effect and no party shall be bound by it.

7. This agreement shall be governed by English Law and subject to the non-exclusive jurisdiction of the English courts.

Confirmation

8. By typing the Submitting Author's name into the box at Part 3 below and clicking "Submit", the Named Authors agree to these terms. Authorised signatories of any third party copyright owner(s) agree, on behalf of such owner(s), to these terms by typing the owner's name into the "Institution" box at the top of the page.

Part 2 - Open Access Copyright Assignment
Assignment of copyright

1.1 In consideration for acceptance and publication of the Article, the Named Authors of the Article and/or the Institution hereby assign, where necessary by present assignment of future copyright, to IOP with full title guarantee the entire copyright in all original material published as part of the Article (which expression includes but is not limited to the text, abstract, tables, figures and graphs, related corrigenda or "comments" and multimedia content but excludes any other item referred to as supplementary material) throughout the world for the full term of copyright (including any extensions or renewals thereof) for all media and formats, whether known or unknown. Such assignment shall be

Sue Figueroa <sfigueroa@scisoc.org>
Yesterday, 9:42 PM

Dear Bruno Barazani,
As one of the authors of the identified paper, you may reproduce any portions needed in your thesis as long as the paper is properly cited. In this case, since it is not in print and page numbers are not yet established, it can be cited as "In Press".
Please let me know if you have any questions.
Sincerely,
Sue Figueroa
==========
Sue Figueroa, Permissions Coordinator
American Association of Brewing Chemists
3340 Pilot Knob Road
St. Paul, MN 55121
+1.651.994.3871 (telephone)
+1.651.454.0766 (fax)
sfigueroa@scisoc.org

Bruno Barazani
Yesterday, 3:28 PM

Dear Mis Duling,

As I explained to Dr. Bamforth last week, I am seeking for permission to include substantial portion of the following paper in my thesis:

"Mechanical characterization of individual brewing yeast cells using MEMS: cell rupture force and stiffness" Barazani B. *et al.*
which will appear in *Journal of the American Society of Brewing Chemists* no. 3 of 2017.

Unfortunately, I am very close to my Thesis submission deadline, so I would ask you to please provide me an answer as soon as you can.

Thank you very much

Bruno Barazani
PhD candidate
Dalhousie University
Mech Eng Dept